7-20-2018 10:00 AM

The Development Of Platforms For Inhibiting RHAMM-HA Interactions & The Development Of An Optical Probe For Measuring Glomerular Filtration Rate

Alexandra Hauser-Kawaguchi
The University of Western Ontario

Supervisor
Luyt, Leonard G.
The University of Western Ontario

Graduate Program in Chemistry
A thesis submitted in partial fulfillment of the requirements for the degree in Doctor of Philosophy

Recommended Citation

Hauser-Kawaguchi, Alexandra, "The Development Of Platforms For Inhibiting RHAMM-HA Interactions & The Development Of An Optical Probe For Measuring Glomerular Filtration Rate" (2018). *Electronic Thesis and Dissertation Repository*. 5576.
https://ir.lib.uwo.ca/etd/5576

Abstract

Carbohydrates are a class of molecule occurring widely in the body. Their presence has varied biological implications, generating clinical interest regarding their impact on disease prognosis. This thesis will investigate the development of chemical entities surrounding two carbohydrates, hyaluronan and inulin.

The Receptor for hyaluronan mediated motility (RHAMM) is one of several receptors for hyaluronan (HA), a polysaccharide that, when fragmented, has pro-angiogenic and inflammatory properties. RHAMM expression is tightly regulated during homeostasis but increases in response to cellular stress, including during injury or disease states. HA-RHAMM interactions stimulate the Ras-ERK-Mek pathway to promote cell motility, differentiation, and proliferation. Specific inhibition of HA-RHAMM interactions could have significant therapeutic potential.

Chapters 2 and 3 explore two platforms for disrupting HA-RHAMM interactions. Chapter 2 discusses development of a 62-amino acid chemically synthesized truncated RHAMM protein, 7 kDa RHAMM, for use in screening novel therapeutics. This mini-protein exhibited similar secondary structure, bioactivity, and HA-binding capabilities as the full-length protein, and binds known RHAMM-binding peptides with similar affinities as recombinant RHAMM. This suggests that it is a suitable replacement for the difficult-to-obtain recombinant version. Chapter 3 discusses the development of double stapled RHAMM peptide mimetics as therapeutic anti-inflammatory agents. The peptides were evaluated for secondary structure, HA-binding capability, and inflammation-related bioactivity. The lead compound blocked 27.2% and 52% of induced inflammation in culture and *in vivo*, respectively. The lead peptide was further optimized to improve metabolic stability while maintaining secondary structure and HA-binding affinity, improving therapeutic efficacy.

Glomerular filtration rate (GFR) is a measure of kidney function and a prognostic indicator of chronic kidney disease. Filtration of the polysaccharide inulin is the gold standard for measuring GFR clinically, as it is neither reabsorbed nor secreted by the kidneys; however, this method is laborious and invasive. Chapter 4 explores the development of a near-infrared dye-labeled inulin, Cy7.5-inulin conjugate, as an optical probe to accurately and non-invasively measure GFR by transcutaneous pulse dye densitometer. The conjugate was characterized by different analytical techniques, and is stable under *in vivo* conditions. The probe was successfully used in a pig model to accurately measure GFR non-invasively.

Keywords

Receptor for hyaluronan mediated motility, RHAMM, HMMR, Hyaluronan, Inflammation, Peptide, Glomerular filtration rate, Inulin, Optical probe

Co-Authorship Statement

Chapter 1, section 1.1, 1.4, and 1.6 were adapted from published mini-review A. Hauser-Kawaguchi, L. G. Luyt, E. Turley, *Matrix Biol*, 2018, S0945-053X(17), 30444-4. Dr. Eva Turley and Dr. Len Luyt significantly contributed to the mini-review.

Chapter 2 is a manuscript that has been submitted for publication in Bioorganic & Medicinal Chemistry. 7 kDa RHAMM and all other peptides within this chapter were synthesized, purified and characterized by Alexandra Hauser-Kawaguchi. Characterization by CD spectroscopy was carried out by Alexandra Hauser-Kawaguchi. All SPR kinetic analyses and sensor chip preparation were carried out by Alexandra Hauser-Kawaguchi. The migration study was carried out by Dr. Cornelia Tolg and Dr. Teresa Peart using resources and instruments provided by Dr. Eva Turley. Confocal microscopy work with 7 kDa RHAMM was carried out by Dr. Cornelia Tolg using resources and instruments provided by Dr. Eva Turley. Fluorescent staining and microscopy (**Figure S2.10**) were carried out by Catalina Vasquez, a former M.Sc. student of Dr. John Lewis.

Chapter 3 is a manuscript in preparation. All peptides within this chapter were synthesized, purified and characterized by Alexandra Hauser-Kawaguchi. Characterization by CD spectroscopy was carried out by Alexandra Hauser-Kawaguchi and Claire Browne. All SPR kinetic analyses and sensor chip preparation were carried out by Alexandra Hauser-Kawaguchi. The inflammatory protein array and RANTES ELISA were conducted by Dr. Teresa Peart using resources provided by Dr. Eva Turley and Novare Pharmaceuticals Inc. The LPS mouse study was carried out by Dr. Cornelia Tolg and Jenny Ma using resources provided by Dr. Eva Turley and Novare Pharmaceuticals Inc.

Chapter 4 is a manuscript that has been submitted to International Journal of Biological Macromolecules. Carboxymethyl inulin and the dye conjugate were synthesized by Alexandra Hauser-Kawaguchi. Characterization by IR, absorbance, dynamic light scattering, NMR, and MALDI were done by Alexandra Hauser-Kawaguchi. The ESI-MS of inulin was obtained by Megan Kelman. *In vivo* evaluation was carried out by Jennifer Hadway and her team of animal technicians with resources provided by Dr. Ting Lee. Fiona Lee processed all data obtained through the course of *in vivo* studies with resources provided by Dr. Ting Lee.

Acknowledgments

First and foremost, thank you to my supervisor, Len, for being hugely supportive and encouraging both in and out of the lab. Thank you for trusting me with everything related to the RHAMM project and with Novare. You saw something in me and nurtured my growth as a scientist and as a person. I'm not sure where my future lies, but I'm sure that I'll never find another boss who loves skiing as much as I do, and because of that, your shoes will be hard to fill!

Thank all of the members of the Luyt group, both past and present, who have helped make memories and shape my time in the lab. To Aagam and Will, I could not have asked for a better start to grad school than with you two. To Megan Kelman, thank you for making SPR experiments enjoyable, and for your help with everything Mass Spec-related. A very special thank you to Mark Milne, who looked out for me since he joined the lab, and continues to do so now that he has left!

A very special thank you to Dr. Eva Turley and her entire lab for their support and contribution to this thesis. Eva, thank you for all of your constant guidance, patience, and support. Conny, thank you for always listening to me and commiserating with me. Teresa, thank you for secretly working on the bioassays that eventually strengthened the story and made it what it is.

Thank you to Dr. Ting Lee and everyone in his lab for their collaboration in the Inulin project, particularly to Jenn Hadway and Fiona Lee. Ting, thank you for never completely losing hope in me and for all of your brilliant ideas.

Thank you to my entire ski family at Track 3! Track 3 was my home away from home for so much of the year and brought balance to my life. To all of the people who have helped make my time there as incredible as it was, thank you for nurturing my love of skiing and finding opportunities to help me grow. This 'starving student' couldn't have made it through her PhD without you! Special thanks to Marc Mitchell, Jamie Spencer, Mike Mahler, Don Campbell, and Dan Elliot for always being on-call to help me get into a sit ski!

To everyone at 343 Balderstone Ave, thank you for bringing me into your home and adopting me as one of your own. Lola, Nina, Geoff, Spencer, Mason, and honorary Balderstone resident, Sandi, you have all made my journey through this PhD a little bit easier. Thank you for taking care of me when I was sick or dealing with dental nightmares, for treating me to home cooked meals, and most of all, for encouraging me on a daily basis. A special thank you to Nina for everything that you have done for me from the first day that we met. You have gone above and beyond, and I feel so lucky to have someone as special as you as my second mama!

To my Little Sister, Rachelle, I am so thankful that you came into my life all those years ago, and that our relationship was able to able to develop into a true sisterhood. To Vicky and Mike Belair, thank you from the bottom of my heart for trusting me with Rachelle, and for welcoming me into your home.

Thank you to all of the wonderful people that I am able to call my friends! A very special thank you to the friends I left behind in Toronto, who have supported every step of my journey without fail despite the distance and the time apart. To Octavian Maciu, thank you for being the Opa to my Oma, and for being the most reliable shoulder to lean on for over 10 years, despite the ocean that separates us – "Jtm mit umlaut und Kartoffeln!" To Sarah Wagner, thank you for finding me and for taking a chance on me, and to Dominique Ciccarelli, thank you for always tirelessly supporting my growth and having my back!

Thank you to Sylvester Oleszkiewicz, whose memory I will always hold onto dearly. You were more than a neighbour. You were my grandfather when I lost mine, my Bridge teacher, my friend, and an unconditional supporter of my education. Thank you for your wise stories, your witty jokes, your support, and your friendship.

To my family: thank you for always pushing me to be the best version of myself and for believing in my abilities. I may have laboured for 5 years, but I could not have done it without your unconditional love and support. Thank you to my mother, Gabriele Hauser, for always sending me back to London with a week's worth of her delicious food, for being my partner in world travel, for being my biggest critic, but also my biggest supporter. To my father, Ken Kawaguchi, for always looking after my car and making sure that I have every practical tool under the sun, and for finding the best birthday cards. To both of my parents, thank you for instilling within me the drive needed to achieve this PhD. To my Oma, Maria Hauser, Grandma, Yaeko Kawaguchi, and aunt, Diane Kawaguchi, thank you for constantly believing in me and supporting me despite having little idea of what I have spent the last few years doing. Lastly, to my partner in crime, Ruben Flam-Shepherd, thank you for being available and supportive when I needed it most, for believing in me more than I believed in myself, for understanding my priorities, for reminding me that it is all worth it, and for always letting me win.

To my entire family, this PhD belongs to all us!

Table of Contents

List of Tables

List of Figures

List of Schemes

List of Supplemental Information

List of Abbreviations

CD: Circular dichroism

CKD: Chronic kidney disease

Cy7.5: Cyanine 7.5

DMEM: Dulbecco's Modified Eagle Medium

DIPEA: N, N-Diisopropylethylamine

DMF: Dimethylformamide

DMSO: Dimethylsulfoxide

ECM: Extracellular matrix

eGFR: Estimated glomerular filtration rate

ERK1,2: Extracellular signal-regulated kinase 1,2

ELISA: Enzyme-linked immunosortbent assay

FBS: Fetal bovine serum

FL: Full-length

Fmoc: 9-fluorenylmethoxycarbonyl

GAG: Glycosomaminoglycan

GFR: Glomerular filtration rate

GPI: Glycosylphosphatidylinositol

GST: Glutathione S-transferase

HA: Hyaluronan, Hyaluronic acid

HABD: Hyaluronan binding domain

HATU: 1-[Bis(dimethylamino)methylene]-1H-1,2,3-triazolo[4,5-b]pyridinium 3-oxid hexafluorophosphate

HCTU: 2-(6-Chloro-1-H-benzotriazole-1-yl)-1,1,3,3-tetramethylaminium hexafluorophosphate

Hmb: 2-hydroxy-4-methoxybenzyl

HMW: High molecular weight

HPLC: High-performance liquid chromatography

HRP: Horseradish peroxidase

k_a: rate constant of association

k_d: rate constant of dissociation

k_m: rate constant of mass transport

LSPR: Localized surface plasmon resonance

MAP: Microtubule-associated protein

MAPK: Mitogen activated pathway kinase

MBHA: 4-methylbenzhydrylamine

MDRD: Modification of Diet in Renal Disease

MMP: Matrix metalloproteinase

m/z: mass over charge ratio

NTA: Nitrilotriacetic acid

OBOC: One-bead one-compound

PBS: Phosphate buffered saline

PDB: Protein Data Bank

ROS/RNS: Reactive oxygen species/Reactive nitrogen species

RHAMM: Receptor for hyaluronan mediated motility

SAR: Structure-activity relationship

SPPS: Solid-phase peptide synthesis

SPR: Surface plasmon resonance

TBME: Tert-butyl methyl ether

TBS: Tris-buffered saline

TFA: Trifluoroacetic acid

TFE: Tetrafluoroethylene

TIPS: Triisopropylsilane

TMB: Tetramethylbenzidine

TPX2: Targeting protein for Xklp2

UHPLC: Ultra high-performance liquid chromatography

Ce qui embellit le désert, dit le petit prince, c’est qu’il cache un puits quelque part.

“What makes the desert beautiful,” said the little prince, “is that somewhere it hides a well.”

– Antoine de Saint Exupéry, Le Petit Prince

Chapter 1

1 Introduction

1.1 Hyaluronan

Hyaluronan (HA) is a simple linear extracellular matrix polysaccharide that belongs to the glycosaminoglycan (GAG) family of macromolecules and consists of dimeric repeats of N-acetylglucosamine followed by D-glucuronic acid (**Figure 1.1**). In homeostatic tissues, the majority of HA occurs in its high molecular weight (HMW) and native form (e.g. >500 kDa), which is organized into scaffolds and matrices of the extracellular matrix (ECM) [1, 2], making it a ubiquitous component of the ECM. The ECM environment is tightly regulated during normal physiological conditions, providing important structural and biochemical support to surrounding cells [3, 4]. Its functions are understudied, but at a minimum, it promotes tissue hydration, provides lubrication, protects against mechanical damage, reduces proliferation, modulates immune recognition, promotes expression of anti-inflammatory cytokines, and blocks macrophage functions, such as phagocytosis [3, 5-10]. In contrast to homeostatic tissues, HA polymer size in remodeling and diseased tissues is strikingly polydisperse, ranging from <10 kDa to >500 kDa [11]. HA fragments are generated by reactive oxygen/nitrogen species (ROS/RNS) and hyaluronidases that are produced during tissue stress and repair [5-9, 12-14]. Fragmentation of polymeric HA drastically alters the functions of HA. Short HA fragments are reported to promote pro-inflammatory cytokine expression/release as well as regulate innate immune cell proliferation [15-17]. Thus, the specific function of HA depends on the precise polymer size and the type of cell responding to the fragments [18-21]. HA fragments activate multiple receptors, triggering different downstream events depending upon the injury or disease context [2, 15, 22-25]. HMW HA binds to CD44, while smaller fragments of HA bind to receptor for hyaluronan mediated motility (RHAMM) [2]. It has been suggested that HA fragments can also inhibit the binding of higher molecular weight HA to CD44 [2, 26, 27]. Thus, fragmented HA could impact tissues by either directly binding specific receptors or by acting as an antagonist such that they prevent the binding of larger HA polymers to their cognate receptors. These complex interactions control a variety of signaling pathways that regulate cell adhesion/motility, mitotic spindle integrity and transcriptomes.

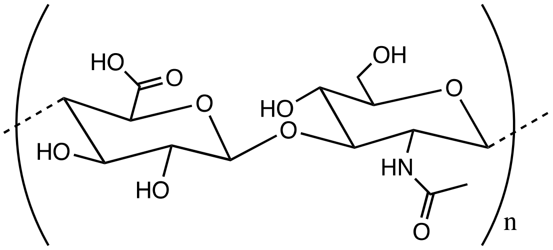

Figure 1.1. Structure of hyaluronan, depicting the dimeric repeat of D-glucuronic acid and N-acetyl glucosamine

1.2 Receptor for hyaluronan mediated motility (RHAMM)

RHAMM (gene name HMMR) is a largely hydrophilic protein that was originally isolated from embryonic chicken heart explant cultures exhibiting high HA production and increased cell migration. It is one of a number of HA receptors that are expressed on immune cells that bind to complex mixtures of HA polymer sizes and activate pathways required for an inflammatory or tumorgenic response. RHAMM exists in two populations: intracellularly, where it exists in both the nucleus and the cytoplasm, and extracellularly, where it is a cell surface glycosylphosphatidylinositol (GPI) linked protein. RHAMM expression is tightly regulated and limited during homeostasis; however, RHAMM mRNA expression transiently increases in response to injury or cellular stress, such as inflammation and cancer, resulting in increased receptor protein expression and export to the cell surface. Cell surface RHAMM is a HA co-receptor with CD44, and the interaction between the three molecules stimulates the activation of the mitogen activated pathway (MAPK) or the Ras-Mek-ERK pathway and the transcription of genes involved in cell motility, differentiation and proliferation in pro-inflammatory microenvironments (**Figure 1.2**) [28]. Thus, the specific inhibition of HA-RHAMM interactions could have significant therapeutic potential in cancer and other diseases.

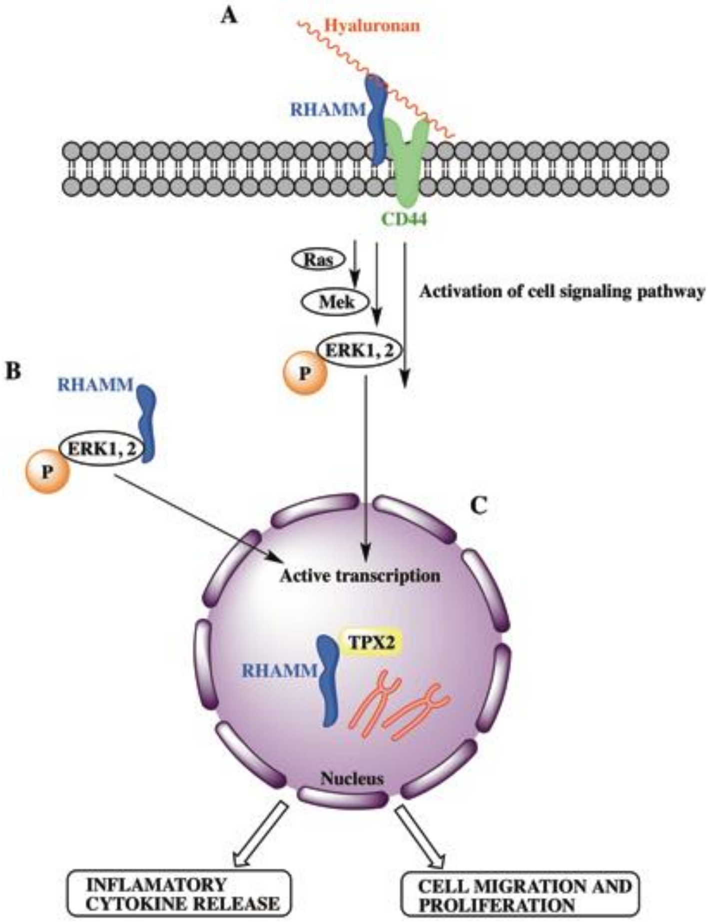

Figure 1.2. The interaction between cell surface RHAMM and HA activates the Ras-Mek-ERK pathway, and the phosphorylation of ERK1,2, which results in active transcription of mitogenic genes (A). Increased cytoplasmic RHAMM expression also results in phosphorylation of ERK1,2, and therefore, the transcription of mitogenic genes (B). Increased nuclear RHAMM expression results in aberrant mitotic activity and genomic instability (C). All of these increases in RHAMM expression result in the release of inflammatory cytokines and cellular migration and proliferation. Adapted from [29].

RHAMM interacts with HA via two HA binding domains (HABDs) located near the protein's carboxyl terminus, each of which has a BX_7B binding motif, where B represents any basic residue and X represents any non-acidic residue [4]. These clusters of basic residues allow for ionic interactions with the carboxylate ions of HA [4].

In addition to being a cell surface receptor for HA, RHAMM binds to extracellular-regulated kinase (ERK) kinase, and regulates the expression of ERK [30]. ERK has two closely related isoforms (ERK1 and -2) that are required for cellular differentiation and proliferation [28, 30]. RHAMM is also a microtubule-associated protein (MAP) that binds directly to microtubules and interacts with TPX2, a different MAP that is required for microtubule formation [31]. RHAMM localizes to the centrosome, where it interacts with tubulin and helps to maintain mitotic spindle integrity and polarity [32] (**Figure 1.3**). TPX2 initiates the formation of microtubules at the kinetochore, and activates Aurora kinase A (AURKA), which accumulates at the centrosome from S phase to the end of mitosis and facilitates the formation of microtubules [33-35]. This results in centrosome maturation and spindle assembly [33]. High expression of AURKA results in aberrant mitotic spindle formation, and is, therefore, correlated with genetic instability and poor prognosis in human diseases [36].

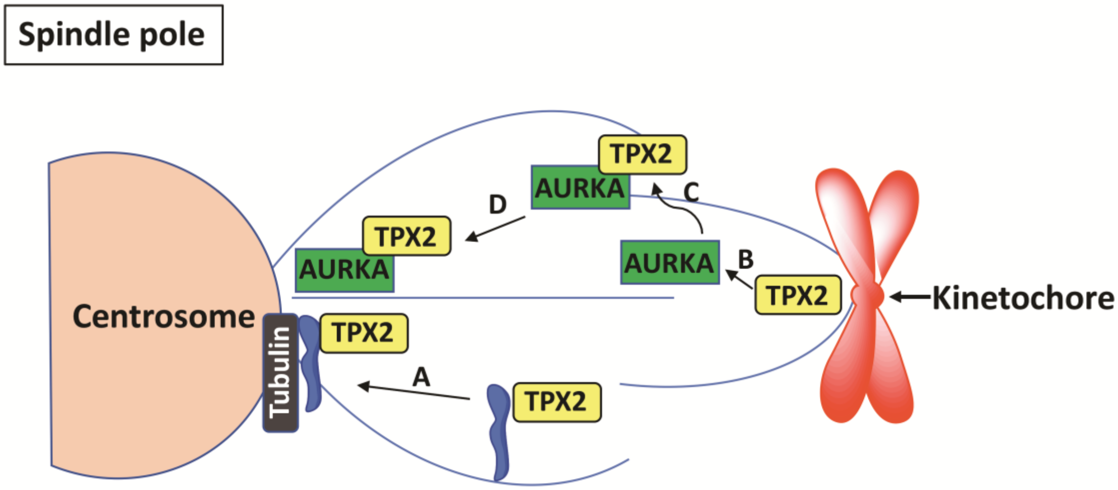

Figure 1.3. RHAMM binds to microtubules and TPX2, and localizes at the centrosome, where it also binds to tubulin (A). TPX2 initiates the formation of microtubules at the kinetochore and activates AURKA (B). AURKA complexes with TPX 2 (C) and accumulates at the centrosome (D). Adapted from [32].

While RHAMM expression is tightly regulated or absent in most tissues, it is important for a number of wound repair processes that require cell migration, invasion, and remodelling of the ECM. Its restricted expression makes it a potential target for cancer and wound repair therapy with low toxicity. RHAMM peptides are currently being tested in phase II clinical trials for multiple myeloma and myelodysplastic syndrome and are showing efficacy and low toxicity in patients [37, 38].

1.3 Peptide synthesis

Peptides can be synthesized chemically by two main techniques, solid phase peptide synthesis (SPPS) and solution phase peptide synthesis. Solution phase peptide synthesis can be more problematic than its solid phase counterpart, as dimerization and the formation of other unwanted by-products requires the purification after the addition of each amino acid.

In the early 1960s, Merrifield pioneered the idea of SPPS, using a polystyrene-based solid support for peptide synthesis, which would deal with the difficulties associated with solution phase synthesis [39]. The technique of solid phase peptide synthesis covalently links the peptide chain to an insoluble resin, which acts as a solid support off of which the peptide chain can grow or elongate. The solid support facilitates the addition of excess soluble reagents in order to drive each reaction to completion, and the excess reagents can be easily removed by multiple washing and filtration steps, eliminating the need for tedious purification steps after the addition of each amino acid [39]. Following synthesis, the crude peptide is released from the solid support and purified by traditional HPLC methods, with higher yields often reported for SPPS than for solution phase methods [39]. SPPS can be performed either manually or using an automatic peptide synthesizer, which is convenient, and improves throughput.

Peptide synthesis by the SPPS strategy is carried out in a stepwise procedure that builds the peptide chain from the C- to the N-terminus using Nα- protected amino acids. The first amino acid is loaded onto the resin, which is functionalized with linkers for easy loading, and the chain is elongated as subsequent amino acids are coupled together. Once the peptide has been synthesized in its entirety or the desired peptide length has been achieved, it can be removed from the resin, yielding the free and linear peptide (**Figure 1.4**). Similarly, the synthesis can be monitored by LC-MS at any point during the synthesis by removing a small aliquot of resin and cleaving the peptide off of it.

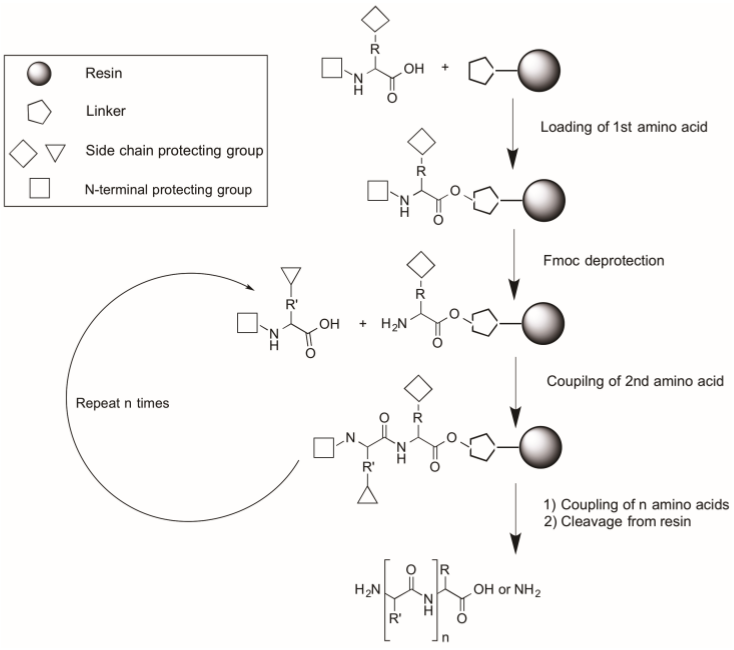

Figure 1.4. General scheme of solid-phase peptide synthesis

Successful SPPS depends on the choice of resin used. Resins are insoluble polymers that are pre-loaded with varying linkers, which provide flexibility during synthesis, and allow for control over the final product by determining the functionalization of a cleaved peptide [40]. For example, Rink amide resins are functionalized with an amine group that covalently binds to the first amino acid in the sequence to obtain an amide bond at the carboxyl terminus of the peptide. In addition, resins can have different substitution levels, which when decreased, facilitate the synthesis of long peptides by avoiding interchain crowding, resulting in improved the synthetic yields [41].

One of the most common methods for synthesizing peptides by SPPS is through the 9-fluorenylmethoxycarbonyl (Fmoc) strategy, which was first introduced by Carpino and Han in 1970, in which amino acids are N-terminally protected [42]. This method employs an orthogonal scheme that allows the removal of only the N-terminal Fmoc protecting group without disrupting the remainder of the peptide. This is accomplished by mild basic conditions for the removal of the Fmoc group from each amino acid in order for the next amino acid to be added, and by the strong acidic conditions that are required to liberate the peptide from the resin, as well as remove all of the acid-labile side-chain protecting groups.

Fmoc-based SPPS is carried out as depicted in **Scheme 1.1**. A protected amino acid is added to the resin through standard coupling procedures to form an amide bond. The N-terminal Fmoc group of the amino acid is then deprotected with piperidine, resulting in a free amine. The remainder of the peptide sequence is built following the same procedure until the final peptide length is acquired. The free peptide is then obtained by treatment of the resin with acid in order to simultaneously deprotect amino acid side chains and remove the peptide from the solid support.

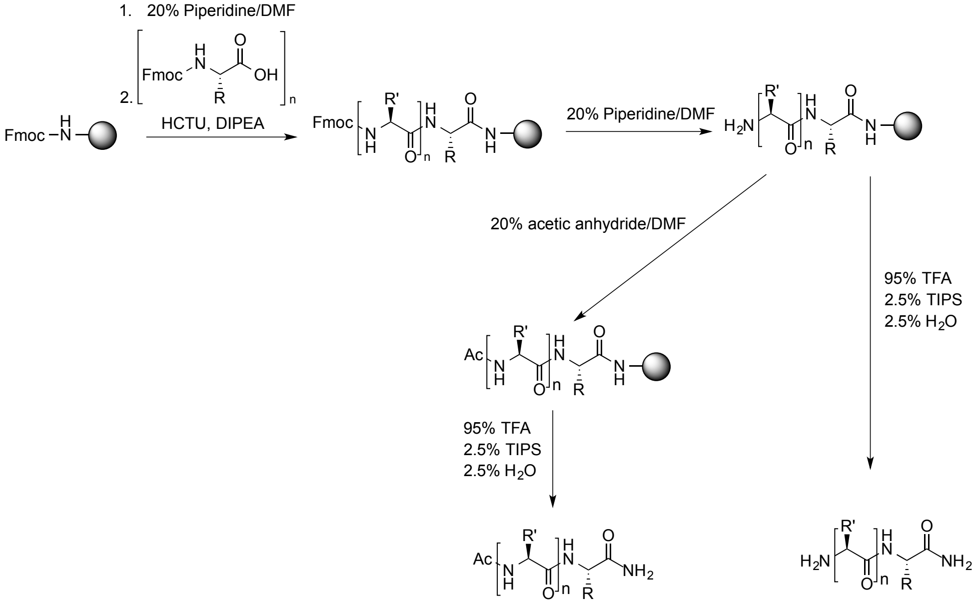

Scheme 1.1. Fmoc-based solid-phase peptide synthesis

1.4 Rational design of peptides

Targeting a protein-polysaccharide or protein-carbohydrate interaction is often challenging, as there is a large surface area of interaction and a lack of well-defined binding pockets that prevent the use of small molecules for interfering with these binding interfaces and inhibiting the interaction. Similarly, a challenge exists in trying to develop mimics that contain the specific multivalences that will foster interaction with its target [43]. This is further complicated by the conformational changes that these HA receptor proteins undergo upon binding to HA [44]. Higher molecular weight entities such as peptides, proteins, and antibodies are more readily able to block protein-polysaccharide interactions due to their ability to interact over a larger surface area.

The discovery of peptides that modulate protein-carbohydrate interactions has focused largely on two approaches: unbiased or random peptide library screening and rational design based upon known structure or binding sites. Unbiased peptide library screening has used phage display, which is a biochemical approach to identify high affinity peptides displayed on a bacteriophage, and one-bead one-compound (OBOC) libraries, which is a chemical approach of screening peptides using polymer beads. These unbiased peptide libraries were primarily used for identifying peptide mimetics that scavenge HA and HA fragments. The discovery approaches used for finding HA binding peptides that mimic HA receptors have primarily been based upon rational design, with many structural leads being derived from RHAMM's known binding sites for HA.

In many cases, the rational design of targeting peptides can start with a known crystal structure of the peptide, which provides important information on the compound's secondary and tertiary structure [45]. Based on the initial crystal structure, alanine scans, small focused libraries, and structure-activity relationship (SAR) studies are carried out in order to identify the essential amino acids and sites for possible modification. This process allows for the identification of those amino acids that are unstable and susceptible to events such as isomerization, glycosylation, or oxidation [46]. In addition to optimizing the peptide's sequence, rational design involves improving the physicochemical properties of natural or native peptides. This is often carried out by introducing structural constraints, such as staples to cyclize the peptide the backbone, and unnatural amino acids for use as pharmacologically active building blocks. Rational design of a compound must account for target affinity and specificity, biological stability, and its pharmacological and pharmacodynamics properties [45].

1.5 Peptides as therapeutics

Targeting a specific receptor or other class of target can be achieved with a number of different classes of molecules, including small molecules, peptides, or antibodies. There are advantages and disadvantages to using the different classes of compounds. Small molecules have relatively low molar mass, and therefore, can access many biological targets in the body. In addition, small molecules are not easily recognized or degraded by enzymes; however, they unfortunately suffer in lipophilicity, and because of their small surface area, suffer from nonspecific interactions, which can lead to toxicity [47]. Peptides, on the other hand, can be synthesized by standard synthetic protocols, and improvements in manufacturing technology have allowed for peptides of various length ranges up to 40 amino acids to be synthesized, as well as quick and easy synthesis of peptide analogues [48, 49].

Peptide-based drugs are generally shorter than 50 amino acids in length, with molecular weights that lie between those of small molecules and large biologics [50]. Peptides as a class of molecule are particularly attractive as drug candidates because they are biocompatible with typically low toxicity, structurally diverse permitting high selectivity and potency, and have a predictable metabolism [51]. These features have enabled peptides to have high affinity for their targets at nanomolar and picomolar concentrations. Unfortunately, peptides suffer from a relatively short circulating half-life because they are susceptible to the same digestive enzymes designed to break down amide bonds of ingested proteins, and can be cleaved by both endopeptidases and exopeptidases. As a result, they have poor oral bioavailability and are quickly eliminated [45]. In addition, they are prone to hydrolysis and oxidation, and have low membrane and tissue permeability due to their polarity and relatively high molecular weight [45]. However, there has been an increasing number of commercially available unnatural amino acids and strategies that have helped improve the stability and other physical properties of peptides. For example, the identification of possible cleavage sites within the peptide sequence and the substitution of relevant amino acids is a preliminary approach to limiting enzymatic degradation of the peptide. Novel synthetic strategies supplement this, including modifications to amino acids or the peptide backbone, the incorporation of unnatural amino acids, the conjugation of additional moieties that extend half-life or improve solubility, and cyclization of the peptide backbone with synthetic structural constraints, which may stabilize the peptide's secondary structure [48, 52].

1.6 Current peptide mimetics that inhibit RHAMM-HA interactions

1.6.1 Rationally designed peptide mimetics

To date, several peptide mimetics have been rationally designed to interfere and block the HA-RHAMM interaction. RHAMM-sequence based peptide mimetics that bind to HA fragments and have been shown to have therapeutic effects in a number of processes, including inflammation, wound repair, and fibrosis/adipogenesis. One of the first rationally designed HA-binding peptides was based on the RHAMM BX_7B HA binding motif, but does not otherwise have any amino acid sequence homology with RHAMM. This peptide strongly reduced BAL macrophages in bleomycin-induced lung injury and blunted destruction of lung architecture [53], reduced surfactant protein A-induced macrophage chemotaxis [54] and ozone induced lung hyper-responsiveness [55]. Another peptide, pep-35, has 70% homology with the RHAMM sequence and essentially joins four RHAMM HA binding sequences together. This peptide reduced *Staphyloccus aureus* burden in infected surgical wounds and increased the production of CXCL1,2 by inflammatory cells, which subsequently increased neutrophil influx into the wound [56]. Other peptides have been designed to mimic the three BX_7B motifs of CD44 and were shown to block tumor cell growth [57]. Finally, RHAMM sequence mimics (NPI-0102, NPI-0104), which disrupt HA binding to RHAMM, were reported to promote adipogenesis and reduce tissue fibrosis [58] by increasing the production of adiponectin, an anti-fibrogenic adipokine [59, 60].

In another rationally designed approach, Esguerra et al. developed HA peptide mimics from the C-terminal region of α- and β-tubulin that bind to RHAMM [61]. Novel 12mer peptide ligands were identified that bind with high affinity (nM) to RHAMM and block HA binding to tumor cells [61]. The strongest binding compounds were taken from the negatively charged carboxy terminal tail (CTT) and the helix H12 regions of tubulin, and those that contained a repeating amino acid motif of EEXEE, suggesting that both electrostatic forces and conformational effects may be important for the development of RHAMM-binding ligands.

Other RHAMM peptide-based therapies could reasonably be developed from varying the peptide backbone and/or altering the peptide structure, which may confer improved specificity and affinity towards its target. Such strategies include the development of stapled or cyclized peptides, resulting in more drug-like compounds.

1.6.2 Peptide library screening for HA- and HA receptor-binding

In addition to rational design, many peptides with therapeutic potential were discovered through peptide library screenings. The P15-1 peptide (STMMSRSHKTRSHHV) is a 15mer peptide, which was the first peptide mimetic that was reported to bind specifically to HA fragments of <10 kDa. It was identified by screening a recombinant phage display library with a complexity of approximately 10^{13} transformants for peptides that both bind to HA fragments (MW range 5-200 kDa) linked to Sepharose beads and that block cell motility [62]. Two peptide sequences were recovered in the screen and of these, P15-1 exhibited the highest affinity for HA fragments ($K_D = 10^{-7}$ M), and most strongly blocked cell motility. It has low homology with known HA receptors but contains a BX_7B motif similar to that required for binding of HA to RHAMM [4]. In a model of excisional skin injury, P15-1 blunted inflammation and fibrogenesis [62]. Consistent with the proposed possibility that P15-1 blocks RHAMM signaling though HA fragments, the consequences of this peptide mimetic on skin wound repair is similar to that of the genetic deletion of RHAMM [28], which results in blunted responses to HA fragments [63]. For example, both conditions block inflammation and fibrogenesis in excisional wounds but neither affect the course of incisional wound repair, which does not involve the massive waves of cellular trafficking and migration that are required for the healing of excisional wounds [28, 64, 65]. P15-1 synthesized entirely with D-amino acids (referred to as HABP42) also reduced bacterial burden in surgical skin wounds by modulating neutrophil responses [56, 66].

Pep-1, a 12mer peptide (GAHWQFNALTVR) was identified as an HA binding sequence by screening an M13 phage display library expressing random 12mer peptides fused to gene 3 (pIII) minor coat proteins with a complexity of approximately 10^9 transformants [67]. This peptide (Pep-1) was isolated by panning the library for sequences that bind to HA-coated plates. Pep-1 binds to HA with moderate affinity ($K_D = 1.4\ \mu M$), inhibits HA binding to innate immune cells, and was shown to inhibit leukocyte attachment to HA substrates [67, 68]. The systemic, subcutaneous or topical administration of this peptide inhibited dinitrofluorobenzene/oxazolone induced-contact hypersensitivity by blocking both the in-trafficking of inflammatory cells and the migration of dendritic cells out of the epidermis [67]. Skin dendritic cells utilize HA as a motogenic stimulus for migrating from the epidermis to lymph nodes, where they function as antigen-presenting cells, a process that is required for generating protective pro-inflammatory and tolerogenic immune responses during tissue injury [69, 70]. Aberrant activation of these cells contributes to inflammatory disease processes [70]. These results provided early support for the development of HA inhibitors for inflammatory disorders. Pep-1 was later shown to inhibit the production of fragmented HA-promoted chemokine MIP-2 by bone marrow macrophages [71], reduce bronchial inflammation [72], reduce pro-inflammatory cytokine production (TNF-α, IL-6, MMP13 and iNOS), and preserve cartilage architecture in a mouse model of collagen-induced arthritis [69, 73]. In addition, Pep-1 dramatically inhibited interleukin-2 (IL-2)-induced vascular leak syndrome (VLS) [74], which may be linked to its anti-inflammatory effects. P15-1 and Pep-1 have been useful in dissecting the signaling pathways that are regulated by HA fragments, and their efficacy in blocking inflammation in animal models propelled the development of peptide mimetics that block fragmented HA-induced activity that leads to disease.

Recombinant CD44 protein has also been used to screen peptide libraries [75]. In this study, a Ph.D.^{TM} -12 phage display peptide library with a peptide complexity of $2.7\text{x}10^{-9}$ transformants was screened using recombinant CD44 as bait. The screen isolated several peptides, one of which exhibited a $K_D = 7.5$ pM for recombinant CD44. However, none of the isolated peptides were tested for their ability to bind to the CD44 HA binding region or evaluated for functional effects. Nevertheless, these studies show that isolating peptides that bind to HA receptors is a viable approach for potentially developing novel inhibitors of HA receptor signaling.

Peptide-displaying phage and peptide library technology have also been used to identify peptides that mimic carbohydrates [76]. HA peptide mimics that bind with high affinity to recombinant RHAMM containing hyaluronan binding sequences, were originally identified by Ziebell, M. et al [77, 78]. Two libraries of 8mer peptides were designed to target recombinant RHAMM fragments, with one library consisting of peptides made of entirely random sequences. The second library was biased, with alternating acidic residues incorporated in every other position of the sequence, with the intention of mimicking the placement of the glucuronic acid moieties of HA [77]. Peptides from the unbiased (random) library bound to recombinant RHAMM in an HA fragment-dependent manner with µM to nM affinity, and exhibited some similarities with respect to regions of hydrophobic residues (e.g. PVY), but contained very few negatively charged amino acids. These peptides were then computationally modeled to evaluate their binding to an NMR-based model of RHAMM, from which residues within RHAMM were identified and theorized to stabilize RHAMM-HA interactions [78]. However, these peptides have not yet been reported to affect cellular functions.

1.7 Protein-Carbohydrate interactions

There are a number of proteins that bind glycosaminoglycan carbohydrates, and many of the binding partners have been studied extensively. Generally, the main interaction between GAGs and the proteins that bind them are strong ionic interactions between the highly acidic sulphate or carboxylate groups of the carbohydrates and the basic side chains of arginine, lysine, and to a lesser extent, histidine residues of the protein [79]. GAGs interact with those residues that are exposed and easily accessible on the surface of proteins. Aliphatic residues, including Ala, Gly, Leu, and Ile, and other hydrophobic residues, such as Pro, Phe, Met, and Trp, are usually buried on the inside of proteins, and therefore, do not appear to participate in sugar bonding, while more polar and charged residues, such as Asn, Asp, Glu, Gln, His, Arg, and Lys, have been shown by both structure and sequence-based statistical analysis to bind to non-sulfated carbohydrates [80-82], such as heparin and hyaluronan. It is common for clusters of basic amino acids to exist on proteins, which facilitates the protein's interaction with the negatively charged groups of the sugar. Heparin-binding proteins have been identified as having binding sites with sequences of XBBXBX or XBBBXXBX, where B is any basic residue, and X is any non-acidic residue [83]. Similar binding sequences have been observed in HA-binding proteins, such as RHAMM and CD44, both of which exhibit a BX_7B binding motif [4]. Depending on the secondary structure of the protein, it is possible that very few residues in these binding sequences actually contribute to or participate in binding. For example, when the binding domains are arranged in an alpha-helix, the basic residues are often found along one exposed face of the protein, resulting in an amphipathic helical arrangement [84]. Therefore, in order for an interaction to take place between linear carbohydrates, such as HA, and largely helical proteins, such as RHAMM, the positively charged residues arrange themselves so that they are on the same face of the protein segment (**Figure 1.5**).

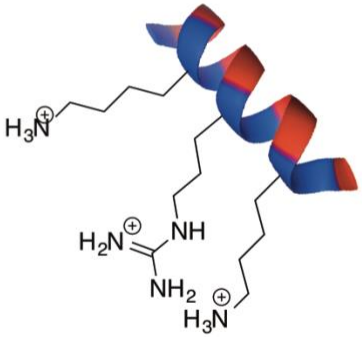

Figure 1.5. In an alpha-helix, the basic residues are often found along one exposed face of the protein, resulting in an amphipathic helical arrangement.

Biochemical assays are used to evaluate protein-carbohydrate interactions and can be carried out by chemically modifying the entities being evaluated, such as in the case of enzyme-linked immunosortbent assay (ELISA), or without modifying either entity, such as in the case of surface plasmon resonance (SPR). ELISA has the potential to be the more high-throughput method of screening, allowing the binding of several compounds to be evaluated simultaneously against either a single or multiple targets [85]. This assay requires that compounds be labeled or chemically modified, such as with a dye or biotin molecule, for signal readout. SPR, on the other hand, is a label-free method for evaluating biomolecular interactions, measuring single concentrations of compound at a single time, decreasing the throughput of measurement compared to ELISA. Despite this, label-free methods of evaluating the interaction between two compounds is especially important for small proteins or peptides, as secondary structure often influences binding, and chemically modifying these molecules can potentially alter their secondary structure. In addition, unlike ELISA, SPR delivers a kinetic analysis of the interaction in addition to the binding affinity in real-time, providing information on the association (k_a) and dissociation (k_d) phases of the interaction.

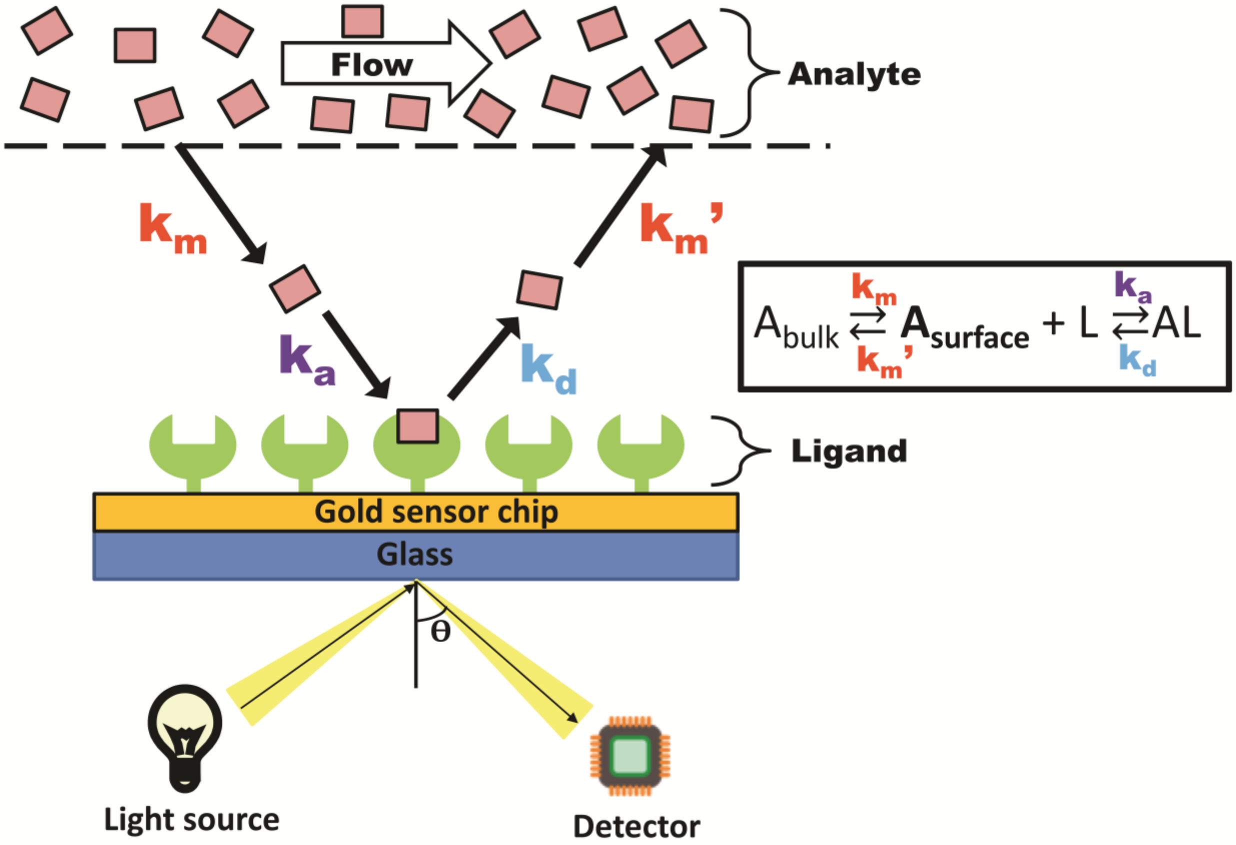

Figure 1.6. Analyte binding to the immobilized ligand at the sensor chip surface results in a change in resonance angle of reflected light. The Langmuir model with mass transport limitations describes the relationship between on (k_a) and off (k_d) rate constants, taking into account the rate at which analyte is brought from the bulk solution to the sensor chip surface. Adapted from Nicoya Lifescience.

The principle of SPR utilizes the immobilization of a compound of interest, known as the ligand, to a metal-coated sensor chip surface, and the measurement of changes in refractive index at the surface as another molecule, the analyte, binds. A light source shines light or a laser on the metal-coated film, reflecting with a resonance angle θ that shifts when a binding event occurs at the sensor chip surface, resulting from a change in refractive index (**Figure 1.6**). This shift depends on the mass and density of analyte at the chip surface. In this thesis, a variation of SPR, localized SPR (LSPR), was studied. LSPR differs from traditional SPR by using gold nanoparticles at the sensor chip surface instead of the continuous metal film used in traditional SPR. In addition, LSPR produces a strong resonance absorbance peak, with its position being highly sensitive to the refractive index localized around the nanoparticles. As a result, it measures changes in the wavelength of the absorbance position resulting from binding events rather than changes in angles (**Figure 1.7**), like is measured in traditional SPR.

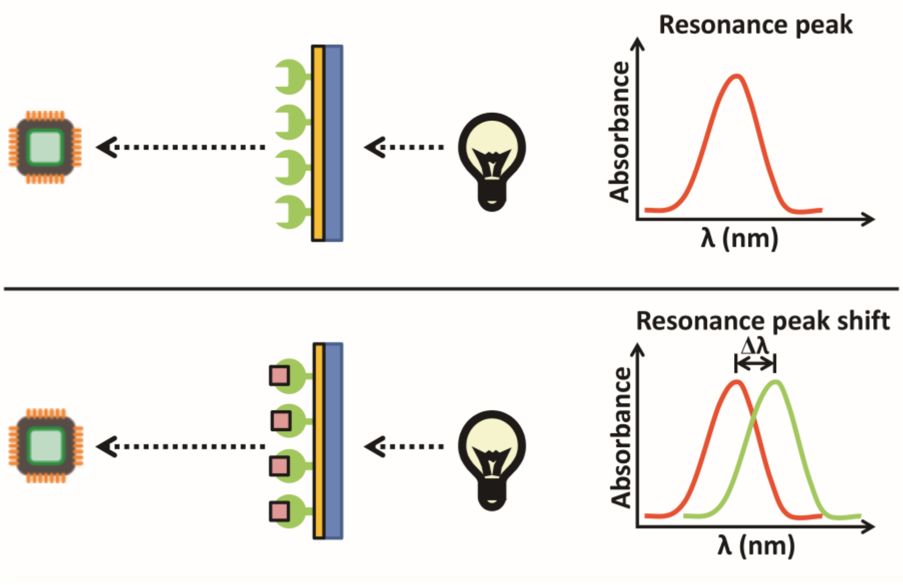

Figure 1.7. Analyte binding causes a shift in wavelength of absorbance position in localized SPR (LSPR). Adapted from Nicoya Lifesciences.

Following immobilization of the ligand to the sensor chip surface, the remaining binding sites are blocked in order to prevent non-specific interactions between the analyte and the chip surface. As the analyte flows across the immobilized ligand surface, and interacts or associates with it, it accumulates on the chip surface, resulting in a change in molecular weight at the chip surface, which is denoted by a change in signal. The rate of association between the two compounds depends directly on the on-rate of the interaction (k_a) and the mass transport of the analyte from the bulk flow to the sensor chip surface (k_m). Once the flow of analyte switches to buffer, the analyte dissociates from the chip surface, resulting in a decrease in signal (k_d). A strong ligand-analyte interaction requires the use of a regeneration buffer to completely remove analyte from the chip surface, while leaving the immobilized ligand in-place.

An important consideration in SPR is that tethering the ligand to the sensor chip surface will not disrupt its activity, prevent rotational freedom, or block any sites of binding. Therefore, the correct method of immobilizing one of the binding partners to the sensor chip surface is important. Biomolecule immobilization can be either direct, by covalent interaction with the sensor chip surface, or indirect, by binding to an immobilized capturing molecule [86]. Examples of direct immobilization include biotin-streptavidin interactions, gold-thiol interactions, and amine-carboxylic acid interactions. In many of these instances, orientation of these proteins is difficult to control, resulting in mixed orientations of protein on the surface, and the interaction can be so strong that regeneration of the sensor chip surface is not possible, such as with biotin-streptavidin interactions [87]. An alternative approach is to indirectly immobilize a biomolecule by labeling it with an oligo histidine tag (His tag) at either its C- or N-terminus, which interacts with nitrilotriacetic acid (NTA) that is pre-immobilized on the sensor chip. This method of attachment involves the capture of the His-tag protein by Ni^{2+} NTA chelation without altering secondary structure or blocking important analyte-binding residues, and allows for regeneration of the sensor chip. The exact immobilization chemistry depends on the specific interaction that is being evaluated.

1.8 Stapled peptides

1.8.1 Alpha-helices

Protein secondary structure is broken down into conformations that are in an alpha-helix, a beta-sheet, or a random coil. The Protein Data Bank (PDB) consist of approximately

62% alpha-helical proteins, suggesting that the alpha-helical conformation plays an important role in mediating a number of biological processes, including interactions with other proteins and macromolecules [52, 88].

There is a high energy requirement associated with organizing three consecutive amino acids into a helical conformation, which is referred to as the helix-coil transition theory [89]. Many short peptides lack a helical structure, as the energy required to organize them into well-defined helices is too great. However, pre-folding short peptides synthetically has the potential to overcome this energy barrier and can therefore facilitate the adoption of a stable secondary structure, such as an alpha-helix.

1.8.2 Stapled peptides

One complete turn of an alpha-helix is made up of 3.6 amino acids, resulting in the residues at positions i, i+4, and i+7 occurring on the same face of the helix [52]. Synthetically, the alpha-helical conformation of a peptide is carried out by introducing a covalent bond, or “staple”, at these amino acids positions, stabilizing the structure and inducing an alpha-helical conformation [90]. The positions of these staples can be important, however, and care must be taken in order to not replace or obstruct those residues that are important for binding to the target. Four methods for synthesizing stapled peptides have been extensively studied thus far, and include their formation by a lactam bridge, a hydrocarbon chain, a metal-ion clip, and a hydrogen bond surrogate [50, 52]. Staples formed by a hydrocarbon chain and lactam bridge are the preferred methods of peptide cyclization for the improvement in bioactivity and target recognition that they confer [91].

Staple formation in peptides depends on the linear peptide sequence and can only take place if the unfolded peptide sequence has the natural propensity to adopt an alpha-helical conformation. If the peptide sequence is unable to naturally adopt an alpha-helical conformation, it is possible that the side chains forming the staple will not arrange themselves appropriately, and therefore, will not bridge. Staple length depends on the size of the ring that is created following bridging, with shorter staples between side chains decreasing the peptide’s flexibility, and resulting in a more stable helix [90].

Amino acid side chains should produce a staple length or size that is large enough to not cause significant ring strain, and therefore, decrease the demand for activation energy for successful cyclization to be completed [92]. Side chains involved in creating the linker do not contribute to target recognition, and therefore, block at least one face of the helix once the staple is created.

A lactam bridge is created by means of an amide bond that forms between the side chains of two amino acids. Natural amino acids, glutamic acid or aspartic acid and lysine, are commonly applied to make the lactam bridge, but unnatural amino acids, such as ornithine and aminoadipic acid, can also be used. During synthesis, orthogonally-protected glutamic acid and lysine residues replace the amino acids of the natural peptide sequence in the appropriate positions (i.e. positions *i*, *i*+4, *i*+7, *i*+11). The peptide chain is built on resin following standard Fmoc-based SPPS procedures, allowing for the selective deprotection of the two amino acid side chains forming the lactam bridge, and their subsequent coupling to staple the peptide backbone and yield the cyclized product. Specifically, allylester and alloxycarbonyl protecting groups on glutamic acid and lysine side chains, respectively, are deprotected with palladium (0) catalyst under basic conditions, and the deprotected side chains are coupled together with a coupling agent, such as 1-[Bis(dimethylamino)methylene]-1H-1,2,3-triazolo[4,5-b]pyridinium 3-oxid hexafluorophosphate (HATU). The remainder of the peptide sequence can be modified as necessary, and eventually removed from the resin, with the staple intact (**Scheme 1.2**).

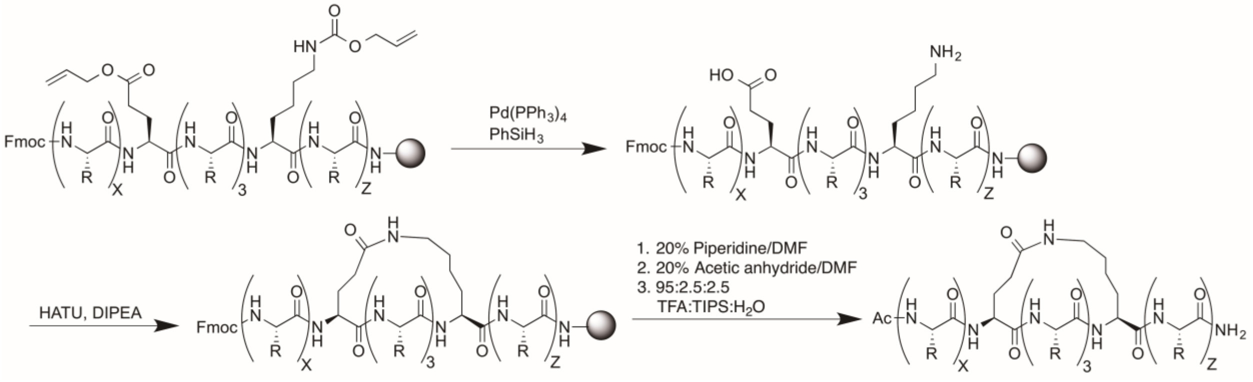

Scheme 1.2. General synthetic protocol for the formation of a lactam bridge between glutamic acid and lysine residues

1.8.3 Circular Dichroism spectroscopy

The secondary structure of proteins and peptides can be analyzed and quantified by analytical techniques, such as circular dichroism (CD) spectroscopy, which measures the extent to which asymmetric molecules can absorb right- and left-handed circularly polarized light [93]. The amide bonds in the primary sequence of proteins and peptides contain chromophores that produce different excitation interactions, resulting in identifiable characteristics on the spectra [94]. Each type of secondary structure produces a unique CD spectrum, which are blended together when different secondary structure elements exist within a single compound. The CD spectrum of a perfect alpha-helix (3.6 amino acids per turn) is characterized by two minima at 222 nm and 208 nm, and a maximum at 193 nm, but these signals may shift in wavelength or in intensity if the compound contains elements of β-sheet or random coil within its structure [94]. Many large proteins are made up of multiple secondary structure elements, and many small stapled peptides lack a perfectly stable secondary structure beyond the stapled sequence. In both of these cases, the CD spectrum is unlikely to reflect a perfect single secondary structure.

1.9 Glomerular filtration rate

Glomerular filtration rate (GFR) measures renal clearance, and can therefore, be a valuable tool in assessing kidney function and identifying the presence of chronic kidney disease (CKD) or other diseases that may target the kidneys. GFR may also be used for monitoring kidney function following kidney transplant, and therefore, identifying threats associated with organ rejection and nephrotoxicity.

The gold standard for measuring GFR is by directly measuring plasma clearance of a marker molecule or compound that filters freely through the glomeruli and is neither metabolized nor reabsorbed through the renal tubules. Inulin, a polysaccharide made of up of a single glucose unit and many fructose units, has been accepted as the marker of choice for quantifying GFR.

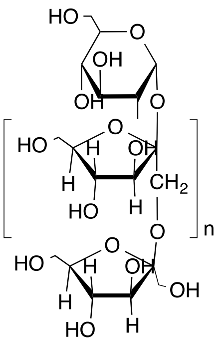

Figure 1.8. Structure of inulin

In the classic method for measuring clearance by Homer Smith, patients receive a continuous intravenous infusion of inulin following a period of fasting, multiple collections of blood and urine samples at precise times over 3 hours, and bladder catheterization in order to ensure complete urine collection [95]. Because this method of determining GFR is time-consuming, impractical, and invasive for patients, the clinical practice of using inulin has decreased, and the common clinical practice has been replaced with measuring the clearance of endogenous markers, such as serum creatinine levels, which provide an estimated GFR (eGFR) value quickly for clinical decision making using the Modification of Diet in Renal Disease (MDRD) Study equation [96] or the Cockcroft-Gault formula [97].

Cockcroft-Gault formula:

$$Creatinine\ clearance = \frac{(140 - age\ in\ years) \times (body\ weight\ in\ kg)}{(72 \times serum\ creatinine\ in \frac{mg}{dL})}$$

The value is multiplied by 0.85 if the individual is female.

MDRD formula:

$$GFR = 186.3 \times \left(creatinine\ level\ in \frac{mg}{dL}\right)^{-1.154} \times age^{0.203} \times 0.742\ (if\ female) \times 1.210 (if\ black)$$

Plasma levels of endogenous filtration markers, such as creatinine, are determined by their generation from cells and diet, renal excretion, including filtration through the glomeruli, and tubular secretion and reabsorption, and elimination by the gut and liver (**Figure 1.9**) [98]. Unfortunately, equations that estimate GFR consider only 4 variables: age, gender, race, and body weight. Factors that influence muscle mass or diet, changes in diet or muscle mass due to illness or amputation that are not considered, and differences in race other than those considered in the equation, result in inaccuracies that underestimate the normal physiologic GFR value.

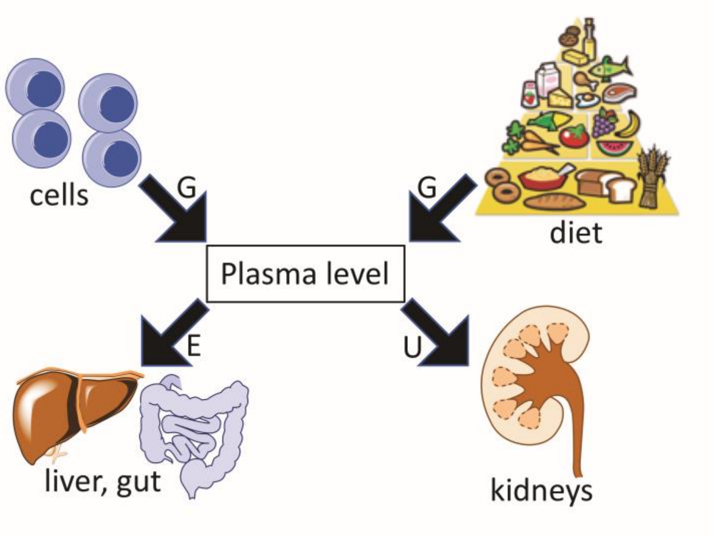

Figure 1.9. The plasma level of endogenous filtration markers depends on their generation (G) from cells and diet, elimination (E) by the liver and gut, and urinary excretion (U) by the kidneys. Urinary excretion includes filtration, tubular secretion and reabsorption. Under homeostatic conditions, U = G+E. Adapted from [98].

In order to improve the efficiency and accuracy of GFR measurements, several alternative exogenous tracer agents [98] have been developed, all of which allow for real-time measurement of kidney function by monitoring the decay of a bolus infusion of the reporter molecule from the plasma or the extracellular space over a period of time [99]. These alternative techniques include the use of radioisotope-labeled probes, such as ^{125}I-iothalamate [100], ^{51}Cr-ethylenediaminetetraacetic acid (EDTA) [101], and ^{99m}Tc-diethylenetriaminepentaacetic acid (DTPA) [102, 103], as well as non-radioactive probes, including iohexol [104], unlabeled iothalamate [105, 106], FITC-labeled sinistrin [107, 108], and FITC-labeled inulin [109, 110]. Methods for detecting these reporter molecules have included corometric assays, scintillation counting, X-ray fluorescence, HPLC, visible fluorescence, and two-photon intravital microscopy [99]. While many of these techniques are useful for developing and evaluating probes, they can be costly and are not easily translated to a clinical environment. In addition, these alternative probes have all been found to underestimate GFR, suggesting that they might be suffering from tubular reabsorption or plasma protein binding [98].

1.10 Rationale of thesis

This thesis will focus on two separate frameworks. The first framework encompasses chapters 2 and 3, studying the protein-carbohydrate interaction between RHAMM and HA and developing tools that inhibit it, while the second framework is discussed exclusively in chapter 4, involving a different carbohydrate, inulin, and the development of an optical agent based on it. Chapter 2 describes the chemical synthesis and optimization of a truncated RHAMM receptor, 7 kDa RHAMM, for use as the target receptor in screening and discovering novel peptide ligands. Chapter 3 describes the development of double stapled RHAMM peptide mimetics that bind HA with high affinity, and that are active in blocking inflammation both *in vitro* and *in vivo*. Chapter 4 describes the development of a dye-labeled inulin conjugate for measuring glomerular filtration rate by transcutaneous pulse dye densitometry and has been evaluated *in vivo* in farm-raised pigs.

1.11 References

1. Stern, R., Asari, A.A., and Sugahara, K.N., *Hyaluronan fragments: An information-rich system.* Eur J Cell Bio, 2006. **85**(8): p. 699-715.

2. Tolg, C., et al., *Hyaluronan and RHAMM in wound repair and the "cancerization" of stromal tissues.* BioMed Res Int, 2014. **2014**: p. 103923-103941.

3. Misra, S., et al., *Interactions between Hyaluronan and Its Receptors (CD44, RHAMM) Regulate the Activities of Inflammation and Cancer.* Front Immunol, 2015. **6**: p. 201.

4. Yang, B., et al., *Identification of a common hyaluronan binding motif in the hyaluronan binding proteins RHAMM, CD44 and link protein.* Embo J, 1994. **13**(2): p. 286-296.

5. Kavasi, R.M., et al., *HA metabolism in skin homeostasis and inflammatory disease.* Food Chem Toxicol, 2017. **101**: p. 128-138.

6. Schiraldi, C., et al., *Hyaluronan viscosupplementation: state of the art and insight into the novel cooperative hybrid complexes based on high and low molecular weight HA of potential interest in osteoarthritis treatment.* Clin Cases Miner Bone Metab, 2016. **13**(1): p. 36-37.

7. Litwiniuk, M., et al., *Hyaluronic Acid in Inflammation and Tissue Regeneration.* Wounds, 2016. **28**(3): p. 78-88.

8. Lauer, M.E., et al., *The Rise and Fall of Hyaluronan in Respiratory Diseases.* Int J Cell Biol, 2015. **2015**: p. 712507-712522.

9. Hull, R.L., et al., *Hyaluronan: A Mediator of Islet Dysfunction and Destruction in Diabetes?* J Histochem Cytochem, 2015. **63**(8): p. 592-603.

10. Schwertfeger, K.L., et al., *Hyaluronan, Inflammation, and Breast Cancer Progression.* Front Immunol, 2015. **6**: p. 236.

11. Tolg, C., et al., *Hyaluronan modulates growth factor induced mammary gland branching in a size dependent manner.* Matrix Biol, 2017. **63**: p. 117-132.

12. Cowman, M.K., et al., *Viscoelastic Properties of Hyaluronan in Physiological Conditions.* F1000Res, 2015. **4**: p. 622.

13. Monslow, J., Govindaraju, P., and Pure, E., *Hyaluronan - a functional and structural sweet spot in the tissue microenvironment.* Front Immunol, 2015. **6**: p. 231.

14. De la Motte, C.A. and Kessler, S.P., *The role of hyaluronan in innate defense responses of the intestine.* Int J Cell Biol, 2015. **2015**: p. 481301-481306.

15. Wight, T.N., et al., *Interplay of extracellular matrix and leukocytes in lung inflammation.* Cell Immunol, 2017. **312**: p. 1-14.

16. Viola, M., et al., *Extracellular Matrix in Atherosclerosis: Hyaluronan and Proteoglycans Insights.* Curr Med Chem, 2016. **23**(26): p. 2958-2971.

17. Lee-Sayer, S.S., et al., *The where, when, how, and why of hyaluronan binding by immune cells.* Front Immunol, 2015. **6**: p. 150.

18. D'Agostino, A., et al., *Is molecular size a discriminating factor in hyaluronan interaction with human cells?* Carbohydr Polym, 2017. **157**: p. 21-30.

19. Dong, Y., et al., *Endotoxin free hyaluronan and hyaluronan fragments do not stimulate TNF-alpha, interleukin-12 or upregulate co-stimulatory molecules in dendritic cells or macrophages.* Sci Rep, 2016. **6**: p. 36928.

20. Schaefer, L., *Complexity of danger: the diverse nature of damage-associated molecular patterns.* J Biol Chem, 2014. **289**(51): p. 35237-35245.

21. Werb, Z. and Lu, P., *The Role of Stroma in Tumor Development.* Cancer J, 2015. **21**(4): p. 250-253.

22. Avenoso, A., et al., *Hyaluronan in experimental injured/inflamed cartilage: In vivo studies.* Life Sci, 2017. 193: p. 132-140.

23. Maytin, E.V., *Hyaluronan: More than just a wrinkle filler.* Glycobiology, 2016. **26**(6): p. 553-559.

24. Garantziotis, S., et al., *The role of hyaluronan in the pathobiology and treatment of respiratory disease.* Am J Physiol Lung Cell Mol Physiol, 2016. **310**(9): p. L785-795.

25. Albeiroti, S., Soroosh, A., and de la Motte, C.A., *Hyaluronan's Role in Fibrosis: A Pathogenic Factor or a Passive Player?* Biomed Res Int, 2015. **2015**: p. 790203-79213.

26. Urakawa, H., et al., *Therapeutic potential of hyaluronan oligosaccharides for bone metastasis of breast cancer.* J Orthop Res, 2012. **30**(4): p. 662-672.

27. Ruppert, S.M., et al., *Tissue integrity signals communicated by high-molecular weight hyaluronan and the resolution of inflammation.* Immunol Res, 2014. **58**(2-3): p. 186-192.

28. Tolg, C., et al., *Rhamm-/- fibroblasts are defective in CD44-mediated ERK1,2 motogenic signaling, leading to defective skin wound repair.* J Cell Biol, 2006. **175**(6): p. 1017-1028.

29. Shigeishi, H., Higashikawa, K., and Takechi, M., *Role of receptor for hyaluronan-mediated motility (RHAMM) in human head and neck cancers.* J Cancer Res Clin Oncol, 2014: p. 1-12.

30. Zhang, S., et al., *The hyaluronan receptor RHAMM regulates extracellular-regulated kinase.* J Biol Chem, 1998. **273**(18): p. 11342-11348.

31. Maxwell, C.A., et al., *RHAMM is a centrosomal protein that interacts with dynein and maintains spindle pole stability.* Mol Biol Cell, 2003. **14**(6): p. 2262-2276.

32. Maxwell, C.A., McCarthy, J., and Turley, E., *Cell-surface and mitotic-spindle RHAMM: moonlighting or dual oncogenic functions?* J Cell Sci, 2008. **121**(7): p. 925-932.

33. Marumoto, T., Zhang, D., and Saya, H., *Aurora-A—a guardian of poles.* Nat Rev Cancer, 2005. **5**(1): p. 42-50.

34. Tulu, U.S., et al., *Molecular requirements for kinetochore-associated microtubule formation in mammalian cells.* Curr Biol, 2006. **16**(5): p. 536-541.

35. Shigeishi, H., et al., *Overexpression of the receptor for hyaluronan-mediated motility, correlates with expression of microtubule-associated protein in human oral squamous cell carcinomas.* Int J Onc, 2009. **34**(6): p. 1565-1571.

36. Fu, J., et al., *Roles of Aurora kinases in mitosis and tumorigenesis.* Mol Cancer Res, 2007. **5**(1): p. 1-10.

37. Greiner, J., et al., *High-dose RHAMM-R3 peptide vaccination for patients with acute myeloid leukemia, myelodysplastic syndrome and multiple myeloma.* Haematologica, 2010. **95**(7): p. 1191-1197.

38. Schmitt, M., et al., *RHAMM-R3 peptide vaccination in patients with acute myeloid leukemia, myelodysplastic syndrome, and multiple myeloma elicits immunologic and clinical responses.* Blood, 2008. **111**(3): p. 1357-1365.

39. Merrifield, R.B., *Solid Phase Peptide Synthesis. I. The Synthesis of a Tetrapeptide.* Journal of the Am Chem Soc, 1963. **85**(14): p. 2149-2154.

40. Guillier, F., Orain, D., and Bradley, M., *Linkers and cleavage strategies in solid-phase organic synthesis and combinatorial chemistry.* Chem Rev, 2000. **100**(6): p. 2091-158.

41. Tam, J.P. and Lu, Y.-A., *Coupling Difficulty Associated with Interchain Clustering and Phase Transition in Solid Phase Peptide Synthesis.* J Am Chem Soc, 1995. **117**(49): p. 12058-12063.

42. Carpino, L.A. and Han, G.Y., *9-Fluorenylmethoxycarbonyl function, a new base-sensitive amino-protecting group.* J Am Chem Soc, 1970. **92**(19): p. 5748-5749.

43. Holgersson, J., Gustafsson, A., and Breimer, M.E., *Characteristics of protein–carbohydrate interactions as a basis for developing novel carbohydrate-based antirejection therapies.* Imm Cell Biol, 2005. **83**(6): p. 694-708.

44. Banerji, S., et al., *Structures of the Cd44-hyaluronan complex provide insight into a fundamental carbohydrate-protein interaction.* Nat Struct Mol Biol, 2007. **14**(3): p. 234-9.

45. Fosgerau, K. and Hoffmann, T., *Peptide therapeutics: current status and future directions.* Drug Discov Today, 2015. **20**(1): p. 122-128.

46. Manning, M.C., et al., *Stability of protein pharmaceuticals: an update.* Pharm Res, 2010. **27**(4): p. 544-575.

47. Renukuntla, J., et al., *Approaches for enhancing oral bioavailability of peptides and proteins.* Int J Pharm, 2013. **447**(1-2): p. 75-93.

48. Lau, J.L. and Dunn, M. K., *Therapeutic peptides: Historical perspectives, current development trends, and future directions.* Bioorganic Med Chem, 2017. 26 (10): p. 2700-2707.

49. Behrendt, R., White, P., and Offer, J., *Advances in Fmoc solid-phase peptide synthesis.* J Pept Sci, 2016. **22**(1): p. 4-27.

50. Craik, D.J., et al., *The future of peptide-based drugs.* Chem Biol Drug Des, 2013. **81**(1): p. 136-147.

51. Nevola, L. and Giralt, E., *Modulating protein–protein interactions: the potential of peptides.* Chem Comm, 2015. **51**(16): p. 3302-3315.

52. Estieu-Gionnet, K. and Guichard, G. *Stabilized helical peptides: overview of the technologies and therapeutic promises.* Expert Opinion Drug Discov, 2011. **6**(9): p. 937-963.

53. Savani, R.C., et al., *A role for hyaluronan in macrophage accumulation and collagen deposition after bleomycin-induced lung injury.* Am J Respir Cell Mol Biol, 2000. **23**(4): p. 475-484.

54. Foley, J.P., et al., *Toll-like receptor 2 (TLR2), transforming growth factor-beta, hyaluronan (HA), and receptor for HA-mediated motility (RHAMM) are required for surfactant protein A-stimulated macrophage chemotaxis.* J Biol Chem, 2012. **287**(44): p. 37406-37419.

55. Garantziotis, S., et al., *Hyaluronan mediates ozone-induced airway hyperresponsiveness in mice.* J Biol Chem, 2009. **284**(17): p. 11309-11317.

56. Lee, J.C., et al., *Modulation of the local neutrophil response by a novel hyaluronic acid-binding peptide reduces bacterial burden during staphylococcal wound infection.* Infect Immun, 2010. **78**(10): p. 4176-86.

57. Xu, X.-M., et al., *A peptide with three hyaluronan binding motifs inhibits tumor growth and induces apoptosis.* Cancer Res, 2003. **63**(18): p. 5685-5690.

58. Bahrami, S.B., et al., *Receptor for hyaluronan mediated motility (RHAMM/HMMR) is a novel target for promoting subcutaneous adipogenesis.* Integr Biol, 2017. **9**(3): p. 223-237.

59. Marangoni, R.G. and Lu, T.T., *The roles of dermal white adipose tissue loss in scleroderma skin fibrosis.* Curr Opin Rheumatol, 2017. **29**(6): p. 585-590.

60. Park, P.H., Sanz-Garcia, C., and Nagy, L.E., *Adiponectin as an anti-fibrotic and anti-inflammatory adipokine in the liver.* Curr Pathobiol Rep, 2015. **3**(4): p. 243-252.

61. Esguerra, K.V., et al., *Identification, design and synthesis of tubulin-derived peptides as novel hyaluronan mimetic ligands for the receptor for hyaluronan-mediated motility (RHAMM/HMMR).* Integr Biol, 2015. **7**(12): p. 1547-1560.

62. Tolg, C., et al., *A RHAMM mimetic peptide blocks hyaluronan signaling and reduces inflammation and fibrogenesis in excisional skin wounds.* Am J Pathol, 2012. **181**(4): p. 1250-1270.

63. Tolg, C., Telmer, P., and Turley, E., *Specific sizes of hyaluronan oligosaccharides stimulate fibroblast migration and excisional wound repair.* PLoS One, 2014. **9**(2): p. e88479.

64. Zhou, H., et al., *The progress and challenges for dermal regeneration in tissue engineering.* J Biomed Mater Res A, 2017. **105**(4): p. 1208-1218.

65. Sorg, H., et al., *Skin Wound Healing: An Update on the Current Knowledge and Concepts.* Eur Surg Res, 2017. **58**(1-2): p. 81-94.

66. Zaleski, K.J., et al., *Hyaluronic acid binding peptides prevent experimental staphylococcal wound infection.* Antimicrob Agents Chemother, 2006. **50**(11): p. 3856-3860.

67. Mummert, M.E., et al., *Development of a peptide inhibitor of hyaluronan-mediated leukocyte trafficking.* J Exp Med, 2000. **192**(6): p. 769-780.

68. Mummert, M.E., et al., *Synthesis and surface expression of hyaluronan by dendritic cells and its potential role in antigen presentation.* J Immunol, 2002. **169**(8): p. 4322-4331.

69. Mummert, M.E., *Immunologic roles of hyaluronan.* Immunol Res, 2005. **31**(3): p. 189-206.

70. Worbs, T., S.I. Hammerschmidt, and R. Forster, *Dendritic cell migration in health and disease.* Nat Rev Immunol, 2017. **17**(1): p. 30-48.

71. Morioka, Y., et al., *Cathelicidin antimicrobial peptides inhibit hyaluronan-induced cytokine release and modulate chronic allergic dermatitis.* J Immunol, 2008. **181**(6): p. 3915-22.

72. Uchakina, O.N., et al., *The role of hyaluronic acid in SEB-induced acute lung inflammation.* Clin Immunol, 2013. **146**(1): p. 56-69.

73. Campo, G.M., et al., *Combined treatment with hyaluronan inhibitor Pep-1 and a selective adenosine A2 receptor agonist reduces inflammation in experimental arthritis.* Innate Immun, 2013. **19**(5): p. 462-478.

74. Guan, H., Nagarkatti, P.S., and Nagarkatti, M., *Blockade of hyaluronan inhibits IL-2-induced vascular leak syndrome and maintains effectiveness of IL-2 treatment for metastatic melanoma.* J Immunol, 2007. **179**(6): p. 3715-3723.

75. Park, H.Y., et al., *Screening of peptides bound to breast cancer stem cell specific surface marker CD44 by phage display.* Mol Biotechnol, 2012. **51**(3): p. 212-220.

76. Fukuda, M.N., *Peptide-displaying phage technology in glycobiology.* Glycobiology, 2012. **22**(3): p. 318-325.

77. Ziebell, M.R., et al., *Peptides that mimic glycosaminoglycans: high-affinity ligands for a hyaluronan binding domain.* Chem Biol, 2001. **8**(11): p. 1081-1094.

78. Ziebell, M.R. and Prestwich, G.D., *Interactions of peptide mimics of hyaluronic acid with the receptor for hyaluronan mediated motility (RHAMM).* J Comput Aided Mol Des, 2004. **18**(10): p. 597-614.

79. Fromm, J., et al., *Pattern and spacing of basic amino acids in heparin binding sites.* Arch Biochem Biophys, 1997. **343**(1): p. 92-100.

80. Malik, A. and Ahmad, S., *Sequence and structural features of carbohydrate binding in proteins and assessment of predictability using a neural network.* BMC Struct Biol, 2007. **7**(1): p. 1.

81. Shionyu-Mitsuyama, C., et al., *An empirical approach for structure-based prediction of carbohydrate-binding sites on proteins.* Protein Eng, 2003. **16**(7): p. 467-478.

82. Taroni, C., Jones, S., and Thornton, J.M., *Analysis and prediction of carbohydrate binding sites.* Protein Eng, 2000. **13**(2): p. 89-98.

83. Cardin, A.D. and Weintraub, H., *Molecular modeling of protein-glycosaminoglycan interactions.* Arterioscl Thromb Vasc Biol, 1989. **9**(1): p. 21-32.

84. Gandhi, N.S. and Mancera, R.L., *The structure of glycosaminoglycans and their interactions with proteins.* Chem Biol Drug Des, 2008. **72**(6): p. 455-482.

85. Mashalidis, E.H., et al., *A three-stage biophysical screening cascade for fragment-based drug discovery.* Nat Protoc, 2013. **8**(11): p. 2309-2324.

86. Van Der Merwe, P.A., Harding, N. S. E., and Chowdhry, B. Z., ProteinLigand Interactions: Hydrodynamics and Calorimetry; Oxford University Press: Oxford, 2001; pp 137-170.

87. Fischer, M., Leech, A.P., and Hubbard, R.E., *Comparative assessment of different histidine-tags for immobilization of protein onto surface plasmon resonance sensorchips.* Anal Chem, 2011. **83**(5): p. 1800-1807.

88. Hill, T.A., et al., *Constraining cyclic peptides to mimic protein structure motifs.* Angew Chem, 2014. **53**(48): p. 13020-13041.

89. Poland, D. and Scheraga, H.A., *Theory of helix-coil transitions in biopolymers: statistical mechanical theory of order-disorder transitions in biological macromolecules*. 1978, New York: Academic Press.

90. Henchey, L.K., Jochim, A.L., and Arora, P.S., *Contemporary strategies for the stabilization of peptides in the α-helical conformation.* Curr Opin Chem Biol, 2008. **12**(6): p. 692-697.

91. Walensky, L.D. and Bird, G.H., *Hydrocarbon-stapled peptides: principles, practice, and progress: miniperspective.* J Med Chem, 2014. **57**(15): p. 6275-6288.

92. Fang, W., *Design and synthesis of novel linear and cyclic peptide ligands for kappa opioid receptors*. 2008, PhD thesis, University of Kansas.

93. Greenfield, N.J., *Using circular dichroism spectra to estimate protein secondary structure.* Nat Protoc, 2006. **1**(6): p. 2876-2890.

94. Greenfield, N.J. and Fasman, G.D., *Computed circular dichroism spectra for the evaluation of protein conformation.* Biochemistry, 1969. **8**(10): p. 4108-4116.

95. Smith, H.W., *Comparative physiology of the kidney.* JAMA, 1953. **153**(17): p. 1512-1514.

96. Levey, A.S., et al., *A more accurate method to estimate glomerular filtration rate from serum creatinine: a new prediction equation.* Ann Intern Med, 1999. **130**(6): p. 461-470.

97. Cockcroft, D.W. and Gault, H., *Prediction of creatinine clearance from serum creatinine.* Nephron, 1976. **16**(1): p. 31-41.

98. Stevens, L.A. and Levey, A.S., *Measured GFR as a confirmatory test for estimated GFR.* J Am Soc Nephrol, 2009. **20**(11): p. 2305-2313.

99. Wang, E., et al., *Rapid diagnosis and quantification of acute kidney injury using fluorescent ratio-metric determination of glomerular filtration rate in the rat.* Am J Physiol Renal Physiol, 2010. **299**(5): p. F1048-F1055.

100. Thomaseth, K. and Amici, G., *Optimal design of a two-sample test for assessing [125I] iothalamate plasma clearance in peritoneal dialysis.* Nephrol Dial Transplant, 1998. **13**(9): p. 2265-2270.

101. Brändström, E., et al., *GFR measurement with iohexol and 51Cr-EDTA. A comparison of the two favoured GFR markers in Europe.* Nephrol DIal Transplant, 1998. **13**(5): p. 1176-1182.

102. Rabito, C.A., et al., *Noninvasive, real-time monitoring of renal function: the ambulatory renal monitor.* J Nucl Med, 1993. **34**(2): p. 199-207.

103. Rabito, C.A., et al., *Noninvasive, real-time monitoring of renal function during critical care.* J Am Soc Nephrol, 1994. **4**(7): p. 1421-8.

104. Schwartz, G.J., et al., *Glomerular filtration rate via plasma iohexol disappearance: pilot study for chronic kidney disease in children.* Kidney Int, 2006. **69**(11): p. 2070-2077.

105. Agarwal, R., *Ambulatory GFR measurement with cold iothalamate in adults with chronic kidney disease.* Am J Kidney Dis, 2003. **41**(4): p. 752-759.

106. Dowling, T.C., et al., *Comparison of iothalamate clearance methods for measuring GFR.* Pharmacotherapy, 1999. **19**(8): p. 943-950.

107. Schock-Kusch, D., et al., *Transcutaneous measurement of glomerular filtration rate using FITC-sinistrin in rats.* Nephrol Dial Transplant, 2009. **24**(10): p. 2997-3001.

108. Schock-Kusch, D., et al., *Transcutaneous assessment of renal function in conscious rats with a device for measuring FITC-sinistrin disappearance curves.* Kidney Int, 2011. **79**(11): p. 1254-1258.

109. Yu, W., Sandoval, R.M., and Molitoris, B.A., *Rapid determination of renal filtration function using an optical ratiometric imaging approach.* Am J Physiol Renal Physiol, 2007. **292**(6): p. F1873-1880.

110. Qi, Z., et al., *Serial determination of glomerular filtration rate in conscious mice using FITC-inulin clearance.* Am J Physiol Renal Physiol, 2004. **286**(3): p. F590-F596.

Chapter 2

2 A Truncated RHAMM Protein for Discovering Novel Peptide Therapeutics

2.1 Introduction

The receptor for hyaluronan mediated motility (RHAMM, gene name HMMR) is one of several proteins that bind to the polysaccharide hyaluronan (HA). HA is a high molecular weight (HMW) anionic polysaccharide that is a major component of the extracellular matrix in most tissues and is important to both tissue homeostasis and response to injury processes. Thus, it regulates immune cell infiltration, and such cell behavior as migration, proliferation, and adhesion [1-9]. These functional effects of HA depend upon its molecular weight. For example, native HMW HA (>500 kDa) reduces inflammation and angiogenesis while fragmented HA (<200 kDa) has pro-angiogenic, -inflammatory and -fibrosis properties. Notably, fragmented HA accumulation is linked to the progression of inflammation and fibrosis-based pathologies such as arthritis, diabetes, and idiopathic pulmonary fibrosis [3, 4, 10, 11].

Full-length human RHAMM is an 85 kDa coiled-coil protein in humans (95 kDa in mice) that occurs both in intracellular and extracellular compartments. It has highly restricted and tightly regulated expression in most normal tissues [12], but is one of a number of oncogenic proteins that are exported to the cell surface in response to tissue stress by unconventional transport mechanisms. Cell surface RHAMM regulates both cell motility and mesenchymal differentiation, while intracellular RHAMM is a microtubule-associated protein (MAP) that binds to ERK1,2 [13] and also mediates interactions of TPX2 with Aurora A kinase, which affects microtubule assembly [14]. Intracellular RHAMM localizes to interphase microtubules, the mitotic spindle and centrosomes, and contributes to mitotic spindle integrity and orientation during mitosis [13-18]. These RHAMM functions are required for mobilizing progenitor/stem cells and innate immune cells during development [19] and normal tissue repair [20-23]. De-regulated RHAMM expression has been linked to both centrosomal abnormalities and aberrant cell motility, which likely contribute to the genetic instability and invasion that fuels progression of many cancers. Elevated RHAMM expression is common in cancer, and is prognostic of poor outcome, such as in oral squamous cell, breast and prostate carcinomas [24-26]. The ability of fragmented HA to bind to RHAMM is key to its signaling functions. RHAMM binds to HA fragments and interacts with CD44 and growth factor receptors such as platelet-derived growth factor receptor (PDGFR), epidermal growth factor receptor (EGFR) and members of the hepatocyte growth factor receptor (HGFR) family [13, 27-32]. These interactions activate signaling pathways such as the RAS/MEK1,2/ERK1/,2 cascade and promote AP1/TRE and NFκB transcriptional activity [3, 13, 27, 33] resulting in the expression of genes that promote cell growth and differentiation, tissue remodeling [34-36], tissue morphogenesis [34, 37], matrix organization, inflammation and angiogenesis, and cell trafficking [27, 38-41]. Thus, the specific inhibition of HA-RHAMM interaction could have significant therapeutic potential for preventing activation of HA-mediated signaling cascades.

RHAMM was originally isolated from the supernatants of chick embryonic heart fibroblasts in culture as a 60 kDa isoform [42], and was subsequently cloned from mesenchymal cells [43, 44]. Production and isolation of full-length RHAMM using recombinant protein technology has proven difficult with low isolation yields. We propose the chemical synthesis of a truncated version of the protein (706-767), 7 kDa RHAMM, which contains the HA-binding region [45, 46], for use as the target receptor in the screening of new RHAMM-binding peptides for the development of peptide-based therapeutic agents for treating RHAMM-related disease.

2.2 Results and Discussion

2.2.1 Synthesis and purification of 7 kDa RHAMM

The therapeutic potential of RHAMM-binding peptides that inhibit cellular RHAMM-HA interaction deserves investigation. RHAMM expression is tightly regulated and restricted in healthy homeostatic tissues, but is overexpressed during cellular stress, including tissue repair, chronic inflammation, and oncogenic processes. This makes RHAMM protein an ideal candidate for therapeutic intervention. Synthesis of full-length RHAMM by recombinant protein production methods has been described previously using glutathione-S-transferase (GST) recombinant fusion protein [47, 48], but elution of GST-RHAMM from a glutathione column and the subsequent removal of the GST tag with thrombin results in a final yield of 0.06-0.13% (2-4 mg final yield following 3 g starting material in the supernatant) for recombinant RHAMM protein that is the C-terminal 10 kDa fragment, with much lower yields for larger fragment sizes. The largest loss occurs during the column elution step, and the treatment of the column with SDS to facilitate protein elution compromises bioactivity. Thus, the biosynthesis of recombinant RHAMM protein is difficult, resulting in very low yields. This has therefore directly hindered the discovery and development of therapeutic agents that target RHAMM. Here, we proposed and investigated the chemical synthesis of a truncated receptor that contains both HA binding sites, affording it the HA binding properties that have been well characterized of the native protein, and that can be readily synthesized by Fmoc-based peptide chemistry in high purity. 7 kDa RHAMM (mRHAMM 706-767) is a 62-amino acid mini-protein that bears the same amino acid sequence as that portion of the full-length protein, including the two HA binding domains.

The RHAMM protein is predicted to be predominantly helical and binds to HA by carboxyl-terminal positively charged amino acid clusters [49, 50] in contrast to CD44, which binds to HA in a conformationally-dependent manner to a much larger link module sequence [51]. We reasoned that synthesis of the carboxyl terminal RHAMM sequence should retain its HA binding potential and provide much better yields than achieved recombinantly. We therefore synthesized the aa706-767 fragment of mRHAMM, which contains the HA binding sequence (**Figure 2.1**).

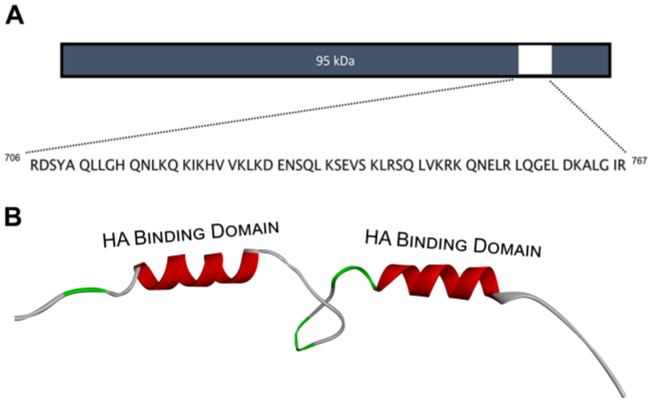

Figure 2.1. 7 kDa RHAMM protein. (A) mRHAMM (706-767) sequence (B) Depiction of 7 kDa RHAMM, showing the protein's two hyaluronan binding domains contained within two helices, as proposed by [50, 51].

7 kDa RHAMM was synthesized by automated Fmoc solid phase peptide synthesis, using Rink amide MBHA resin (0.39 mmol/g loading) and Fmoc-protected L-amino acids. Synthesis of 7 kDa RHAMM was carried out under microwave irradiation conditions, with coupling reactions taking place at 75 °C, with the exception of His residues, which were done at room temperature in order to prevent racemization [52]. Synthesis was performed on a 0.05 mmol scale, as initial attempts indicated that a 0.1 mmol scale did not allow for adequate mixing of the resin during periods of vortexing. Purification by automated HPLC resulted in a final product with a purity >95%. All expected charged states until the $[M+13H]^{13+}$ signals were observed, and the observed isotope pattern for each charged state was as expected (**Table S2.1**).

A negative control mini-protein was synthesized under the same conditions as 7 kDa RHAMM. All basic residues were replaced with alanine residues in both HA binding domains, and we have therefore termed this control Ala-7 kDa RHAMM. Purification by HPLC-MS resulted in a final product with a purity of >95%, and charged states were observed until the $[M+8H]^{8+}$ signals were observed. Characterization of 7 kDa RHAMM

RHAMM's protein sequence is predicted to be largely hydrophilic and alpha helical, with the HA binding domains contained in two tightly coiled coils that are separated by a central loop [50, 53]. The alpha helical structure of the HA binding domains results in the alignment of the positively charged residues on the same face of the helix, where they presumably interact with the negatively charged carboxylate ions of HA [50].

2.2.2 Characterization of 7 kDa RHAMM

The RHAMM protein sequence is predicted to be largely hydrophilic alpha helical, with the HA binding domains contained in two tightly coiled coils that are separated by a central loop [50, 53]. The alpha helical structure of the HA binding domains facilitates ligand binding by ensuring the alignment of the positively charged residues on the same face of the helix, where they presumably interact with the negatively charged carboxylate ions of HA [49, 50]. The portion of the full protein that makes up the mini-protein specifically has been reported to contain helices [50], and therefore, 7 kDa RHAMM is expected to have a similar secondary structure as that portion of full-length RHAMM. Structural analysis of 7 kDa RHAMM by CD spectroscopy confirmed that the mini-protein has an alpha-helical character (**Figure 2.2**). The ratio of the molar ellipticities at the two minima defining helicity in a CD spectrum, $[\theta]222/[\theta]208$, is indicative of the relative helicity of a compound; a compound is more helical when the ratio of these two values approaches 1.0. 7 kDa was found to have a $[\theta]222/[\theta]208$ value of 0.86 in a water solution. For this reason, despite truncation, the secondary structure of 7 kDa RHAMM suggests that this part of the protein might have important secondary structure properties needed for interaction with the protein's native ligand, HA.

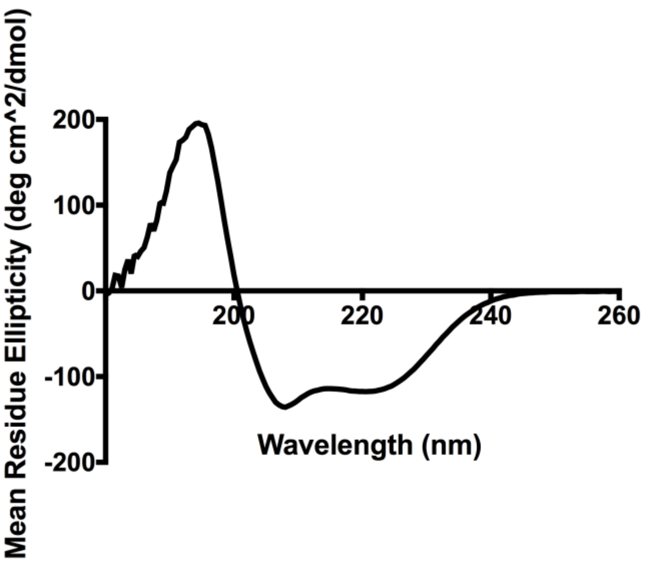

Figure 2.2. 7 kDa RHAMM is helical by CD spectroscopy. CD spectrum of 7 kDa RHAMM in water (0.5 mg/mL) showing alpha-helical character, similar to that of the full-length protein's predicted secondary structure [49, 50].

2.2.3 HA-binding

SPR was used to evaluate the mini-protein-carbohydrate interaction. 5-10 kDa HA was immobilized on the SPR sensor chip surface by a gold-thiol bond. A concentration dependent dose response was observed for the interaction between 7 kDa RHAMM and HA, and in each case, a rapid rate of association, and a stable SPR signal were observed, suggesting a strong interaction between the two compounds (**Figure 2.3A**). Indeed, 7 kDa RHAMM was determined to bind to HA with an average dissociation constant, K_D value, of 9.0 nM ± 0.2 nM. The dissociation constant between RHAMM protein and HA was originally determined to be approximately 10^{-8} M [44], but no reports have confirmed the accuracy of this affinity range until now. Reports on the increase in RHAMM expression in response to HA fragments ranging from 6 kDa HA to 100 kDa HA [11], and the realization that HA fragments that range from 3 to 25 disaccharide units (1.2-10 kDa) have inflammatory and pro-angiogenic properties *in vitro* [54] make the observed binding between 7 kDa RHAMM and 5-10 kDa HA comparable to the cellular receptor. We developed a negative control mini-protein, in which all of the basic residues in both HA binding domains were replaced with alanine, thereby eliminating the characteristic BX_7B binding motif of the HA binding domains, and theoretically preventing the majority of HA binding through ionic interactions. This was indeed found to be the result, yielding a dissociation constant of 3.2 μM ± 0.6 μM, which is almost a 400X weakening of the affinity compared with when the natural sequence is used in the same size protein. In addition, the SPR signal resulting from the interaction between HA and Ala-7 kDa RHAMM had a significantly lower signal to noise ratio than its 7 kDa RHAMM counterpart, as well as a slower association and quicker dissociation, suggesting a weak and less specific interaction. The residual binding that is observed, however, is possibly the result of interactions that are not the predominant ionic interactions of the two molecules, and may include other interactive forces that are common among glycosaminoglycans and the receptors that bind them, such as van der Waals forces, hydrogen bonds and hydrophobic interactions with the carbohydrate backbone [7]. This stark difference in binding affinity between 7 kDa RHAMM and its alanine counterpart highlights the importance of the basic charges to the RHAMM-HA interaction, and that SPR can be used a successful tool in measuring interactions with the mini-protein.

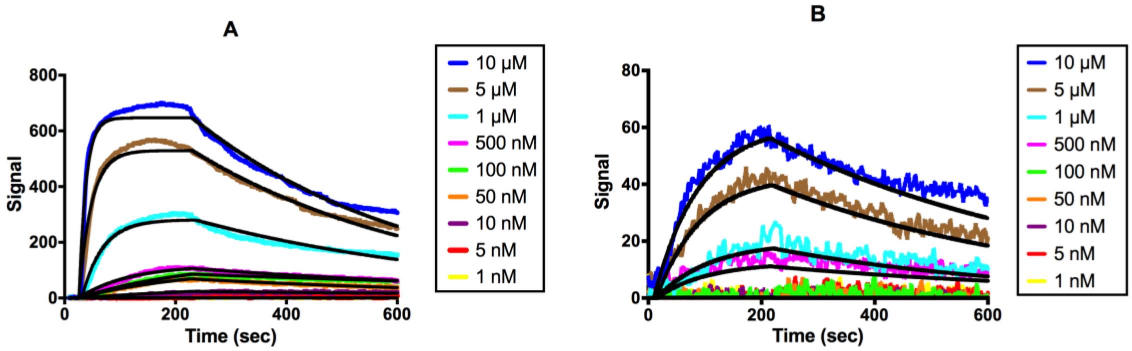

Figure 2.3. 7 kDa RHAMM binds HA by SPR. SPR signals showing the interactions between immobilized 5-10 kDa HA and 7 kDa RHAMM (A) and a negative control mini-protein, which had no basic residues in the HA binding domains (B). Each signal corresponds to the responses of different HA concentrations, and solid lines indicate a linear 1:1 interaction curve fitting model for the ligand-analyte interaction. The dissociation constant was determined to be 9.0 nM for 7 kDa RHAMM and 3.2 μM for the negative control mini-protein.

To confirm the interaction between HA and 7 kDa RHAMM, an enzyme linked immunosorbent assay was carried out using biotinylated 7 kDa RHAMM on HA-coated plates with an average polymer size of 1500-1800 kDa (Echelon). Binding between the mini-protein and HA was found to vary with concentration, resulting in an effective concentration (EC_{50}) value of 0.30 ± 0.05 μM (**Figure 2.4**). This value differs from that obtained by SPR, and can be explained by two major reasons: the difference in size of HA used in the two techniques and the fact that in SPR, substrates are not fixed to the surface of the biosensor, while in ELISA, HA is fixed to the plate, potentially resulting in a different orientation of the carbohydrate, and specifically its carboxylate ions, than in SPR. Nevertheless, the strong and highly specific interaction between 7 kDa RHAMM and HA suggests that truncating the receptor to the 62-amino acids length of mini-protein does not negatively impact HA binding, and therefore, 7 kDa RHAMM can be used as a receptor in developing novel peptide-based ligands that compete with HA for RHAMM-binding.

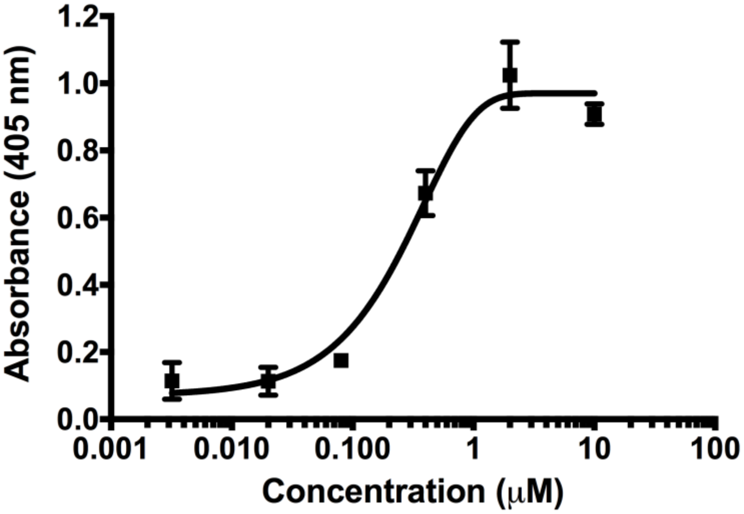

Figure 2.4. 7 kDa RHAMM binds HA by ELISA. ELISA was performed with HA-coated plates and varying concentrations of biotinylated 7 kDa RHAMM.

2.2.4 Optimization of synthesis

Synthesis of long peptides or short proteins by Fmoc chemistry requires additional synthetic tools beyond those available through standard Fmoc-based solid-phased peptide synthesis. Specifically, aggregation during chain assembly and inter- and intra-chain interactions can be minimized by special solvents, such as complex solvent mixtures [55], chaotropic salts[55, 56], structure disrupters such as Pro residues, 2-hydroxy-4-methoxybenyl (Hmb) peptide backbone protection [57, 58], and by resins that facilitate the solvation of peptide chains. Here, we investigate the optimization of 7 kDa RHAMM by applying pseudoproline dipeptides within its sequence during synthesis, as it has been advocated as being the most promising method of facilitating the synthesis of long sequences that are at risk of aggregation [59, 60]. In pseudoproline dipeptides, Ser, Thr, or Cys residues are reversibly protected as proline-like oxazolidines [60]. As with proline, the pseudoproline dipeptides induce kinks in the backbone of the growing polymer chain, thereby removing hydrogen bond donors and disrupting aggregation during chain elongation. Following completion of synthesis of the peptide, cleavage with TFA opens the oxazolidine ring, generating the natural amino acid sequence.

While the strategy of using 5-minute microwave irradiation coupling steps in standard Fmoc-based solid-phase peptide synthesis generated a 62mer mini-protein with high purity following purification (>95%), the final preparative yield was only a few mg in total on a 0.05 mmol scale (3%). We therefore tried optimizing the synthesis of the mini-protein by employing pseudoproline dipeptides at various positions within its sequence. 7 kDa RHAMM has 5 Ser resides, 4 of which have commercially available dipeptides available for replacement: S^{750}, S^{747}, S^{743}, and S^{708}. We evaluated the replacement of the natural amino acids at each of these sites, and compared their yield and purity with the normal synthetic strategy of using all L-amino acids (**Table 2.1**) under identical synthesis, cleavage and purification conditions.

Table 2.1. Summary of 7 kDa RHAMM synthesis and purification by SPPS using natural amino acids and pseudoproline dipeptide on rink amide resin

	Pseudoproline substitution	Purity	Preparative Yield
1	None (all L amino acids, natural sequence)	>95%	3%
2	$D^{707}S^{708}$ $N^{742}S^{743}$	>95%	4%
3	$D^{707}S^{708}$ $N^{742}S^{743}$ $K^{746}S^{747}$	>95%	10%
4	$D^{707}S^{708}$ $N^{742}S^{743}$ $V^{749}S^{750}$	>95%	12%
5	$D^{707}S^{708}$ $N^{742}S^{743}$ $K^{746}S^{747}$ $V^{749}S^{750}$	>95%	10%

Using pseudoproline dipeptides as replacements of two individual amino acids at each of the positions optimized the synthesis yield for 7 kDa RHAMM from 3% to 12% without sacrificing purity. The greatest improvement in yield resulted when the amino acids were replaced at S^{743} and S^{750}, which lie in the middle of the amino acid sequence and where aggregation begins to occur. This finding correlates with published protocols, which suggest that the effect of pseudoproline dipeptides are realized 6-10 residues after their incorporation [61, 62]. Interestingly, the replacement of S^{750}, S^{747}, and S^{743} was less efficient when compared to the synthesis in which replacement of only S^{743} and S^{750} was done, suggesting that introducing pseudoproline residues at close proximity, and below the 6-10 residue optimal spacing, negatively influences yield. In this case, a higher than optimal number of kinks could be introduced in the polymer backbone. Despite the modest improvement in yield resulting from using the pseudoproline dipeptides, we concluded that use of natural amino acids is still more prudent for our needs due to the cost constraints associated with the purchase of commercially available pseudoproline dipeptides.

2.2.5 *In culture* functional assay

It has been previously shown that RHAMM regulates cellular functions associated with motility and affects signaling cascades in mesenchymal cells [26, 27, 63, 64]. RHAMM blocking antibodies, RHAMM mimetic peptides, and genetic deletion of RHAMM reduce migration of mesenchymal and other cell types [3, 22, 27, 65-69]. To investigate whether 7 kDa RHAMM competes with native cell-surface RHAMM on mesenchymal cells, we quantified scratch wound induced migration of RHAMM-transfected 10T1/2 cells with and without 7 kDa RHAMM. As shown by fluorescent staining, RHAMM is located in cell processes on the cell surface where it can interact with HA while intracellular RHAMM is diffused in the cytoplasm (**Figure S2.10**). 7 kDa RHAMM inhibited migration of these cells in scratch wound assays, suggesting that it successfully competes with the endogenous HA receptor for HA binding. (**Figure 2.5**).

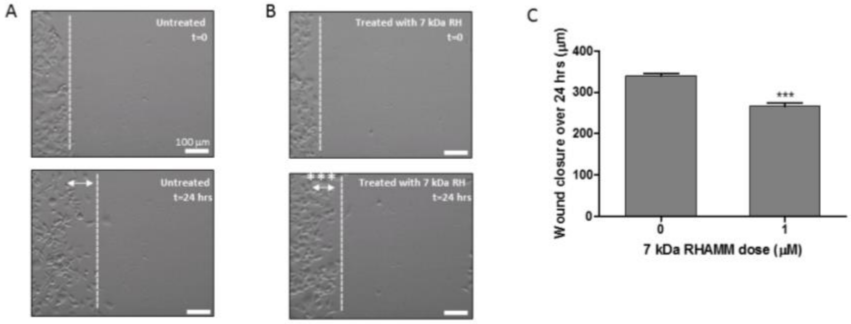

Figure 2.5. Excisional scratch wound assay performed on RHAMM-transfected 10T1/2 cells (LR21). LR21 cells treated with 7 kDa RHAMM (B) migrate slower over 24 hours than those not treated with the synthetic receptor (A). Statistical significance determined by students t-test (*p<0.005). Scale bar, 100 µM.**

We have demonstrated that RHAMM binds to HA more tightly than it has been previously reported to bind to other HA receptors, such as CD44 [70, 71], LYVE-1 [72-74]. Interestingly, CD44, which is the major HA-binding receptor expressed on most cell types [11], appears to require simultaneous clustering with other HA receptor molecules, including RHAMM, in a multivalent fashion in order to stably bind the polysaccharide [75]. In addition, the activation of ERK1,2 and cellular motility in culture depend directly on the function of RHAMM in the presence of HA [27]. In fact, it has been shown that RHAMM expression increases in response to an increase in the expression of all sizes of fragmented HA [11], predicting that the development of RHAMM-targeted peptides that bind and block RHAMM signaling will be useful in blunting many disease processes.

RHAMM regulates cellular functions associated with motility and cellular migration after injury [27]. The RHAMM mini-protein binds HA and was therefore predicted to act as an HA fragment sink, inhibiting the normal function of RHAMM. Indeed, this was found to be the case when RHAMM-overexpressing mesenchymal cells were treated with 7 kDa RHAMM. LR21 cells are transfected with RHAMM$^{\Delta163}$ (73 kDa) [76], which differs from full length RHAMM (RHAMM^{FL}, 85 kDa) in its cellular localization; while both isoforms of the protein are expressed both intracellularly and at the cell surface, full length RHAMM localizes primarily to the cytoskeleton and RHAMM$^{\Delta163}$ has been suggested to be found primarily in the nucleus, on the cell membrane [77] and at podosomes, which are specialized structures of cell substratum contact and matrix metalloproteinase (MMP) release (**Figure S2.10**), and therefore, contribute to the migration. Biotinylated 7 kDa RHAMM was shown by confocal microscopy to be endocytosed in vesicles by LR21 cells following incubation, with vesicle accumulation in the perinuclear region (**Figure 2.6**) as is typical of most endocytosed cell surface receptors. This is the first report of cells behaving in this manner following treatment with a RHAMM protein. Treatment of cells with 7 kDa RHAMM protein, despite truncation to 7 kDa in size, inhibits the natural function of the endogenous cell surface protein, where it potentially binds endogenous HA receptors or growth factor receptors that are present at the cell surface, blocking RHAMM-dependent motile behavior.

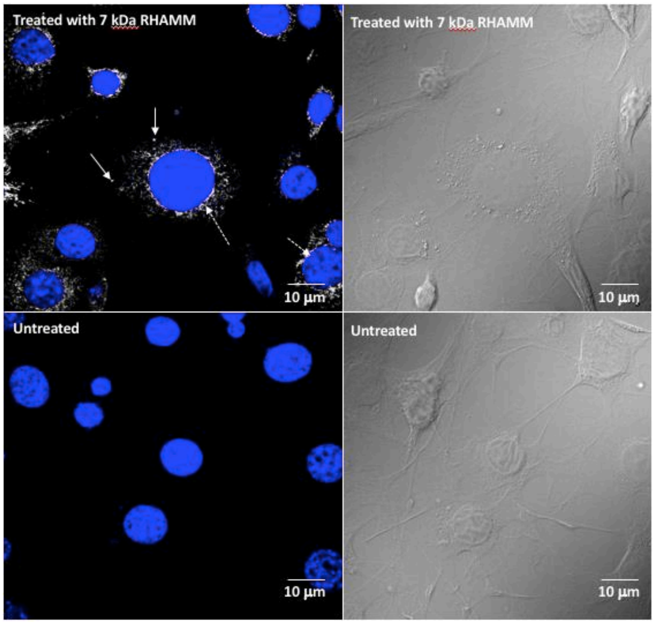

Figure 2.6. Biotinylated 7kDa RHAMM binds to the cell surface and occurs in intracellular perinuclear vesicles. The 7kDa RHAMM mini-protein was added to cultured RHAMM-transfected 10T1/2 fibroblasts, and its distribution was detected using a fluorescent streptavidin. Results show that extracellular staining can be detected (solid white arrows) and in intracellular, perinuclear vesicles (dotted white arrows). Results show that 7 kDa RHAMM is detected near or at the cell surface and that the majority of staining occurs in perinuclear vesicles, which is consistent with its endocytic uptake. Blue is Dapi to detect nuclei, and brightfield images are included to show intact cells.

2.2.6 Protein-ligand binding studies

We have previously reported the discovery and screening of tubulin-derived peptides that compete with HA for RHAMM binding by SPR [78]. However, the difficult purification and isolation of the full-length RHAMM protein renders direct protein-ligand interaction studies difficult to undertake, and may have hindered the discovery of novel molecules since. Here, we investigated the interaction between 7 kDa RHAMM and tubulin-derived peptides by SPR in order to compare chemically synthesized truncated RHAMM with our previous results using recombinant RHAMM protein.

7 kDa RHAMM was functionalized with a histidine tag on its carboxyl terminus during synthesis for immobilization on a nitrilotriacetic acid (NTA) biosensor surface without disrupting the mini-protein's secondary structure or hindering the HA binding sites. Previously reported tubulin-derived peptides were observed to bind the immobilized mini-protein (**Figure 2.7**) with affinities that are highly comparable to those of the recombinant protein (**Table 2.2**), suggesting that truncating the receptor has little effect on binding potential of RHAMM-binding peptides. Compounds that did not bind the recombinant protein also showed no binding to the synthesized RHAMM mini-protein, such as in the case of compound 7a (**Figure 2.7**). Therefore, the chemically synthesized receptor appears to be an appropriate replacement receptor for the recombinant protein in screening novel peptide ligands that bind to the HA binding region of RHAMM. Interestingly, RHAMM sequence aa706-767 has also been shown to bind to tubulin, kinases, such as ERK1 [13], and kinase regulators, such as TPX2 [14], suggesting that this mini-protein will also be useful to screen for peptides that block intracellular signaling as well as interactions/functions involving microtubules, mitotic spindles and centrosomes. Successful synthesis of the RHAMM mini-protein permits discovery and screening for novel RHAMM-binding therapeutic agents, as well as optimizing and evaluating current HA and RHAMM mimic peptides and other therapeutic agents. Importantly, this will facilitate the identification of novel drug compounds that block extra- and intra-cellular RHAMM functions that play important roles in disease progression.

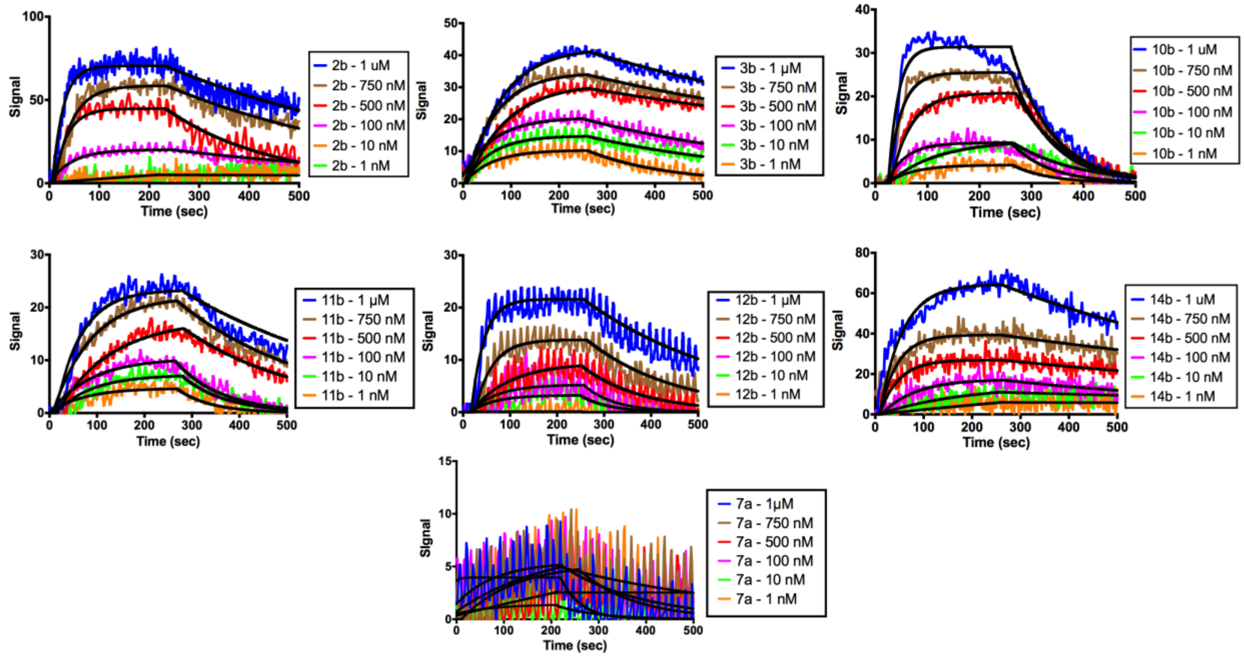

Figure 2.7. SPR signals showing the interaction between immobilized 7 kDa RHAMM and previously reported tubulin-derived peptides, both binding and non-binding. Negative control (no peptide) graphs are also shown. Each signal corresponds to the responses of six peptide concentrations (1000 nM, 750 nM, 500 nM, 100 nM, 10 nM, and 1 nM). The solid lines indicate a global 1:1 interaction curve fitting model for each of the interactions.

Table 2.2. Binding affinities of tubulin-derived peptide analogues for 7 kDa RHAMM and recombinant RHAMM

Peptide ID [78]	**Conc. (nM)**	**k_a (10^4/(M*s))**	**k_d (10^3/s)**	**K_D (nM)**	**Avg. K_D (nM)**	**Avg. K_D with recomb. RHAMM [78] (nM)**
2b	1000	4.1 ± 0.1	1.6 ± 0.1	39.7 ± 0.1	43.3 ± 3.7	24.2 ± 0.4
	750	5.0 ± 0.1	8.1 ± 0.1	61.5 ± 4.7		
	500	5.8 ± 0.2	1.4 ± 0.2	72.4 ± 2.3		

	100	0.2 ± 0.04	4.3 ± 0.1	8.8 ± 0.1		
	10	1.6 ± 0.1	1.22 ± 0.02	77.4 ± 14.8		
	1	0.7 ± 0.1	4.5 ± 0.1	2.40 ± 0.01		
3b	1000	1.3 ± 0.1	1.08 ± 0.03	84.3 ± 2.2	31.9 ± 1.2	331.1± 24.5
	750	1.9 ± 0.2	1.03 ± 0.03	54.6 ± 3.3		
	500	2.3 ± 0.4	0.08 ± 0.02	36.5 ± 1.4		
	100	1.4 ± 0.1	1.9 ± 0.1	14.3 ± 0.3		
	10	0.16 ± 0.02	2.4 ± 0.2	1.5 ± 0.2		
	1	0.02 ± 0.03	5.9 ± 0.2	0.5 ± 0.1		
10b	1000	4.0 ± 0.2	1.3 ± 0.1	314.2 ± 12.2	201.8 ± 8.0	32.6 ± 1.1
	750	3.3 ± 0.1	1.3 ± 0.1	392.1 ± 10.3		
	500	3.0 ± 0.2	1.1 ± 0.1	366.3 ± 12.3		
	100	1.4 ± 0.3	1.4 ± 0.2	99.3 ± 12.0		
	10	2.3 ± 0.2	8.2 ± 0.3	36.3 ± 1.3		
	1	5.7 ± 0.1	1.5 ± 0.2	2.6 ± 0.2		
11b	1000	1.6 ± 0.2	2.3 ± 0.3	144.1 ± 15.8	265.1 ± 4.9	130.0 ± 12.9
	750	1.2 ± 0.1	3.5 ± 0.5	295.2 ± 1.7		
	500	1.0 ± 0.1	3.9 ± 0.3	379.3 ± 5.8		
	100	1.5 ± 0.1	0.1 ± 0.2	694.4 ± 5.1		
	10	0.22 ± 0.02	0.1 ± 0.2	49.3 ± 0.4		
	1	0.48 ± 0.03	0.1 ± 0.2	29.4 ± 0.5		
12b	1000	3.4 ± 0.4	3.1 ± 0.4	90.9 ± 1.6	289.2 ± 2.2	211.3 ± 8.6
	750	2.9 ± 0.2	5.2 ± 0.5	180.2 ± 3.3		
	500	0.9 ± 0.1	7.7 ± 0.6	90.9 ± 3.7		
	100	3.1 ± 0.2	0.8 ± 0.2	476.6 ± 2.2		

	10	3.1 ± 0.1	0.4 ± 0.1	52.3 ± 1.0		
	1	3.7 ± 0.12	5.2 ± 0.2	27.0 ± 1.0		
14b	1000	2.0 ± 0.3	1.4 ± 0.2	70.7 ± 11.7	20.9 ± 5.9	30.2 ± 1.5
	750	3.5 ± 0.4	8.5 ± 0.6	23.9 ± 11.1		
	500	4.9 ± 0.2	8.9 ± 0.7	18.1 ± 7.3		
	100	0.1 ± 0.1	1.5 ± 0.2	11.3 ± 2.3		
	10	0.5 ± 0.1	6.2 ± 0.3	1.2 ± 3.1		
	1	0.8 ± 0.1	1.2 ± 0.2	0.1 ± 0.1		

2.3 Conclusion

The present study demonstrated that chemically synthesized truncated RHAMM can be used as a surrogate for the binding site for screening novel peptide ligands. 7 kDa RHAMM has the same predicted secondary structure as the native protein [49, 50], facilitating binding to the native ligand, HA, and is biologically active in fibroblast cells. Chemical modifications, such as the addition of a histidine tag and a biotin molecule, can be easily incorporated during synthesis of 7 kDa RHAMM, and purification of the chemically synthesized mini-protein produces a final compound with higher yield and purity than is possible for the recombinant protein. In addition, 7 kDa RHAMM binds previously reported tubulin-derived peptides with similar affinities as recombinant RHAMM. The high degree of similarity in binding kinetics between the tubulin-derived peptides and recombinant RHAMM and the peptides and chemically-synthesized RHAMM is suggestive of a strong similarity in the binding action of the two proteins. Therefore, 7 kDa RHAMM may have potential applications in further characterizing the nature and functions of the interactions of RHAMM with HA and other ligands, which are currently lacking in the literature. For these reasons, 7 kDa RHAMM is an efficient and effective replacement receptor protein for screening and discovering novel RHAMM-binding ligands, and will allow for the specific inhibition of RHAMM-ligand interactions, and treatment of RHAMM-associated diseases.

2.4 Experimental

2.4.1 General Methods

All peptides, 7 kDa RHAMM, and modified versions of the mini-protein containing pseudoproline dipeptides and a C-terminal histidine tag, were synthesized on an automated synthesizer (Syrowave, Biotage) applying fluorenyl-9-methoxycarbonyl (Fmoc) solid phase peptide synthesis. All coupling reactions were carried out under microwave conditions at 75 °C for 5 minutes with vortexing, with the exception of histidine residues, which were double coupled for 90-minute and 30-minute intervals at room temperature. Cleavage of the peptides was carried out by treating the resin with TFA: water: triisopropylsilane (95:2.5:2.5 v/v) for 5 hours. The cleaved peptides were then precipitated with cold TBME, and were pelleted by centrifugation at 1000 Gs for 10 min. After decanting the supernatant, the pellets were rinsed with tert-butyl methyl ether (TBME), re-suspended by vortexing, and centrifuged again. The ensuing products were dissolved in water, frozen and lyophilized until a dry, solid powder was obtained.

Analysis of the peptides was carried out using a reversed-phase analytical HPLC column (Agilent Zorbax SB-C18 column 4.6 x 150 mm, 3.5 μm). This system was outfitted with a Waters 600 136 controller, Waters Prep degasser, and Waters MassLynx software (version 4.1). The mobile phases employed were 0.1% TFA in water (solvent A) and 0.1% TFA in acetonitrile (solvent B) with a flow rate of 1.5 mL/min over 15 minutes. The absorbance was monitored using a Waters 2998 Photodiode array detector set at 220 nm, 254 nm, and 400 nm. All peptides and 7 kDa RHAMM were purified using a reversed-phase preparative HPLC column (Agilent Zorbax SB-C18 column 21.2 x 150 mm, 5 μm) all system specifics were the same as those used for the analytical system. The flow rate for the preparative HPLC was set at 20 mL/min, with the absorbance being monitored under the same conditions as previously described. The collected fractions were then lyophilized to a solid, and subsequently analyzed by analytical RP-HPLC (220 nm) and ESI-MS on a Acquity UHPLC-MS system (Waters Co.).

2.4.2 Synthesis and purification of 7 kDa RHAMM

Synthesis was conducted on a 0.05 mmol scale using Rink amide MBHA (0.39 mmol/g), with a four-fold excess of Fmoc protected L-amino acids. Amino acids were coupled with HCTU (4 eq.) in DMF and DIPEA (6 eq.). All couplings from Ser^{30} onwards were double coupled. Fmoc was removed using 2 treatments of 20% piperidine/DMF for 15-minute and 5-minute periods. Following synthesis, the resin was washed with dichloromethane. Purification of 7 kDa RHAMM was carried out as described above at a gradient of 25 to 45%.

2.4.3 Circular Dichroism spectroscopy

CD was carried out on a Jasco J-810 spectropolarimeter and recorded in the range of 180-260 nm. 7 kDa RHAMM (>95% purity, lyophilized) was dissolved in Milli-Q water to a concentration of 0.5 mg/mL. The measurement was carried out at 20 ^{O}C, using a quartz cuvette with a path length of 1 mm. The instrument measured at a scanning speed of 10-50 nm/min, and averaged five individual data points in order to obtain the reported CD spectrum. A blank solution of Milli-Q water, and 40% TFE/water were run before the measurements, and the spectra were baseline corrected.

2.4.4 Evaluation of HA-binding

2.4.4.1 SPR

5-10kDa HA (purchased as sodium hyaluronate, Research Grade 5K, Lifecore Biomedical) was dissolved in DMSO/H_2O (7/3, v/v), and was reacted with excess sodium cyanoborohydride for 12 hours at room temperature. 10 equivalents of cysteamine hydrochloride (Sigma Aldrich) was added, and the reaction proceeded for an additional 24 hours. The solution was then dialyzed exhaustively in deionized water for 3 days using a 3.5-5 kDa dialysis tube (Float-a-Lyzer, Spectrum Labs) with a biotech grade cellulose ester membrane.

All experiments were carried out on an OpenSPR^{TM} instrument (Nicoya Lifesciences) at 25°C, equipped with a 100 μL loading loop. 100 nm gold nanoparticle biosensors were purchased from Nicoya Lifesciences. All experiments were carried out in phosphate buffered saline (PBS) running buffer (137 mM NaCl, 2.7 mM KCl, 10 mM Na_2HPO_4, 2 mM KH_2PO_4), pH 7.4. The gold biosensors were incubated with cystamine-functionalized 5-10 kDa HA (3mg/mL) for 3 days. Available binding sites on the chip surface were blocked with poly(ethylene glycol) methyl ether thiol (2 mg/mL) (Sigma Aldrich). 7 kDa RHAMM and Ala-7 kDa RHAMM were dissolved in PBS at varying concentrations, and were injected at a flow rate of 25 μL/min when the baseline was stabilized. Regeneration of the chip surface was carried out with 1M NaCl, and no further injections were done until the baseline was stable. The data was processed and analyzed using Tracedrawer software (Ridgeview Instruments AB). Kinetic parameters were calculated using a local analysis, fitting the data to a 1:1 model.

2.4.4.2 ELISA

Biotinylated 7 kDa RHAMM was synthesized under the same conditions as before, but was N-terminally modified to include biotin as the free acid (Sigma Aldrich), separated by a PEG-2 linker from the remainder of the mini-protein strand. Fmoc-AEEA-OH (PEG-2) (3 eq.) was coupled onto the N-terminus of the peptide at room temperature for 1 hour with activation by HCTU (3 eq.) and DIPEA (6 eq.). Following Fmoc deprotection with two cycles (5 minutes and 15 minutes) of 20% piperidine in DMF, Biotin-OH (3 eq.) was added with HATU (3 eq.) and DIPEA (6 eq.), which proceeded overnight. Cleavage of the truncated protein from the resin was carried out as described above. 7 kDa RHAMM was purified by the same method as before, with a solvent gradient of 30 to 45%.

An ELISA was utilized to measure HA-binding. Five milligrams of biotin-labeled mini-protein was dissolved in 1 mL phosphate-buffered saline (PBS). This stock solution was further dissolved in 1X Tris-buffered saline (TBS) to generate peptide solutions of 50 μg/mL, 10 μg /mL, 2 μg /mL, 0.4 μg /mL, 0.08 μg /mL, and 0.016 μg/mL. These were subsequently added to HA coated ELISA plates (200 μL/well, triplicates, Echelon kit K-1200), and were incubated overnight at 40 °C. 200 μL of 1X TBS was used as a negative control. Wells were washed 3 times with 200 μL 1X TBS and then 100 μL pre-diluted streptavidin-HRP (LSAB2 Streptavidin-HRP, DAKO K1016) was added to each well and the ELISA plate was incubated for 1 hour at room temperature. Wells were washed 3 times with 200 µL 1X TBS and 100 µL 3,3',5,5'-tetramethylbenzidine (TMB) solution (Echelon kit K-4800) was added. After a 20-minute incubation at room temperature, 50 µL 1N H_2SO_4 stop solution was added. Absorbance was measured at 450 nm using a SYNERGY H4 (BioTek) plate reader. Data was fitted to a nonlinear regression curve with equation $Y = 0.97 + (0.07 - 0.97)e^{-2.58X}$.

2.4.5 Optimization

All syntheses were carried out as described above, except that Fmoc-Asp(OtBu)-Ser($\psi^{\mathrm{Me,Me}}$pro)-OH, Fmoc-Asn(Trt)-Ser($\psi^{\mathrm{Me,Me}}$pro)-OH, Fmoc-Lys(Boc)-Ser($\psi^{\mathrm{Me,Me}}$pro)-OH, and Fmoc-Val-Ser($\psi^{\mathrm{Me,Me}}$pro)-OH (Novabiochem) were used to introduce $D^{707}S^{708}$, $N^{742}S^{743}$, $K^{746}S^{747}$, and $V^{749}S^{750}$, respectively. All coupling reactions were carried out under the same conditions as their L-amino acid counterparts. Cleavage of the peptides from the resin, and purification were carried out as before.

2.4.6 Confocal Microscopy

LR21 cells were plated on fibronectin coated cover slips. The next day, medium was changed to defined medium (DEMEM, insulin, transferrin) and 10 µM biotinylated 7 kDa RHAMM was added. Defined medium without biotinylated 7 kDa RHAMM was used as negative control. After 24 hrs, cover slips were washed three times with 1X PBS. Cover slips were treated with 0.1 % Triton-x /PBS for 10 min at RT, then washed once with 1X PBS. Cover slips were blocked with 3% BSA/PBS for 1 hour at RT. Blocking buffer was removed and fluorescent streptavidin (Alexa 647), diluted 1:250 in 1% BSA/PBS, was added. After 2 hours at RT, cover slips were washed three times with 1X PBS at RT, then cover slips were mounted with mounting medium containing DAPI (Invitrogen, antifade Gold with DAPI). A confocal microscope (Olympus) was used to obtain fluorescence and DIC images using a 100X objective.

2.4.7 Scratch Wound Assay

LR21 cells were cultured in DMEM low glucose medium containing 10% FBS and antibiotics/antimycotics. For scratch wound assays, sufficient LR21 cells were plated in fibronectin (25 µg/ml PBS) coated ibidi 15µ-slide 8 well chambers to allow formation of a confluent cell monolayer. The next day, cultures were scratch wounded using a blue micro pipettor tip. Cells were washed once with growth medium to remove cell debris. Medium was changed to defined medium (DMEM low glucose, 4 μg/ml insulin, 8 μg/ml transferrin, antibiotics/antimycotics) containing 7 kDa RHAMM (1 μM). 8 well chambers were placed inside an ibidi environmental chamber attached to an ibidi temperature controller and gas mixer. Culture conditions were kept constant at 37 °C, 5% CO_2, humidified atmosphere. Wound closure was filmed for 24 hours using a Nikon Eclipse TE 300 microscope equipped with a 10X objective, Hoffman optic and a Hamamatsu digital camera. Image acquisition occurred every 5 min over 24 hours and was controlled by NIS-Elements AR 3.2 software. Wound closure was quantified by measuring migration distance of the migration front over 24 hours using the NIS-Elements AR 3.2 software.

2.4.8 Statistical Analysis

Statistical analysis was performed using GraphPad Prism® software. Data were expressed as means ± SEM. Statistical analysis was performed using a one-way ANOVA and Tukey's post-hoc test with level of significance indicated as follows: *$p < 0.05$, ** $p < 0.01$ and *** $p < 0.001$

2.4.9 SPR experiments with tubulin-derived peptides

Histidine tagged 7 kDa RHAMM was synthesized by first synthesizing the histidine tag on the C-terminus, comprising of six His residues, which were coupled at room temperature. Following synthesis of the His tag, Fmoc-AEEA-OH (PEG-2) (3 eq.) was coupled, followed by the synthesis of 7 kDa RHAMM, which was synthesized under the same conditions as before. Cleavage of the peptide from the resin was carried out as before. 7 kDa RHAMM was purified by the same methods as described above, with a gradient of 25 to 45%.

All experiments were carried out on an OpenSPR™ instrument (Nicoya Lifesciences). Nitrilotriacetic acid (NTA) biosensors were purchased from Nicoya Lifesciences. All experiments were carried out in PBS buffer. The sensor chip surface was primed with imidazole (200 mM) and $NiCl_2$ (40 mM). 7 kDa RHAMM was immobilized onto the biosensor surface at a flow rate of 25 μL/min using a protein concentration of 0.1 mg/mL in a 100 μL sample loop. The peptide ligands were dissolved in water at 10X, 4X, 2X, and 1.25X concentration dilutions from 1 mM to 100 pM, and were injected at a flow rate of 25 μL/min when the protein signal was stabilized. Regeneration of the chip surface was carried out with 1 M NaCl, and no further injections were done until the baseline was stable. The data was processed and analyzed using Tracedrawer software.

2.4.10 Immunofluorescent staining

10T1/2 cells were purchased from ATCC and transfected with 73 kDa RHAMM and a full-length RHAMM cDNA encoding either Zs-green or non-immune IgG [76]. For immunofluorescent staining, RHAMM-transfected cells were plated on fibronectin-coated coverslips. The confluency of these cultures was less than 50%. Cells were fixed in 4% paraformaldehyde/PBS pH 7.5 for 10 minutes at RT. Fixed cells were washed two times with PBS. Non-specific antibody binding was prevented by incubating cover slips with 3% BSA/PBS for 1 hr. Cover slips were then incubated with either a primary antibody to ZsGreen (CloneTech) or non-immune IgG used as a negative control according to manufacturer's instructions. Cover slips were washed three times with PBS to remove unbound IgG/antibody and were then incubated with Alexa dye-conjugated secondary antibody (Alexa 555 or Alexa 488, Invitrogen), washed and mounted using DAPI containing ProLong Gold antifade mounting reagent (Invitrogen). Cells were imaged using a confocal microscope (Olympus IX81) using FV10-ASW 4.2 software.

2.5 References

1. Burdick, J.A. and Prestwich, G.D., *Hyaluronic acid hydrogels for biomedical applications.* Adv Mater, 2011. **23**(12): p. H41-56.

2. Jiang, D., Liang, L., and Noble, P.W., *Hyaluronan as an immune regulator in human diseases.* Physiol Rev, 2011. **91**(1): p. 221-264.

3. Tolg, C., et al., *A RHAMM mimetic peptide blocks hyaluronan signaling and reduces inflammation and fibrogenesis in excisional skin wounds.* Am J Pathol, 2012. **181**(4): p. 1250-1270.

4. Veiseh, M., et al., *Imaging of Homeostatic, Neoplastic, and Injured Tissues by HA-Based Probes.* Biomacromolecules, 2012. **13**(1): p. 12-22.

5. Stern, R., Asari, A.A., and Sugahara, K.N., *Hyaluronan fragments: an information-rich system.* Eur J Cell Biol, 2006. **85**(8): p. 699-715.

6. Toole, B.P., *Hyaluronan: from extracellular glue to pericellular cue.* Nat Rev Cancer, 2004. **4**(7): p. 528-539.

7. Gandhi, N.S. and Mancera, R.L., *The Structure of Glycosaminoglycans and their Interactions with Proteins.* Chem Biol Drug Des, 2008. **72**(6): p. 455-482.

8. Olczyk, P., et al., *[Hyaluronan: structure, metabolism, functions, and role in wound healing].* Postepy Hig Med Dosw, 2008. **62**: p. 651-659.

9. Misra, S., et al., *Hyaluronan-CD44 interactions as potential targets for cancer therapy.* Febs j, 2011. **278**(9): p. 1429-1443.

10. Veiseh, M., et al., *Cellular heterogeneity profiling by hyaluronan probes reveals an invasive but slow-growing breast tumor subset.* Proc Natl Acad Sci, 2014: p. 201402383.

11. D’Agostino, A., et al., *Is molecular size a discriminating factor in hyaluronan interaction with human cells?* Carbohydr Polym, 2017. **157**: p. 21-30.

12. Maxwell, C.A., McCarthy, J., and Turley, E., *Cell-surface and mitotic-spindle RHAMM: moonlighting or dual oncogenic functions?* J Cell Sci, 2008. **121**(7): p. 925-932.

13. Tolg, C., et al., *RHAMM promotes interphase microtubule instability and mitotic spindle integrity through MEK1/ERK1/2 activity.* J Biol Chem, 2010. **285**(34): p. 26461-26474.

14. Chen, H., et al., *Spatial regulation of Aurora A activity during mitotic spindle assembly requires RHAMM to correctly localize TPX2.* Cell Cycle, 2014. **13**(14): p. 2248-2261.

15. Dunsch, A.K., et al., *Dynein light chain 1 and a spindle-associated adaptor promote dynein asymmetry and spindle orientation.* J Cell Biol, 2012. **198**(6): p. 1039-1054.

16. Connell, M., et al., *HMMR acts in the PLK1-dependent spindle positioning pathway and supports neural development.* Elife, 2017. **6**: p. e28672.

17. Li, H., et al., *Spindle Misorientation of Cerebral and Cerebellar Progenitors Is a Mechanistic Cause of Megalencephaly.* Stem Cell Reports, 2017. **9**(4): p. 1071-1080.

18. Li, H., et al., *RHAMM deficiency disrupts folliculogenesis resulting in female hypofertility.* Biol Open, 2015. **4**(4): p. 562-571.

19. Choudhary, M., et al., *Putative role of hyaluronan and its related genes, HAS2 and RHAMM, in human early preimplantation embryogenesis and embryonic stem cell characterization.* Stem Cells, 2007. **25**(12): p. 3045-3057.

20. Schwertfeger, K.L., et al., *Hyaluronan, Inflammation, and Breast Cancer Progression.* Front Immunol, 2015. **6**: p. 236.

21. Tolg, C., P. Telmer, and Turley, E., *Specific sizes of hyaluronan oligosaccharides stimulate fibroblast migration and excisional wound repair.* PLoS One, 2014. **9**(2): p. e88479.

22. Foley, J.P., et al., *Toll-like receptor 2 (TLR2), transforming growth factor-beta, hyaluronan (HA), and receptor for HA-mediated motility (RHAMM) are required for*

surfactant protein A-stimulated macrophage chemotaxis. J Biol Chem, 2012. **287**(44): p. 37406-37419.

23. Sokolowska, M., et al., *Low molecular weight hyaluronan activates cytosolic phospholipase A2alpha and eicosanoid production in monocytes and macrophages.* J Biol Chem, 2014. **289**(7): p. 4470-4488.

24. Shigeishi, H., et al., *Overexpression of the receptor for hyaluronan-mediated motility, correlates with expression of microtubule-associated protein in human oral squamous cell carcinomas.* Int J Oncol, 2009. **34**(6): p. 1565-1571.

25. Turley, E.A., Wood, D.K., and McCarthy, J.B., *Carcinoma Cell Hyaluronan as a "Portable" Cancerized Prometastatic Microenvironment.* Cancer Res, 2016. **76**(9): p. 2507-2512.

26. Tolg, C., et al., *Hyaluronan and RHAMM in wound repair and the "cancerization" of stromal tissues.* Biomed Res Int, 2014. **2014**: p. 103923-103941.

27. Tolg, C., et al., *Rhamm-/- fibroblasts are defective in CD44-mediated ERK1,2 motogenic signaling, leading to defective skin wound repair.* J Cell Biol, 2006. **175**(6): p. 1017-1028.

28. Katona, E., et al., *PP2B and ERK1/2 regulate hyaluronan synthesis of HT168 and WM35 human melanoma cell lines.* Int J Oncol, 2016. **48**(3): p. 983-997.

29. Jiang, J., Mohan, P., and Maxwell, C.A., *The cytoskeletal protein RHAMM and ERK1/2 activity maintain the pluripotency of murine embryonic stem cells.* PLoS One, 2013. **8**(9): p. e73548.

30. Hatano, H., et al., *Overexpression of receptor for hyaluronan-mediated motility (RHAMM) in MC3T3-E1 cells induces proliferation and differentiation through phosphorylation of ERK1/2.* J Bone Miner Metab, 2012. **30**(3): p. 293-303.

31. Nikitovic, D., et al., *Could growth factor-mediated extracellular matrix deposition and degradation offer the ground for directed pharmacological targeting in fibrosarcoma?* Curr Med Chem, 2013. **20**(23): p. 2868-2880.

32. Manzanares, D., et al., *Apical oxidative hyaluronan degradation stimulates airway ciliary beating via RHAMM and RON.* Am J Respir Cell Mol Biol, 2007. **37**(2): p. 160-168.

33. Hall, C.L., et al., *pp60(c-src) is required for cell locomotion regulated by the hyaluronanreceptor RHAMM.* Oncogene, 1996. **13**(10): p. 2213-2224.

34. Laurent, T.C. and Fraser, J., *Hyaluronan.* FASEB J, 1992. **6**(7): p. 2397-2404.

35. West, D.C., et al., *Angiogenesis induced by degradation products of hyaluronic acid.* Science, 1985. **228**: p. 1324-1327.

36. Weigel, P.H., et al., *The specific interaction between fibrin (ogen) and hyaluronan: possible consequences in haemostasis, inflammation and wound healing.* Cyba Found Symp, 1989. **143**: p. 248-261.

37. Toole, B.P. *Hyaluronan in morphogenesis*. Semin Cell Dev Biol, 2001. **12**(2): p. 79-87.

38. Ma, X., et al., *Loss of the hyaluronan receptor RHAMM prevents constrictive artery wall remodeling.* J Vasc Surg, 2014. **59**(3): p. 804-813.

39. Schmitt, M., et al., *Spreading of acute myeloid leukemia cells by trafficking along the peripheral outflow pathway of cerebrospinal fluid.* Anticancer Res, 2011. **31**(6): p. 2343-2345.

40. Pilarski, L.M., et al., *Potential role for hyaluronan and the hyaluronan receptor RHAMM in mobilization and trafficking of hematopoietic progenitor cells.* Blood, 1999. **93**(9): p. 2918-2927.

41. Kouvidi, K., et al., *Hyaluronan/RHAMM interactions in mesenchymal tumor pathogenesis: role of growth factors.* Adv Cancer Res, 2014. **123**: p. 319-349.

42. Turley, E.A., *Purification of a hyaluronate-binding protein fraction that modifies cell social behavior.* Biochem Biophys Res Commun, 1982. **108**(3): p. 1016-1024.

43. Hardwick, C., et al., *Molecular cloning of a novel hyaluronan receptor that mediates tumor cell motility.* J Cell Biol, 1992. **117**(6): p. 1343-1350.

44. Turley, E.A., Moore, D., and Hayden, L.J., *Characterization of hyaluronate binding proteins isolated from 3T3 and murine sarcoma virus transformed 3T3 cells.* Biochemistry, 1987. **26**(11): p. 2997-3005.

45. Yang, B., et al., *Identification of a common hyaluronan binding motif in the hyaluronan binding proteins RHAMM, CD44 and link protein.* Embo j, 1994. **13**(2): p. 286-296.

46. Ziebell, M.R. and Prestwich, G.D., *Interactions of peptide mimics of hyaluronic acid with the receptor for hyaluronan mediated motility (RHAMM).* J Comput Aided Mol Des, 2004. **18**(10): p. 597-614.

47. Mohapatra, S., et al., *Soluble hyaluronan receptor RHAMM induces mitotic arrest by suppressing Cdc2 and cyclin B1 expression.* J Exp Med, 1996. **183**(4): p. 1663-1668.

48. Nedvetzki, S., et al., *RHAMM, a receptor for hyaluronan-mediated motility, compensates for CD44 in inflamed CD44-knockout mice: a different interpretation of redundancy.* Proc Nat Acad Sci, 2004. **101**(52): p. 18081-18086.

49. Yang, B., Zhang, L., and Turley, E.A., *Identification of two hyaluronan-binding domains in the hyaluronan receptor RHAMM.* J Biol Chem, 1993. **268**(12): p. 8617-8623.

50. Ziebell, M.R. and Prestwich, G.D., *Interactions of peptide mimics of hyaluronic acid with the receptor for hyaluronan mediated motility (RHAMM).* J Comput Aided Mol Des, 2004. **18**(10): p. 597-614.

51. Bohaumilitzky, L., et al., *A Trickster in Disguise: Hyaluronan's Ambivalent Roles in the Matrix.* Front Oncol, 2017. **7**: p. 242.

52. Palasek, S.A., Cox, Z.J., and Collins, J.M., *Limiting racemization and aspartimide formation in microwave-enhanced Fmoc solid phase peptide synthesis.* J Pept Sci, 2007. **13**(3): p. 143-148.

53. Hardwick, C., et al., *Molecular cloning of a novel hyaluronan receptor that mediates tumor cell motility.* J Cell Biol, 1992. **117**(6): p. 1343-1350.

54. Vigetti, D., et al., *Hyaluronan: Biosynthesis and signaling.* Biochim Biophysic Acta, 2014. **1840**(8): p. 2452-2459.

55. White, P., et al., *Expediting the Fmoc solid phase synthesis of long peptides through the application of dimethyloxazolidine dipeptides.* J Pept Sci, 2004. **10**(1): p. 18-26.

56. Larsen, B.D. and Holm, A., *Incomplete Fmoc deprotection in solid-phase synthesis of peptides.* Int J Pept Protein Res, 1994. **43**(1): p. 1-9.

57. Nicolás, E., et al., *A new approach to Hmb-backbone protection of peptides: Synthesis and reactivity of Nα-Fmoc-Nα-(Hmb)amino acids.* Tetrahedron Lett, 1997. **38**(13): p. 2317-2320.

58. Simmonds, R.G., *Use of the Hmb backbone-protecting group in the synthesis of difficult sequences.* Int J Pept Protein Res, 1996. **47**(1-2): p. 36-41.

59. Mutter, M., et al., *Pseudo-prolines (psi Pro) for accessing "inaccessible" peptides.* Pept Res, 1995. **8**(3): p. 145-153.

60. Haack, T. and Mutter, M., *Serine derived oxazolidines as secondary structure disrupting, solubilizing building blocks in peptide synthesis.* Tetrahedron Lett, 1992. **33**(12): p. 1589-1592.

61. Wöhr, T., et al., *Pseudo-Prolines as a Solubilizing, Structure-Disrupting Protection Technique in Peptide Synthesis.* J Am Chem Soc, 1996. **118**(39): p. 9218-9227.

62. Bedford, J., et al., *Amino acid structure and "difficult sequences" in solid phase peptide synthesis.* Int J Pept Protein Res, 1992. **40**(3-4): p. 300-307.

63. Nikitovic, D., et al., *Cancer microenvironment and inflammation: role of hyaluronan.* Front Immunol, 2015. **6**: p. 169.

64. Misra, S., et al., *Interactions between Hyaluronan and Its Receptors (CD44, RHAMM) Regulate the Activities of Inflammation and Cancer.* Front Immunol, 2015. **6**: p. 201.

65. Tolg, C., et al., *Genetic deletion of receptor for hyaluronan-mediated motility (Rhamm) attenuates the formation of aggressive fibromatosis (desmoid tumor).* Oncogene, 2003. **22**(44): p. 6873-6882.

66. Shigeeda, W., et al., *Hyaluronic acid enhances cell migration and invasion via the YAP1/TAZ-RHAMM axis in malignant pleural mesothelioma.* Oncotarget, 2017. **8**(55): p. 93729-93740.

67. Mele, V., et al., *The hyaluronan-mediated motility receptor RHAMM promotes growth, invasiveness and dissemination of colorectal cancer.* Oncotarget, 2017. **8**(41): p. 70617-70629.

68. Mascaro, M., et al., *Low molecular weight hyaluronan induces migration of human choriocarcinoma JEG-3 cells mediated by RHAMM as well as by PI3K and MAPK pathways.* Histochem Cell Biol, 2017. **148**(2): p. 173-187.

69. Thangavel, C., et al., *RB Loss Promotes Prostate Cancer Metastasis.* Cancer Res, 2017. **77**(4): p. 982-995.

70. Banerji, S., et al., *Structures of the Cd44-hyaluronan complex provide insight into a fundamental carbohydrate-protein interaction.* Nat Struct Mol Biol, 2007. **14**(3): p. 234-239.

71. Lesley, J., et al., *Hyaluronan binding by cell surface CD44.* J Biol Chem, 2000. **275**(35): p. 26967-26975.

72. Nightingale, T.D., et al., *A mechanism of sialylation functionally silences the hyaluronan receptor LYVE-1 in lymphatic endothelium.* J BiolChem, 2009. **284**(6): p. 3935-3945.

73. Banerji, S., et al., *Homodimerization of the Lymph Vessel Endothelial Receptor LYVE-1 through a Redox-labile Disulfide Is Critical for Hyaluronan Binding in Lymphatic Endothelium.* J Biol Chem, 2016. **291**(48): p. 25004-25018.

74. Lawrance, W., et al., *Binding of Hyaluronan to the Native Lymphatic Vessel Endothelial Receptor LYVE-1 Is Critically Dependent on Receptor Clustering and Hyaluronan Organization.* J Biol Chem, 2016. **291**(15): p. 8014-8030.

75. Wolny, P.M., et al., *Analysis of CD44-hyaluronan interactions in an artificial membrane system: insights into the distinct binding properties of high and low molecular weight hyaluronan.* J Biol Chem, 2010. **285**(39): p. 30170-30180.

76. Hall, C.L., et al., *Overexpression of the hyaluronan receptor RHAMM is transforming and is also required for H-ras transformation.* Cell, 1995. **82**(1): p. 19-28.

77. Savani, R.C., et al., *Migration of bovine aortic smooth muscle cells after wounding injury. The role of hyaluronan and RHAMM.* J Clin Investig, 1995. **95**(3): p. 1158-1168.

78. Esguerra, K.V., et al., *Identification, design and synthesis of tubulin-derived peptides as novel hyaluronan mimetic ligands for the receptor for hyaluronan-mediated motility (RHAMM/HMMR).* Integr Biol, 2015. **7**(12): p. 1547-1560.

2.6 Supplemental Information

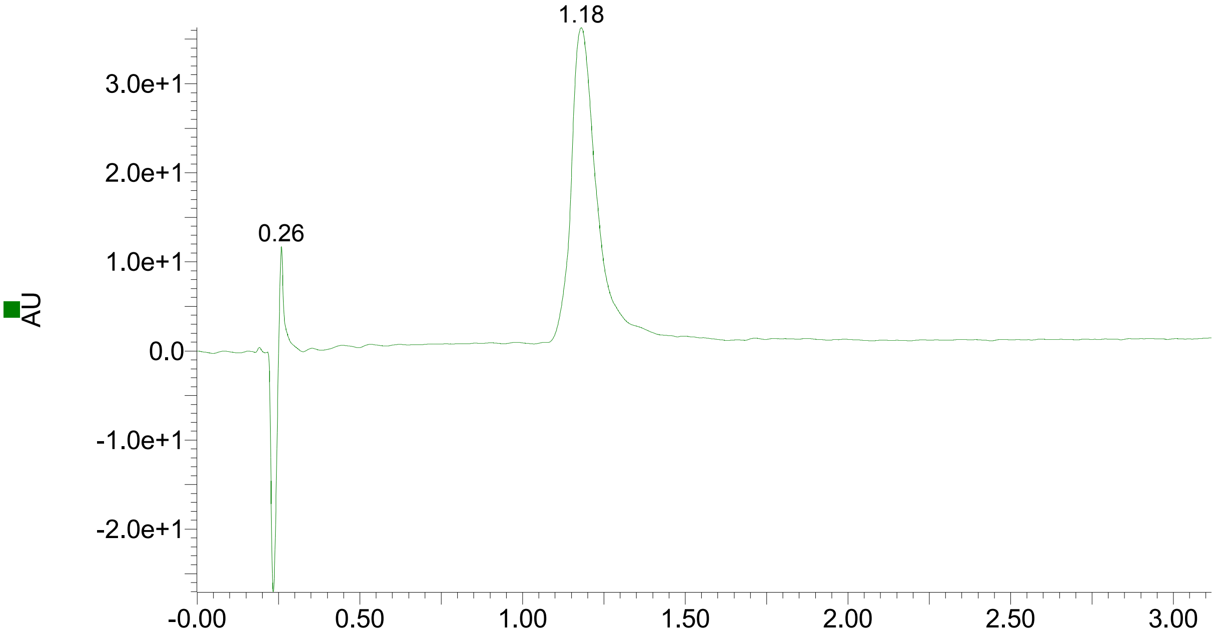

Figure S 2.1. UHPLC trace of 7 kDa RHAMM

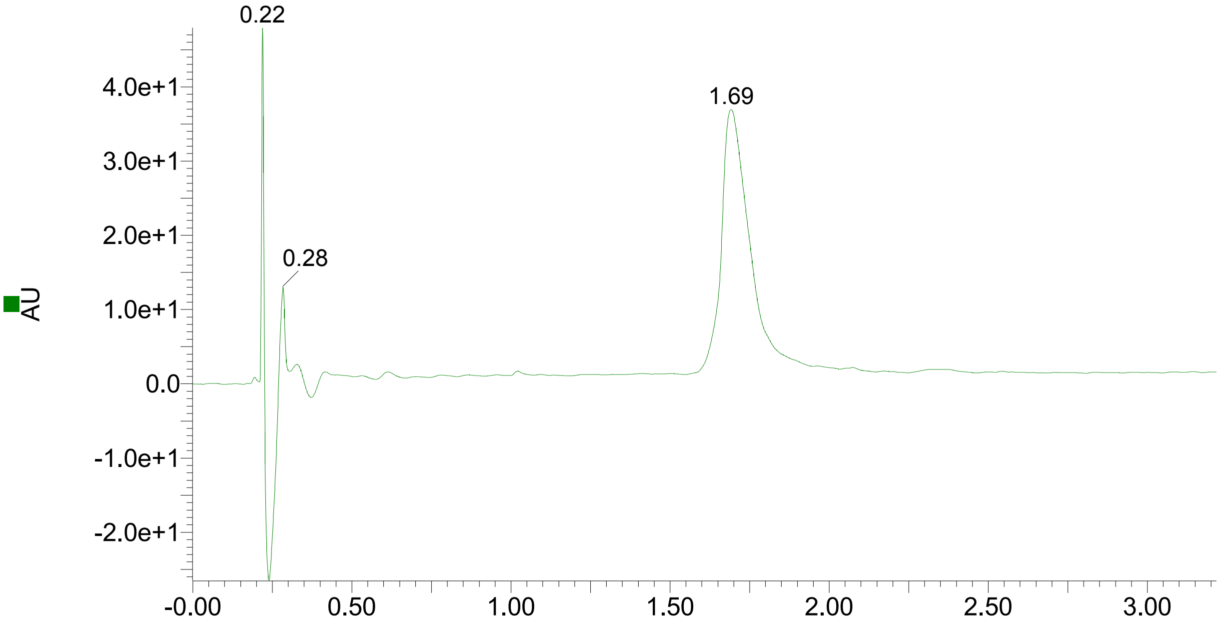

Figure S 2.2. UHPLC trace of Ala-7 kDa RHAMM

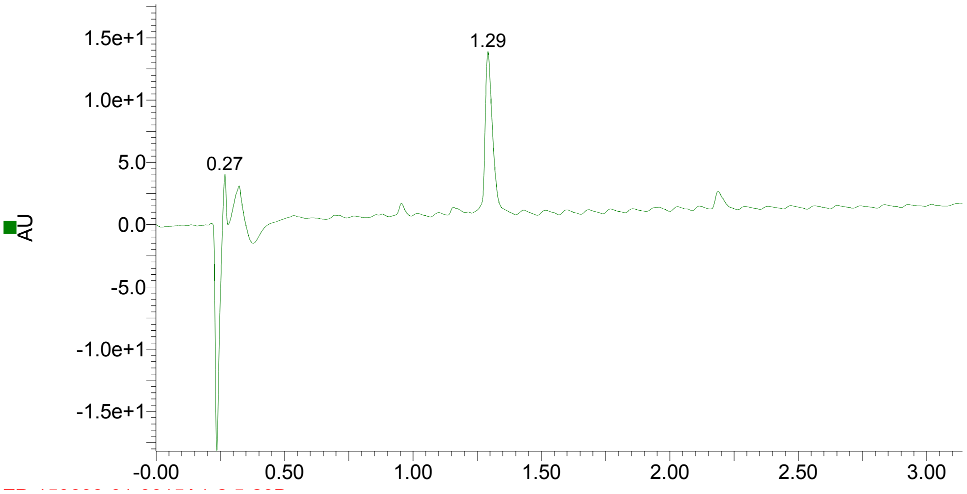

Figure S 2.3. UHPLC trace of 2b (H-VEGEGEEEGEEY-NH₂)

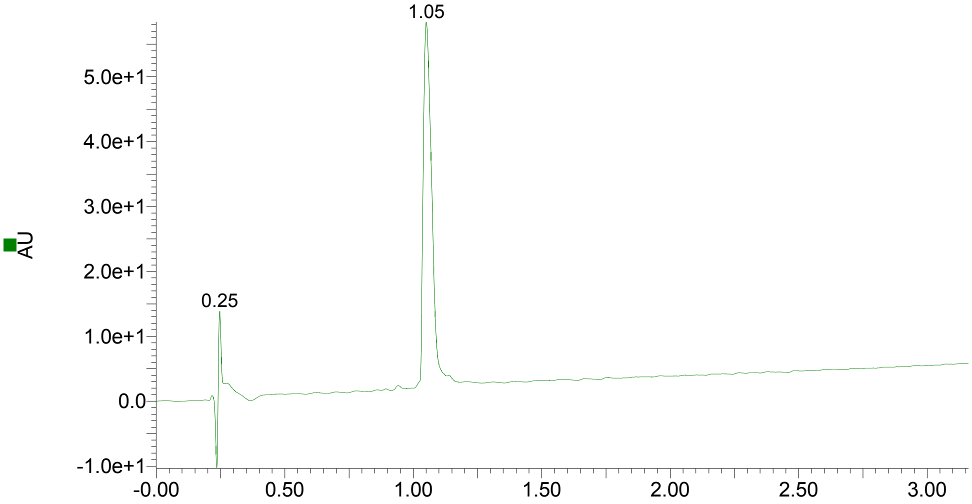

Figure S 2.4. UHPLC trace of 3b (H-SVEAEAEEGEEY-NH₂)

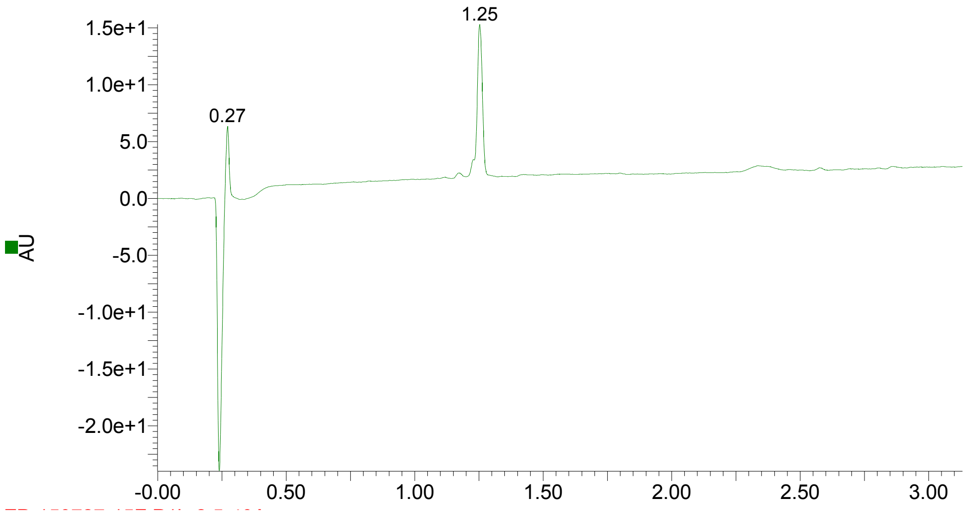

Figure S 2.5. UHPLC trace of 10b (H-EEDFGEEAEEEA-NH$_2$)

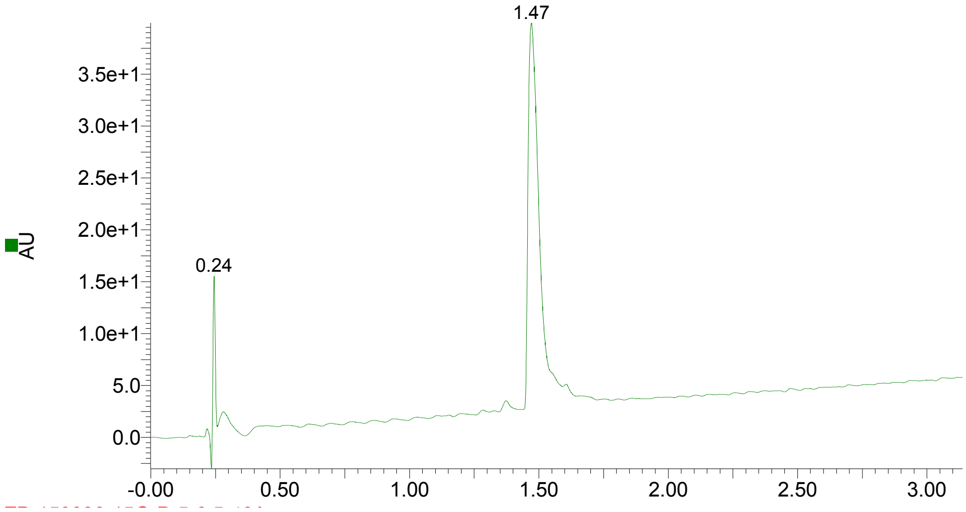

Figure S 2.6. UHPLC trace of 11b (H-GEFEEEAEEEVA-NH$_2$)

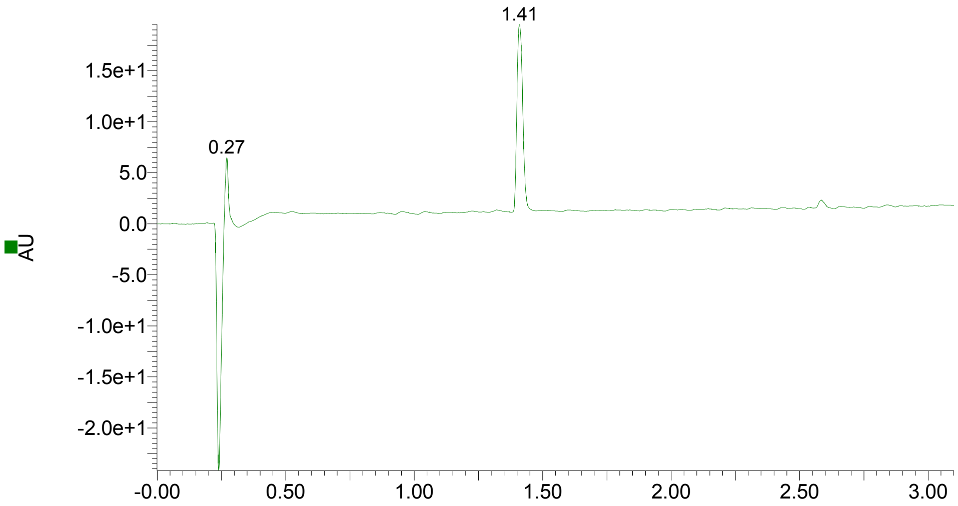

Figure S 2.7. UHPLC trace of 12b (H-EAFEDEEEEIDG-NH$_2$)

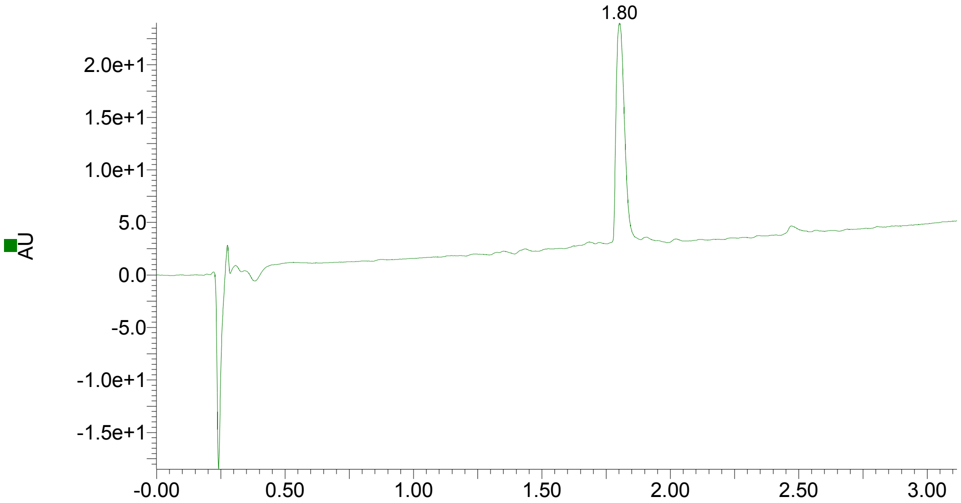

Figure S 2.8. UHPLC trace of 14b (H-FTEAESNMNDLV-NH$_2$)

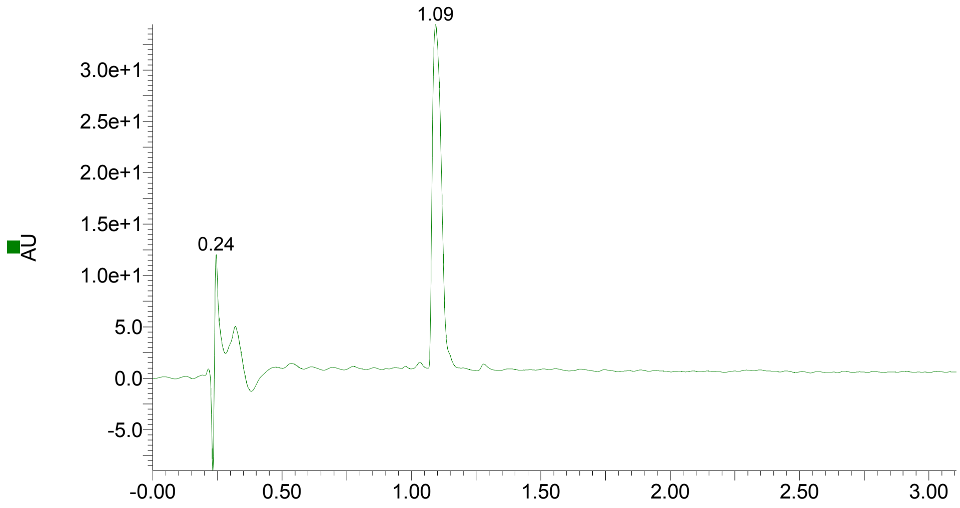

Figure S 2.9. UHPLC trace of 7a (H-GEFSEAREDMAA-NH_2)

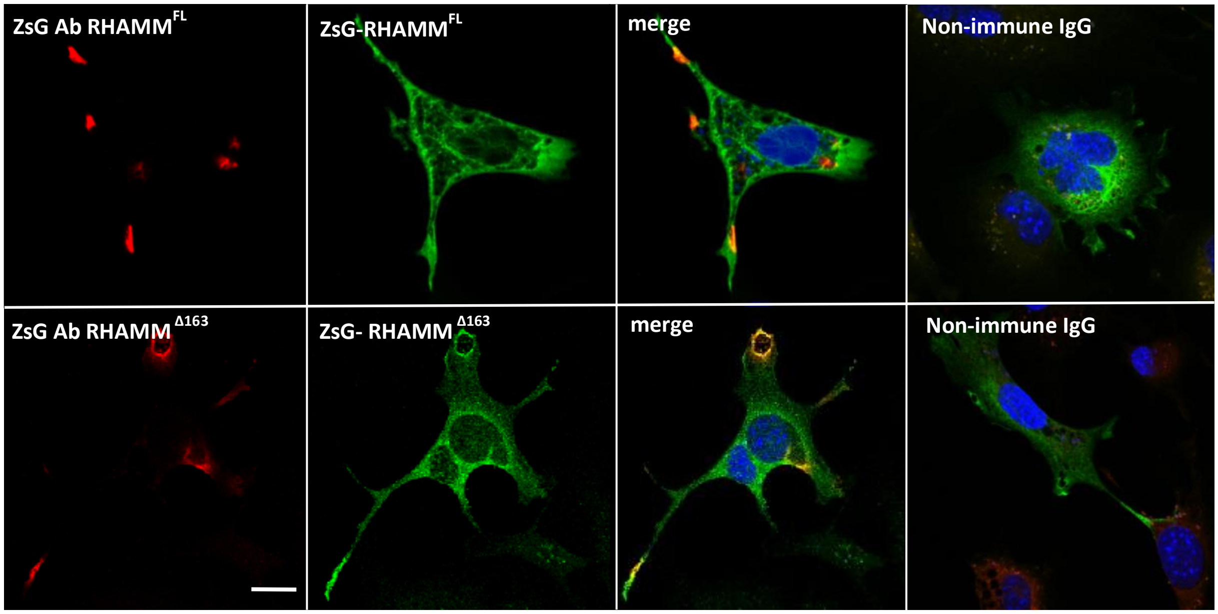

Figure S 2.10. 10T1/2 mesenchymal cells display RHAMM in cell processes and adhesion sites. 10T1/2 cells were transfected with full-length Zs-Green tagged RHAMM (green, top panel) and Zs-Green tagged RHAMM$^{\Delta 163}$ (bottom panel). The tagged cell surface RHAMM was detected by co-localization of Zs-green antibody staining (red) with Zs-green fluorescence in non-permeabilized cells and is present in cell processes. Intracellular RHAMM, which is detected as green fluorescence only, is diffused in the cytoplasm. Scale bar, 20 µM.

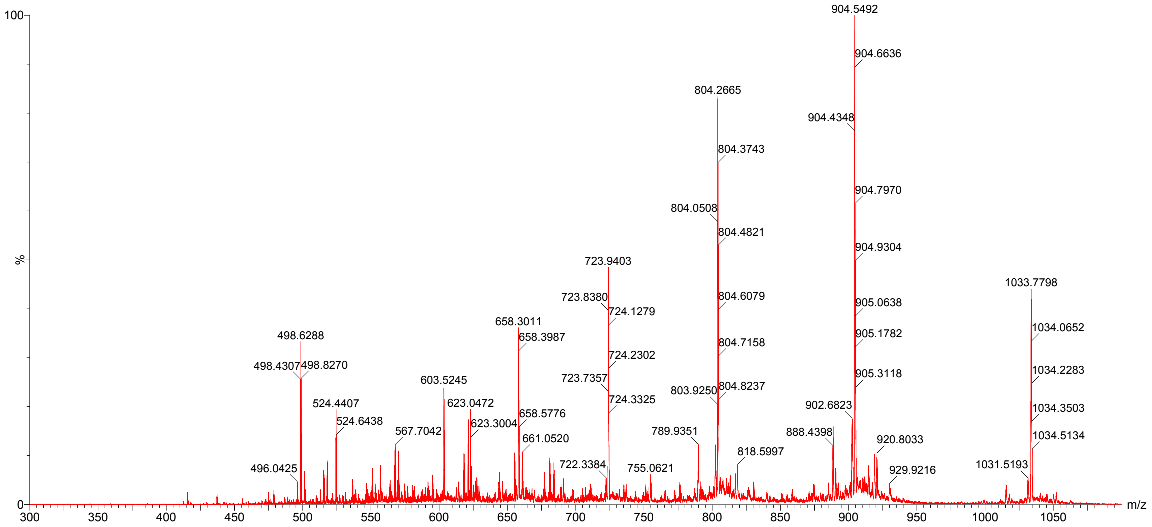

Figure S 2.11. ESI$^+$ Mass Spectrum for 7 kDa RHAMM

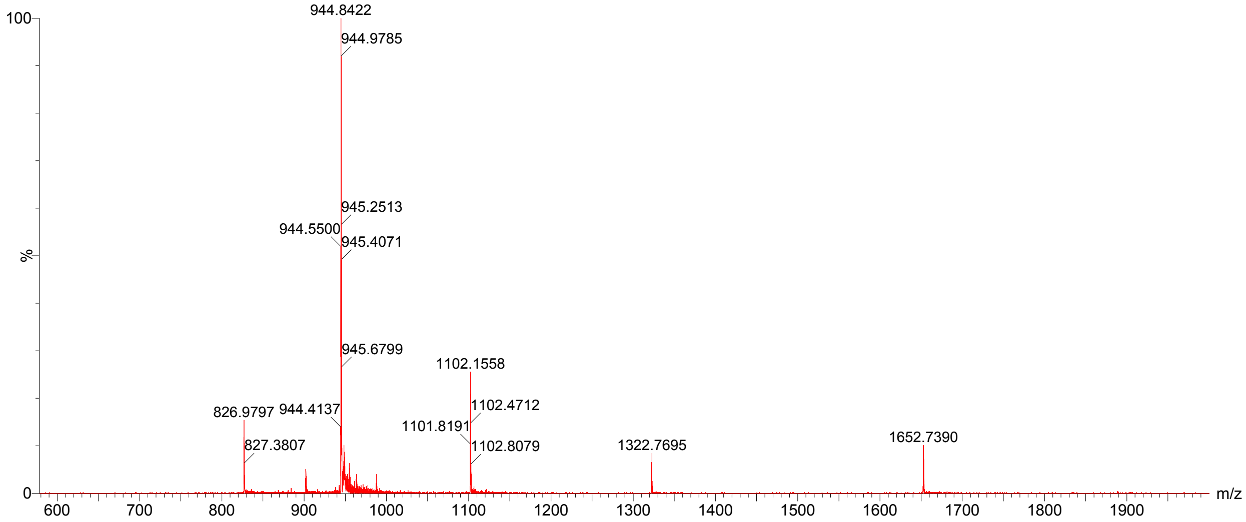

Figure S 2.12. ESI$^+$ Mass Spectrum for Ala-7 kDa RHAMM

Table S 2.1. Calculated and observed m/z peaks of 7 kDa RHAMM

	m/z calculated	m/z observed
$[M+5H]^{5+}$	1446.55	1446.47
$[M+6H]^{6+}$	1205.59	1205.63
$[M+7H]^{7+}$	1033.88	1033.78
$[M+8H]^{8+}$	904.39	904.45
$[M+9H]^{9+}$	804.15	804.12
$[M+10H]^{10+}$	723.72	723.77
$[M+11H]^{11+}$	658.11	658.09
$[M+12H]^{12+}$	603.20	603.23

Table S 2.2. Calculated and observed m/z peaks of Ala-7 kDa RHAMM

	m/z calculated	m/z observed
$[M+4H]^{4+}$	1651.89	1562.02
$[M+5H]^{5+}$	1321.71	1321.94
$[M+6H]^{6+}$	1101.60	1101.65
$[M+7H]^{7+}$	944.37	944.39
$[M+8H]^{8+}$	826.45	826.62

Table S 2.3. Calculated and observed m/z peaks of tubulin-derived peptides

Peptide ID [49]	Peptide Sequence	Mmono calculated	Mmono observed	m/z calculated	m/z observed	Purity (%)
2b	H-VEGEGEEEGEEY-NH_2	1353.52	1358.28	677.77	677.56	>92
3b	H-SVEAEAEEGEEY-NH_2	1339.53	1339.30	670.77	670.66	>95
10b	H-EEDFGEEAEEEA-NH_2	1381.51	1381.28	691.76	691.65	>95
11b	H-GEFEEEAEEEVA-NH_2	1365.55	1365.39	683.78	683.70	>94
12b	H-EAFEDEEEEIDG-NH_2	1409.54	1409.56	705.33	705.79	>93
14b	H-FTEAESNMNDLV-NH_2	1367.60	1368.08	684.81	684.43	>94
7a	H-GEFSEAREDMAA-NH_2	1310.55	1311.44	656.28	656.73	>97

Figure S 2.13. ESI$^+$ Mass Spectrum for Peptide 2b (H-VEGEGEEEGEEY-NH_2)

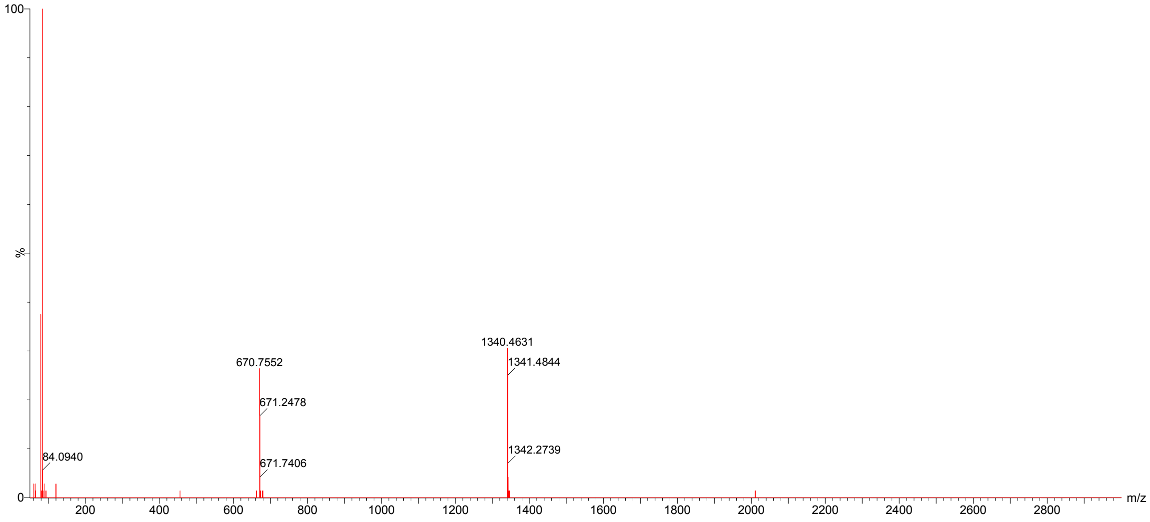

Figure S 2.14. ESI$^+$ Mass Spectrum for Peptide 3b (H-SVEAEAEEGEEY-NH$_2$)

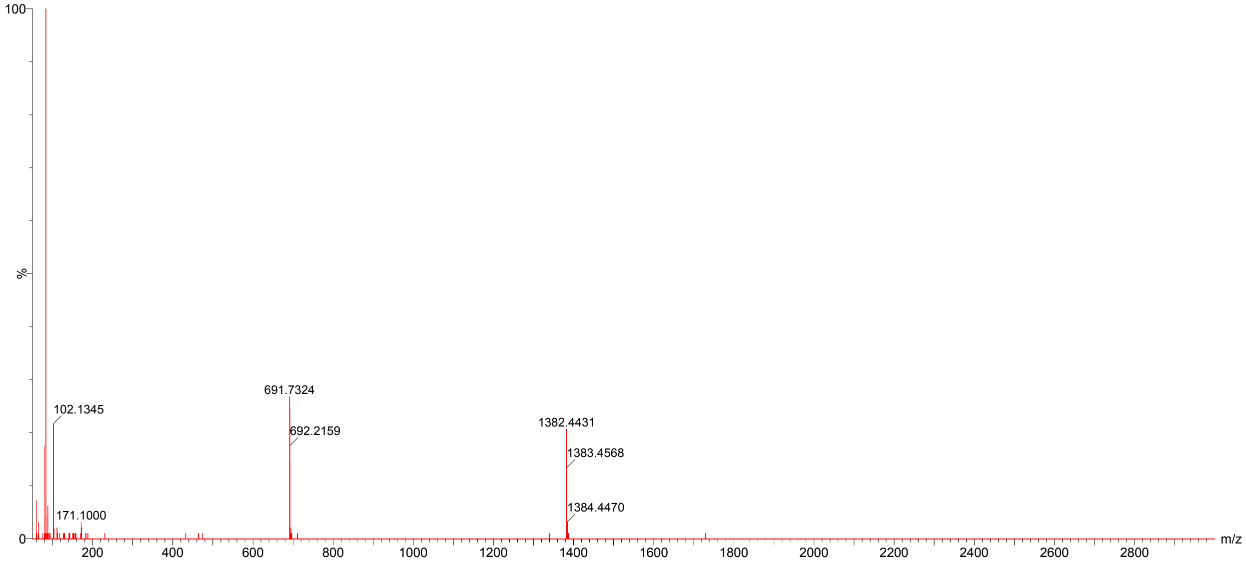

Figure S 2.15. ESI$^+$ Mass Spectrum for Peptide 10b (H-EEDFGEEAEEEA-NH$_2$)

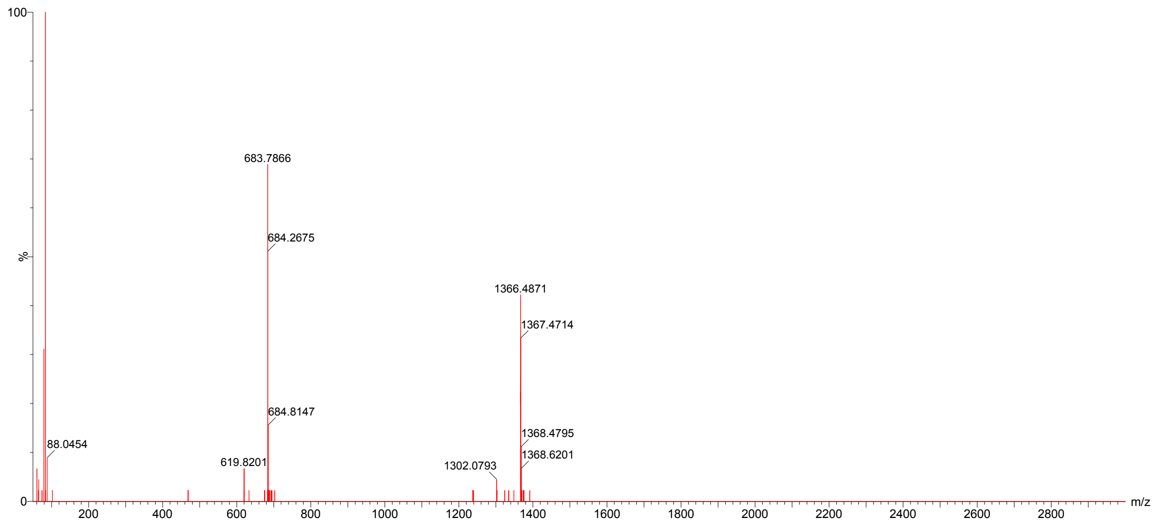

Figure S 2.16. ESI^{+} Mass Spectrum for Peptide 11b (H-GEFEEEAEEEVA-NH$_2$)

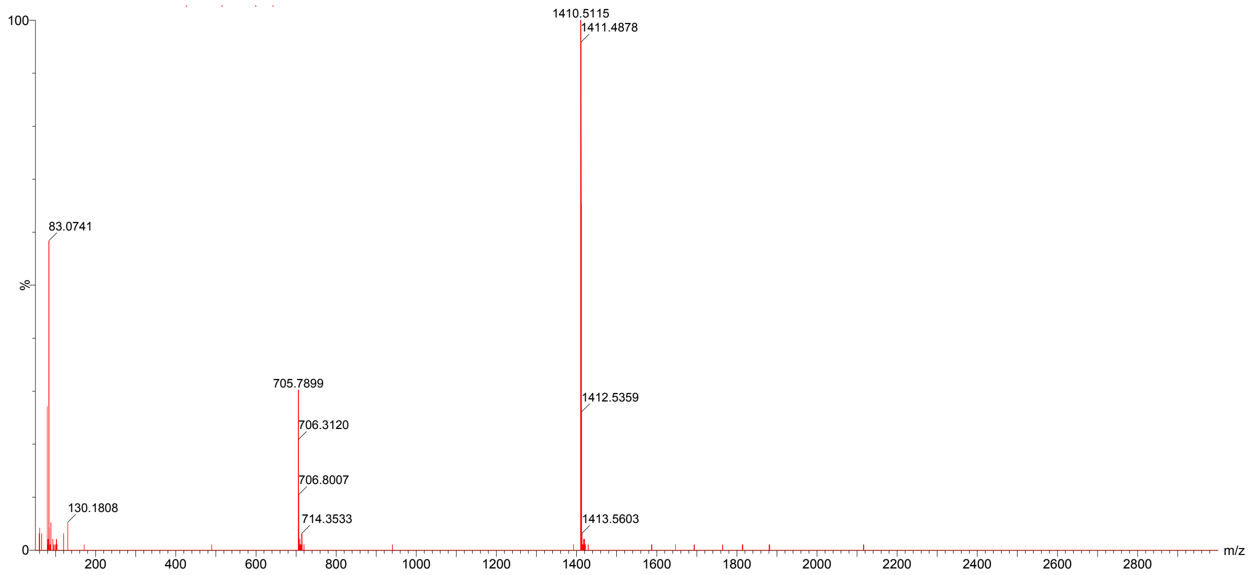

Figure S 2.17 ESI^{+} Mass Spectrum for Peptide 12b (H-EAFEDEEEEIDG-NH$_2$)

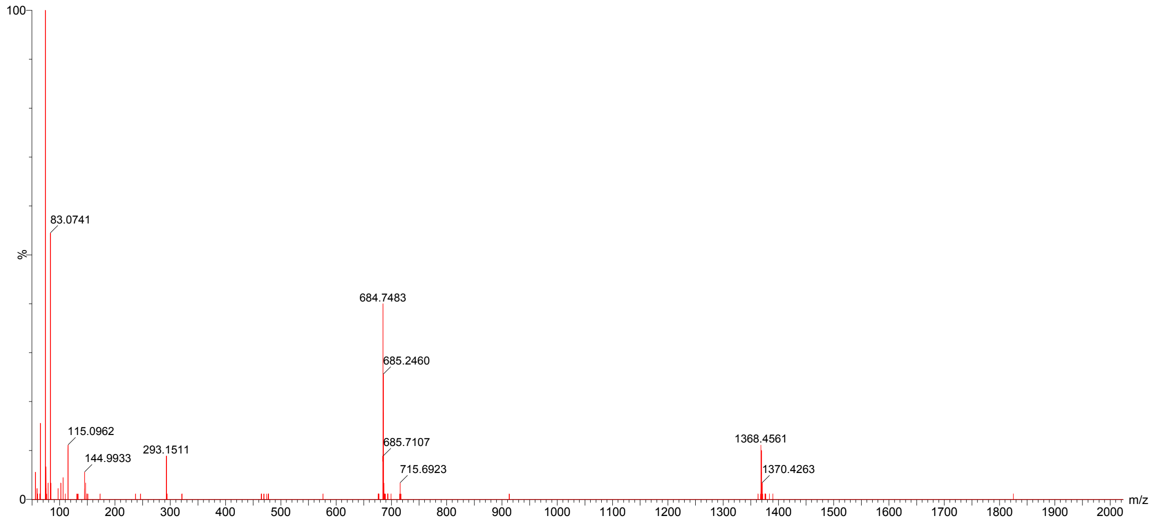

Figure S 2.18. ESI$^+$ Mass Spectrum for Peptide 14b (H-FTEAESNMNDLV-NH$_2$)

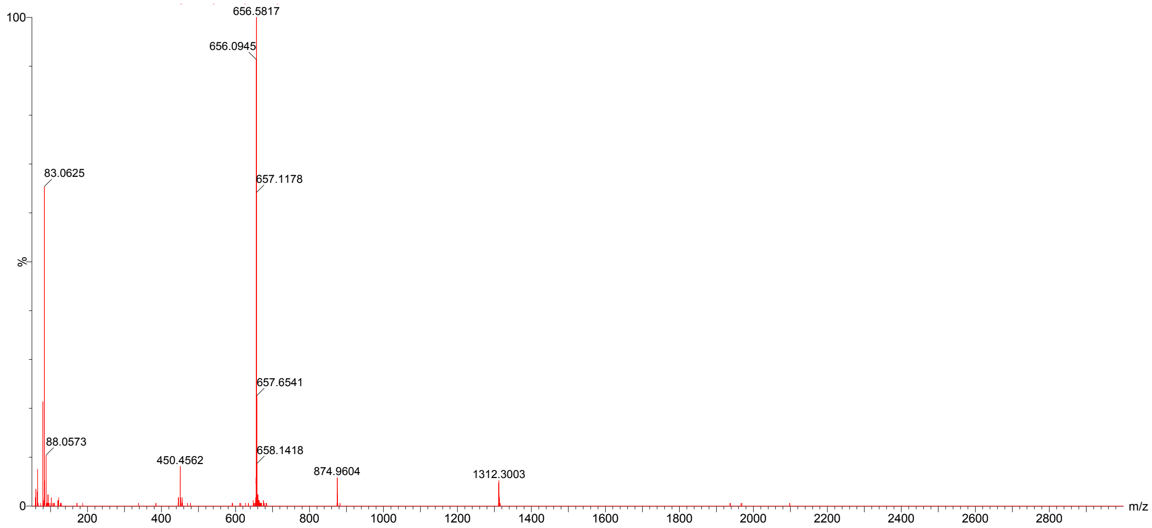

Figure S 2.19. ESI$^+$ Mass Spectrum for Peptide 7a (H-GEFSEAREDMAA-NH$_2$)

Chapter 3

3 The Development of RHAMM Peptide Mimetics for Blocking Inflammation

3.1 Introduction

Hyaluronan is a nonsulfated, linear glycosaminoglycan (GAG) that is composed of repeating disaccharide units of (ß, 1-4) glucuronic acid (GlcUA) and (ß, 1-3) N-acetylglucosamine (GlcNAc). In homeostatic tissues, native HA is a polysaccharide that has a high molecular weight (HMW) of >500 kDa. Native HMW HA is the major carbohydrate component of the extracellular matrix (ECM) in all tissues, where it acts to maintain water homeostasis and matrix structure [1], and as such, plays a vital role in tissue organization and cellular behaviour, including proliferation, growth, and motility [2-8]. However, like many other components of the ECM, HMW HA is broken down to oligosaccharide fragments by hyaluronidases (HYALs) and free radicals (reactive oxygen/nitrogen species, ROS/RNS) in response to cellular stresses, resulting in the accumulation of lower molecular weight (LMW) forms of the polysaccharide that have different functions than their native HMW precursors [9-13]. Many of HA's functions appear to be mediated through specific HA receptors, including LYVE-1, Stab2, CD44 and receptor for hyaluronan mediated motility (RHAMM/HMMR/CD168). Fragmented HA-HA receptor interactions have been shown to increase inflammation, fibrosis and angiogenesis, all of which are processes that have the potential to lead to development of disease.[11, 13-16]. In the case of inflammation specifically, their increased interaction activates macrophages and the expression of pro-inflammatory genes and cytokines, such as macrophage chemoattractant protein-1 (MCP-1), Interleukin-8 (IL-8), RANTES, and TNF-α [17]. A positive feedback loop is also possible when an HA-induced inflammatory response perpetuates further inflammatory processes; inflammation leads to inflammation, and this may eventually lead to fibrosis [7]. Thus, scavenging HA fragments, and preventing HA fragment-HA receptor interactions with targeted entities has both a preventative and therapeutic application.

RHAMM is unique among the group of HA receptor proteins in its strong binding affinity and specificity for HA (Hauser-Kawaguchi, et al., submitted). In addition, unlike the other HA receptors, which bind HA through a link module binding motif [18], RHAMM binds HA through two HA binding domains, both of which have a BX_7B binding motif, where B represents a basic amino acid, and X represents any non-acidic amino acid [19]. Further, RHAMM binds directly to microtubules [20, 21] and TPX2/AURKA A [22, 23] through the leucine zipper that exists between the two HA binding domains. RHAMM is largely present in the cytoplasm and nucleus, where its expression is tightly regulated [24-26], but is also exported to the cell membrane by unconventional mechanisms in response to cellular stress, where it associates with transmembrane receptors including CD44 and PDGFR in order to activate ERK 1,2 [20, 27-29] and focal adhesion kinase (FAK) [30] signaling pathways. The exact signal transduction mechanism of RHAMM-HA-induced signaling has not yet been fully characterized.

Several RHAMM mimetic peptides have been reported to have functional properties [30, 31]. Here, we report the design and synthesis of the first cyclized RHAMM peptide inhibitors and show that this strategy is effective for targeting HA fragments and blocking HA fragment-induced signaling outcomes. Specifically, these RHAMM mimetics have been stabilized by two lactam bridge staples that are adjacent to one another, which we have shown facilitate ligand binding, and therefore, bioactivity both in culture and *in vivo*, suggesting that they have therapeutic potential in treating inflammation-related diseases.

3.2 Results and Discussion

The development of peptide mimetics that bind to HA fragments has proven successful as a therapeutic approach in experimental models of inflammation and other diseases. These peptides bind directly to and sequester HA fragments, which are therefore prevented from binding and activating receptors.

We have developed 30mer RHAMM peptide mimetics that incorporate both HA binding domains of RHAMM as well as the linker region that connects them. Our aim was to develop peptides that have improved affinity towards their target HA, resulting in improved efficiency for scavenging HA, and therefore, are more effective at blocking HA fragment-induced signaling in culture and *in vivo*.

We have identified RHAMM peptide mimetics that have been stabilized by the insertion of lactam bridge staples in the portion of the peptide sequence that lies between the two HA binding domains. We propose that these peptides are prototypical drug molecules, especially our lead compound, Peptide **3.1**, and its variants, which may be used for the treatment of conditions that arise from HA signaling, especially those that involve a strong inflammatory response, such as pro-inflammatory conditions and some cancers.

RHAMM has been reported to be a largely helical protein, and specifically, the two HA binding domains have been reported to have helical character. It has been hypothesized that the arrangement of the binding domains in this structure facilitates the correct orientation of the basic residues in the BX_7B binding motif towards the target so that the two molecules will interact [32]. To this end, two adjacent (*i*, *i*+4) lactam bridge staples were inserted between the two HA binding domains in order to stabilize the linker region and confer further helicity to the shortened RHAMM peptides. In addition, we investigated whether the order of amino acids forming the lactam bridge was important for HA binding, as it has been reported that staples formed by a Lys-Glu staple were less efficient in improving helicity over the Glu-Lys counterpart [33].

In order for the RHAMM peptide mimetics to prevent the activation of signaling pathways, they are required to target and scavenge HA fragments. As expected, all of the compounds bound to HA, as they contain the HABDs, which are required for ligand binding. However, the improvement in ligand-binding observed in the cyclized peptides is noteworthy. Cyclization significantly improved the affinity of these compounds for HA compared to the linear peptide in all cases, as well as decreased their dissociation from HA, suggesting that the double stapled peptides are more specific for their target than their linear counterpart. The most notable increase resulted in the case of Peptide **3.1**, in which both staples were formed by the conjugation of the side chains of an N-terminal Glu and C-terminal Lys residue. Interestingly, switching the order of staple-forming residues decreases the compound’s binding affinity for the ligand (Peptides **3.3** and **3.4**). Because the sequence or placement of the staples does not vary between Peptide **3.1** and Peptides **3.3** and **3.4**, the difference in binding affinity is likely due to the difference in secondary structure of the overall compound, where improved helicity results in improved HA-binding. This insertion and placement of the staples confers rigidity into the structure, cyclizing the linker region of the peptide, ensuring that the HABDs are accessible to the ligand.

Table 3.1. Sequences of double stapled RHAMM peptide mimetics and their linear counterpart. Side-chain cyclization indicated by square brackets.

Peptide ID	Sequence
Linear	Ac-KIKHVVKLKDENSQLKSEVSKLRSQLVKRK-NH_2
3.1	Ac-KIKHVVKLK[EENSK][EKSEK]SKLRSQLVKRK-NH_2
3.2	Ac-KIKHVVKLKD[ENSQK][ESEVK]KLRSQLVKRK-NH_2
3.3	Ac-KIKHVVKLK[EENSK][KKSEE]SKLRSQLVKRK-NH_2
3.4	Ac-KIKHVVKLK[KENSE][EKSEK]SKLRSQLVKRK-NH_2

3.2.1 CD Spectroscopy

The importance of the secondary structure of RHAMM’s HABDs is a well-accepted characteristic for the ligand binding to the receptor [32, 34, 35]. We evaluated the secondary structure of each of the peptides by CD spectroscopy, and determined the mean residue ellipticity of the peptides by taking the ratios of the values at the two minima that are characteristic of an alpha-helix, 208 and 222 nm. The closer the ratio approaches a value of 1, the closer the peptide achieves perfect helicity, while a greater value at 208 nm than at 222 nm suggests the presence of additional conformations in the structure, such as some beta sheet or random coil properties [36]. The secondary structure of the linear peptide was observed to have a mean residue ellipticity of 0.32 in water, suggesting some degree of alpha-helical character, which improved to 0.80 in a 40% TFE solution, following stabilization of the compound's inherent secondary structure [37]. All of the double stapled peptides were reported to exhibit an increase in helicity compared to their linear counterpart. The peptide with the highest degree of helical character was Peptide **3.1**.

The availability of the RHAMM binding domains in the correct conformation is a requirement for binding of the receptor to the ligand. Therefore, some alpha-helical character observed in the linear peptide, which contains both HABDs, is expected, but the minimal degree of helicity is the result of a lack of hydrophobic residues that would contribute to a hydrophobic core [35]. Cyclization of the peptide backbone is a commonly used technique that decreases the flexibility and free rotation of individual bonds contained within the staple, as well as facilitates the distinct formation of an alpha-helical secondary structure. Thus, the addition of staples in the peptide backbone within the linker region acts to stabilize the inherent helicity present within the peptide sequence, evidenced by the linear peptide, and identify those compounds with the greatest potential for targeting HA fragments and preventing HA signaling.

Table 3.2. Mean residue ellipticities of linear and double stapled peptides at 0.25 mg/mL of peptide

Peptide ID	**Water** $[\theta]_{222}/[\theta]_{208}$	**Water + 40% TFE** $[\theta]_{222}/[\theta]_{208}$
Linear	0.32	0.80
3.1	0.65	0.85
3.2	0.48	0.83
3.3	0.37	0.83
3.4	0.41	0.81

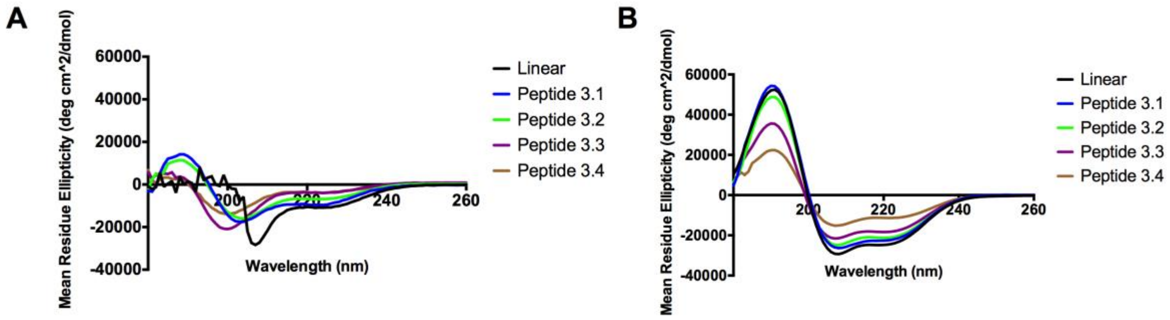

Figure 3.1. Stapling RHAMM peptide mimetics increases helicity compared to the linear peptide by CD spectroscopy in both water (A) and 40% TFE solution (B)

3.2.2 Cyclized RHAMM peptide mimetics bind hyaluronan with high affinity

All of the peptides were evaluated for their binding to LMW HA fragments (5-10 kDa). Cystamine-functionalized HA [38] was covalently conjugated to a gold nanoparticle surface, providing a biosensor for SPR experiments. PEG thiol was used to block any available sites on the chip in order to prevent nonspecific binding of the peptides to the gold surface (data not shown).

All of the peptides were observed to bind to the 5-10 kDa HA surface over a range of peptide concentrations, including the linear peptide. All of the double stapled peptides (**3.1** – **3.4**) had improved binding to HA over the linear peptide, as well as a slower dissociation rate. Peptide **3.1** had the strongest binding to HA, binding the ligand with a K_D of 88 nM, and was found to have the slowest dissociation from the HA surface.

Table 3.3. Kinetic analysis of linear and double stapled peptides

Peptide ID	Average k_a (10^3/(M*s))	Average k_d (10^{-4}/s)	Average K_D (nM)
Linear	2.6 ± 0.1	3.4 ± 0.3	1260.2 ± 24.8
3.1	5.3 ± 0.2	4.7 ± 0.5	88.5 ± 6.3
3.2	7.0 ± 0.4	1.7 ± 0.7	240.3 ± 16.4
3.3	7.6 ± 0.8	1.4 ± 0.8	168.4 ± 21.1
3.4	6.1 ± 0.5	1.4 ± 0.4	230.6 ± 13.8

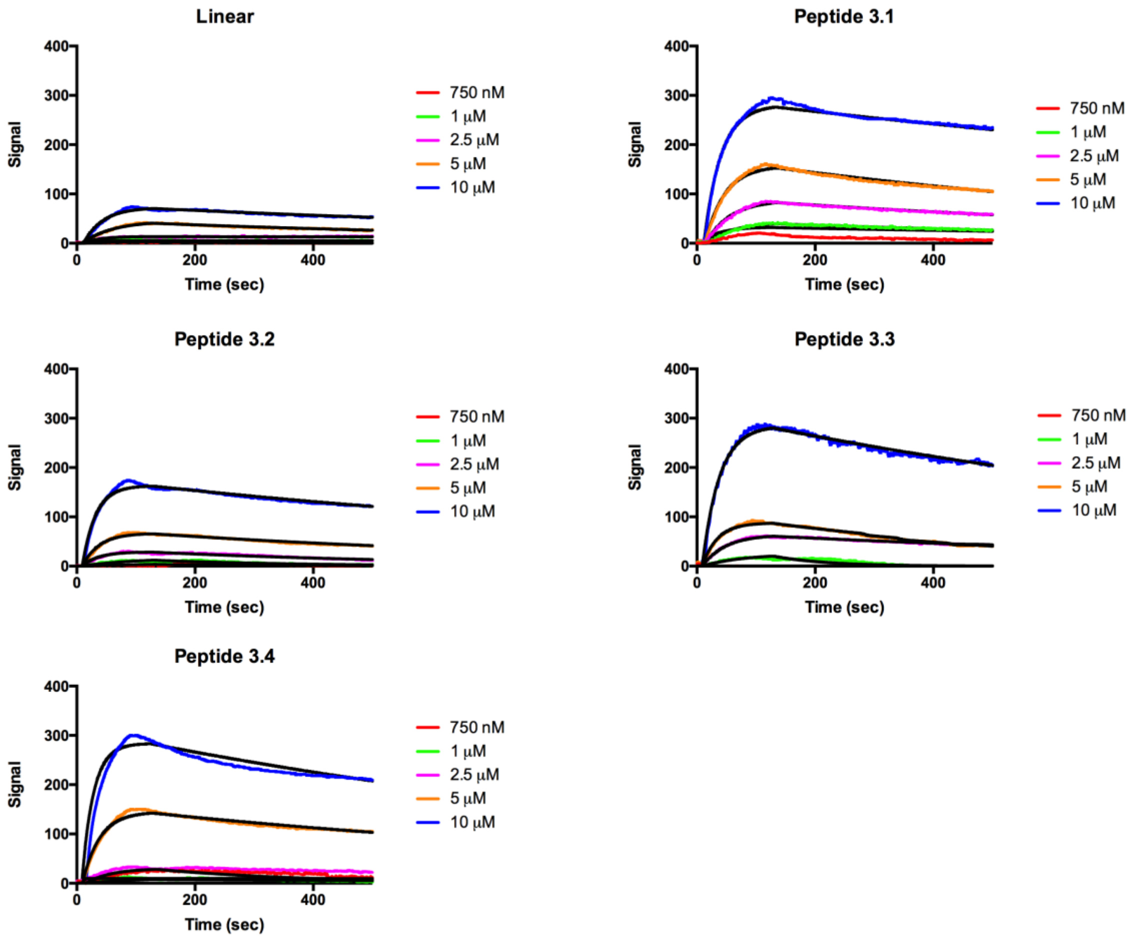

Figure 3.2. SPR signals of linear and stapled peptides. Stapling and staple placement are important for HA-binding. Each signal corresponds to the response of 5 peptide concentrations (750 nM, 1 μM, 2.5 μM, 5 μM, and 10 μM). The solid lines indicate a global 1:1 interaction curve fitting model for each of the interactions.

3.2.3 Cyclized RHAMM peptide mimetics block inflammation

RHAMM expression is induced in macrophages following tissue injury or cellular stress, so blocking normal RHAMM function in sites of injury would reduce the RHAMM-mediated inflammatory response. Several approaches have been reported for blocking pro-inflammatory signaling that is mediated by HA fragments, including, but not limited to inhibiting HA synthesis by small molecules, such as 4-MU [39, 40], gene knockdown or knockout [41-43], blocking hyaluronidase production, and with targeted peptides that bind either HA or HA receptors [30, 31, 44, 45]. Here, we discuss and validate the first RHAMM-based cyclized peptides for treating inflammation. Other HA-targeted peptides have been developed and shown to have therapeutic potential in inflammation, wound repair, and fibrosis/adipogenesis models [31], and as such, this class of molecule offers considerable promise in regulating inflammation-based diseases and disorders.

The lead peptide was subjected to an inflammation protein array to determine the specific cytokines that would be the best readout to measure bioactivity of our peptide library. The mouse inflammation array was purchased from R&D Systems and performed according to manufacturer's protocol. Briefly, RAWBlue macrophages were stimulated with Toll-like receptor (TLR) agonist PAM3CSK4 to induce inflammation and treated with peptide at the same time for a period of 24 hours. The peptide was found to block the expression of a number of inflammatory cytokines measured in the array, the most notable of which was RANTES, where the peptide was able to bring the levels down close to that of the control (**Figure 3.3**).

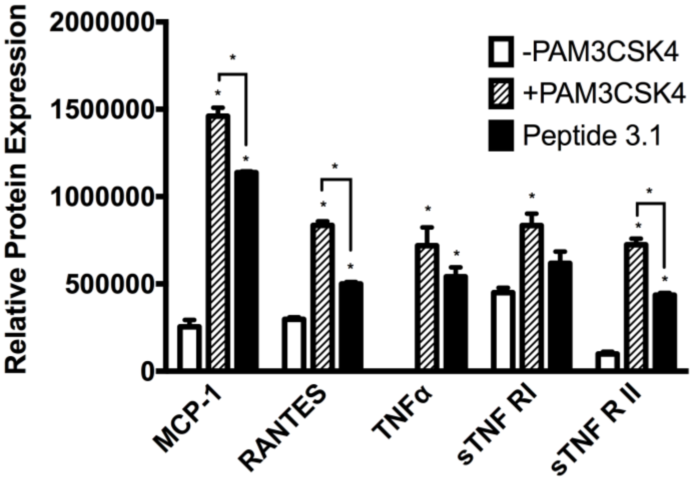

Figure 3.3. An inflammation protein array was performed on RAWBlue macrophages stimulated with TLR agonist PAM3CSK4 in the presence or absence of 1 μM of peptide

Peptide **3.1** was further validated *in vivo* where it blocked 54% of tumor necrosis factor alpha (TNF-α) levels under pro-inflammatory conditions following exposure to lipopolysaccharide (LPS) (**Figure 3.4**). By blocking cytokine recruitment *in vivo*, we have shown that our lead compound could potentially be used to prevent fragmented HA-mediated signaling, including macrophage recruitment.

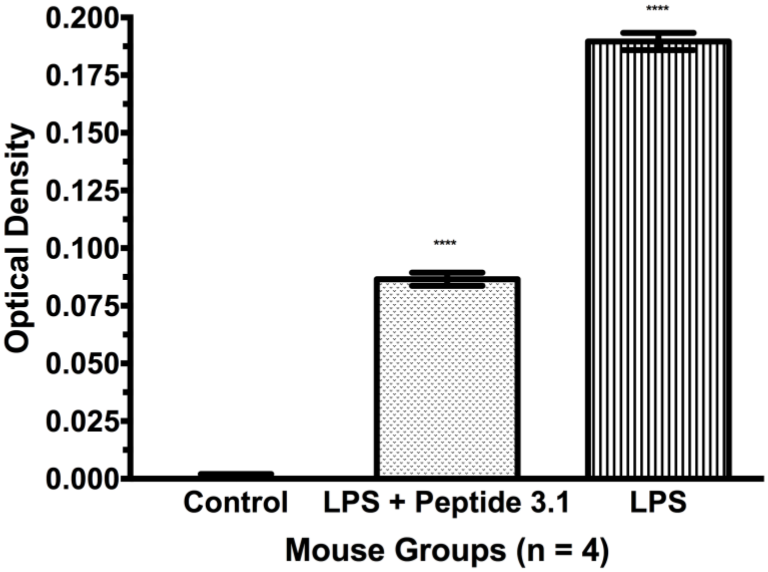

Figure 3.4. Preclinical evaluation of Peptide 3.1 was carried out in mice that were stimulated with lipopolysaccharide (LPS), a TLR agonist. Preliminary results demonstrate that a 54% decrease in TNF-α concentration is observed in the presence of Peptide 3.1 compared to the LPS.

In order to compare the effects of the stapled peptides, Peptides **3.1-3.4** and their linear counterpart were evaluated for their ability to block inflammation in a RANTES ELISA at a single concentration of 50 nM, which was determined from a dose response of Peptide **3.1** (data not shown). All of the stapled peptides were observed to block the RANTES expression more effectively following stimulation with PAM3CSK4 than the linear peptide, which was not found to block the cytokine's expression at all.

RHAMM functional peptides have been developed and successfully been shown to block cellular functions based on the HA-RHAMM interaction, and have therapeutic effects in a number of processes, including inflammation, wound repair, and adipogenesis, without conferring any observable negative toxicities in the injected tissues [31, 46], suggesting that other RHAMM peptide mimetics have a wide range of potential therapeutic applications. Moreover, RHAMM R3 vaccines have already been tested in Phase I/II clinical trials [47, 48], offering promise that other RHAMM-based therapeutics can be developed and safely translated to a clinical setting.

Table 3.4. Inhibition of RANTES expression (compared to +PAM3CSK4 positive control) was observed in response to a number of peptide variants (50 nM dose).

Peptide ID	Inhibition (at 50 nM)
Linear	0%
3.1	27%
3.2	11%
3.3	10%
3.4	0%

3.2.4 Cyclization improves peptide stability

Peptide stability was evaluated by monitoring the degradation of the compounds following incubation in human serum. In addition to improving helicity, peptide stapling increases the diameter of the compound so that it exceeds that of the protease active site, and reduces exposure of the vulnerable amide backbone to protease cleavage [37, 49]. Thus, we expected that the stapled peptides would have improved resistance to enzymatic breakdown than their linear counterpart. In a similar fashion, N-terminal acetylation and carboxyamidation increase a peptide’s resistance to enzymatic breakdown, and specifically hinders the actions of exopeptidases and endoproteases [50]. As expected, the linear peptide degraded at a much faster rate than all of the cyclized variants, with degradation occurring immediately after incubation in serum began (**Figure 3.5**). Interestingly, all of the stapled peptides were still >80% intact after 6 hours of incubation, while the linear peptide had only 11% of the peptide remaining. The most notable degradation product in all of the stapled peptides, particularly after 24 hours of incubation, correlated with the loss of the first three N-terminal residues of the peptide sequence, KIK. No other cleavage products were observed, suggesting that the remainder of the peptide remains intact over the 24-hour incubation period. The residues being cleaved belong to the first HABD (HABD1) of the RHAMM protein (mRHAMM 721-750), which has predicted by computational modeling to be less important for HA binding [35]. The first HABD comprises fewer leucine and glutamine residues in its primary sequence than that of the second HABD, and these amino acids have been proposed to have a greater propensity to form an alpha-helix, making them helix-inducing and stabilizing residues [51]. With fewer helix-stabilizing residues in its sequence, HABD1 may not only have less helical character than HABD2, but may also contribute less to the overall stability of the compound, and therefore, be more likely to produce degradation products following incubation in serum.

Table 3.5. Peptide stability in 25% human serum at 6 hours and 24 hours

Peptide ID	**Percent remaining after 6 hours**	**Percent remaining after 24 hours**
Linear	11.4 ± 3.3	0.3 ± 0.1
3.1	82.3 ± 6.8	4.7 ± 0.7
3.2	91.7 ± 7.4	1.9 ± 0.1
3.3	86.5 ± 4.1	23.1 ± 0.1
3.4	66.6 ± 6.3	4.2 ± 2.1

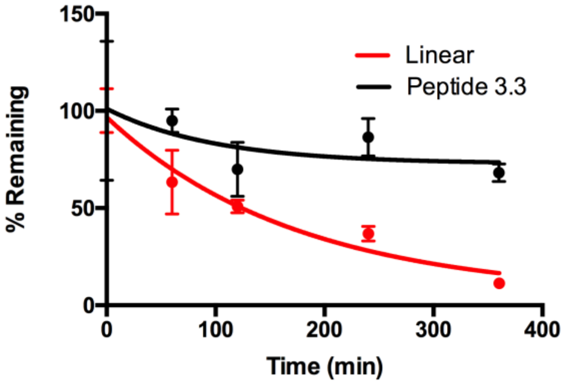

Figure 3.5. Stapling the peptide backbone (black) increases the half-life in human serum compared to the linear (red). Data was fit to nonlinear regression curves.

3.2.5 Modifying the lead compound to find a metabolically stable compound with strong binding affinity

The effect of altering the rigidity of the linker region was evaluated by removing the adjacent double staple. If two adjacent staples confer rigidity, removing one, or inserting a linker to separate them should increase the flexibility of the region, and therefore, destabilize the helical structure. Peptide **3.1** was used as a model for determining the effect of specific modifications to the structure and sequence on helicity and binding affinity. We evaluated the effect of removing the three N-terminal residues, KIK, which were observed as cleavage products following incubation in serum (Peptide **3.1-KIK**), as well as that of destabilizing the linker region between the two HABDs. In addition, we studied the effect following staple separation by one residue (**3.1+Gly**), two residues (**3.1+GG**), helix-inducing residues (**3.1+AA**), a hydrophobic residue, N-aminomethyl benzoic acid (amb) (**3.1+amb**), and the isolation of one of the staples, either the first staple (**3.1_1st staple**) or the second staple (**3.1_2nd staple**).

Table 3.6. Modifications to the linker region of Peptide 3.1. (*Peptides named based on IUPAC-IUB Joint Commission on Bicohemical Nomenclature [52], but reference ID will be used for ease of reference.)

Peptide ID	**Reference ID***	**Sequence**
3.1	3.1	Ac-KIKHVVKLK **[EENSK]-[EKSEK]** SKLRSQLVKRK-NH_2
des-(K1-K3)-Peptide 3.1	3.1-KIK	Ac-HVVKLK **[EENSK]-[EKSEK]** SKLRSQLVKRK-NH_2
[Leu^{16},Val^{20}]-Peptide 3.1	3.1_1st staple	Ac-KIKHVVKLK [**E**ENS**K**]-**L**KSE**V** SKLRSQLVKRK-NH_2
[Asp^{10},Lys^{14}]-Peptide 3.1	3.1_2nd staple	Ac-KIKHVVKLK **D**ENS**Q**-[**E**KSE**K**] SKLRSQLVKRK-NH_2
endo-Gly^{15a}-Peptide 3.1	3.1+Gly	Ac-KIKHVVKLK [**E**ENS**K**]-Gly-[**E**KSE**K**] SKLRSQLVKRK-NH_2
endo-Amb^{15a}-Peptide 3.1	3.1+Amb	Ac-KIKHVVKLK [**E**ENS**K**]-Amb-[**E**KSE**K**] SKLRSQLVKRK-NH_2
endo-Gly^{15a}, Gly^{15b}-Peptide 3.1	3.1+GG	Ac-KIKHVVKLK [**E**ENS**K**]-G-G-[**E**KSE**K**] SKLRSQLVKRK-NH_2
endo-Ala^{15a}, Ala^{15b}-Peptide 3.1	3.1+AA	Ac-KIKHVVKLK [**E**ENS**K**]-A-A-[**E**KSE**K**] SKLRSQLVKRK-NH_2
des-(K1-K3)-endo-Ala^{15a}, Ala^{15b}-Peptide 3.1	3.1-KIK+AA	Ac-HVVKLK [**E**ENS**K**]-A-A-[**E**KSE**K**] SKLRSQLVKRK-NH_2

We observed a significant difference in secondary structure in the modified 3.1-series peptides in a solution without the secondary structure-stabilizing solvent, TFE. In the cases of **3.1_1st staple**, **3.1+Amb**, **3.1+Gly**, and **3.1+GG**, the peptides not only lost some of their helical character, but may have even started to gain random coil character. Peptide **3.1_2nd staple** has greater alpha-helical character compared to those that appear to have random coil properties. This is particularly interesting when compared with **3.1_1st staple**, as the stark difference in helicity between the two peptides is attributed to the position of the staple. In **3.1_1st staple**, the staple is placed adjacent to the first HABD, while in **3.1_2nd staple**, the staple is placed adjacent to the second HABD, which has been reported to have greater helical character than the first, as well as play a greater role in HA binding than the first based on computational modeling [35] and site mutagenesis analysis [19]. This is further supported by the similar helicities observed between Peptide **3.1** and Peptide **3.1-KIK**, in which three residues were removed from HABD1, suggesting that the entirety of HABD1 does not contribute to RHAMM's overall helicity, and therefore, potentially does not bind to HA.

Table 3.7. Mean residue ellipticities of 3.1-series peptides

Peptide ID	**Water** $[\theta]_{222}/[\theta]_{208}$	**Water + 40% TFE** $[\theta]_{222}/[\theta]_{208}$
3.1	0.65	0.85
3.1-KIK	0.64	0.88
3.1_1st staple	0.35	0.88
3.1_2nd staple	0.58	0.84
3.1+Gly	0.39	0.81
3.1+Amb	0.42	0.80
3.1+GG	0.43	0.82
3.1+AA	0.70	0.90
3.1-KIK+AA	0.67	0.90

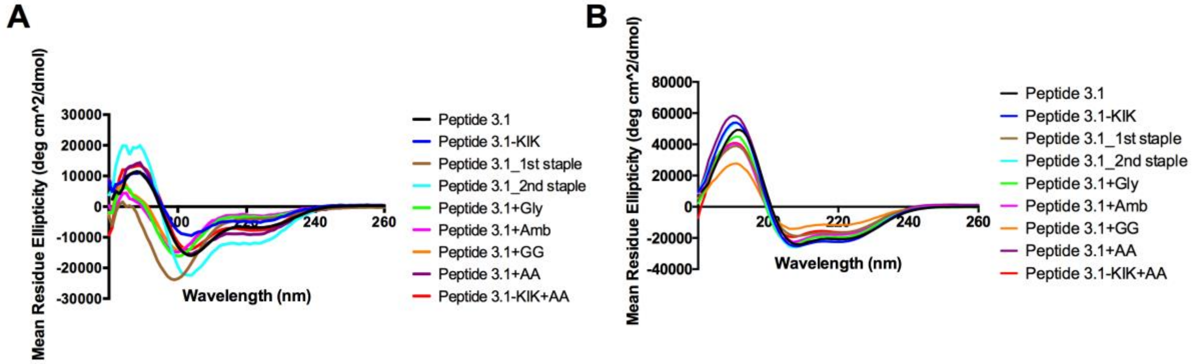

Figure 3.6. Modifications to lead compound, Peptide 3.1, affect helicity of peptides in water (A) by circular dichroism spectroscopy. Despite the modification, peptides all exhibit similar helical character in 40% TFE solution (B).

It has been proposed that the regions surrounding the HABDs of RHAMM facilitate the stabilization of the protein's secondary structure by their inward positioning that forms a hydrophobic core [35]. Interestingly, the introduction of a hydrophobic residue (n-methylaminobenzoic acid) into the sequence of this relatively hydrophilic peptide has the greatest negative effect on binding (**Table 3.8**, **Figure 3.7**). It is possible that rather than forming a hydrophobic core, separating the staples by one hydrophobic residue has a destabilizing effect on the peptide's helicity, by increasing the flexibility of the sequence so that the peptide adopts random coil properties, which would have detrimental effects on the HA binding properties of the peptide. In a similar manner, a single glycine residue between the two staples acts to destabilize the peptide, decreasing the peptide's helicity. This is immediately juxtaposed by a moderate increase in helicity when the staples are separated by two glycine residues (0.39 to 0.43 in water). The addition of two residues allow for the staples to be spaced closer to 3.6 amino acids apart from one another, facilitating helicity within the peptide backbone. The greatest improvement in helicity was observed when two alanine residues were added to the sequence (Peptide **3.1+AA**). Alanine has helix-inducing potential and stabilizes helices more than glycine by having a greater contribution to the hydrophobic effect than glycine as well as having a lower conformational entropy upon folding [53-55]. In the unfolded state, the backbone polar area of alanine is approximately 20.6 Å lower than that of glycine [53]. Alanine is especially stabilizing when it is positioned in internal helical positions [53]. Therefore, two alanine residues act to elongate the helices that are formed by the two staples by the spacing that it confers, and its helix-inducing properties. Interestingly, there is negligible change in helicity with the loss of the three N-terminal amino acids, but the additional of the alanine spacer between the staples more than compensates for the loss of amino acids by improving helical stability and secondary structure.

Table 3.8. Kinetic analysis of 3.1-series peptides

Peptide ID	**k_a (10^4/(M*s))**	**k_d (10^3/s)**	**K_D (nM)**
3.1	5.3 ± 0.5	4.7 ± 0.9	88.2 ± 2.5
3.1-KIK	23.5 ± 1.3	1.00 ± 0.2	117.4 ± 8.4
3.1_1st staple	60.6 ± 3.3	7.9 ± 0.5	479.8 ± 15.3
3.1_2nd staple	8.0 ± 1.0	2.3 ± 0.1	346.4 ± 10.3
3.1+Gly	12.2 ± 0.5	4.9 ± 0.2	381.1 ± 4.5
3.1+Amb	17.9 ± 2.4	4.0 ± 0.3	553.6 ± 13.1
3.1+GG	3.3 ± 0.5	4.5 ± 0.5	168.4 ± 9.8
3.1+AA	25.9 ± 1.2	2.5 ± 0.3	84.7 ± 5.4
3.1-KIK+AA	9.8 ± 1.0	6.2 ± 0.5	89.3 ± 7.2

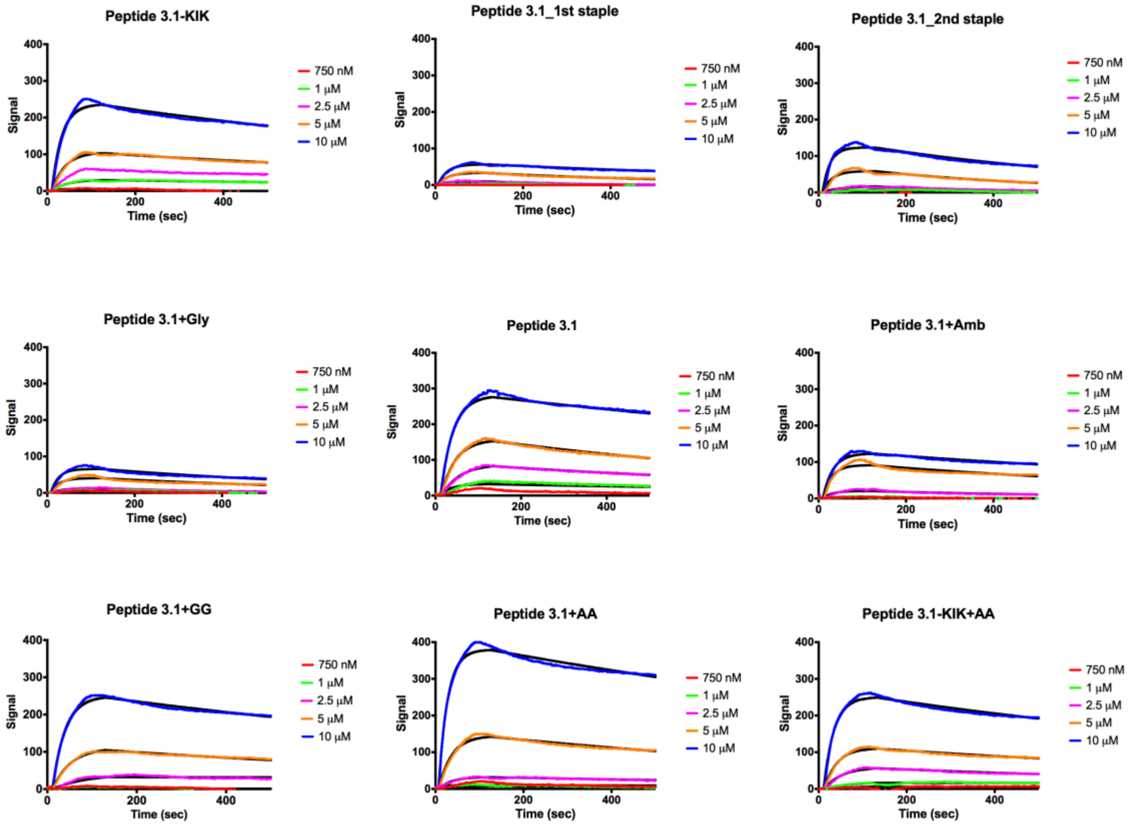

Figure 3.7. SPR experiments between modified variants of Peptide 3.1 and 5-10 kDa HA. Each signal corresponds to the responses of 5 peptide concentrations (750 nM, 1 µM, 2.5 µM, 5 µM, and 10 µM). The solid lines indicate a global 1:1 interaction curve fitting model for each of the interactions.

We observed a relationship between secondary structure stability and the binding potential of the 3.1-series peptides. This supports past reports in which secondary structure has been described as being important in order for binding to occur between HA and RHAMM [34, 35]. As expected, destabilising the linker region of Peptide **3.1** results in weaker binding to HA than the lead compound, regardless of whether only one of the two staples was present, or if a spacer was inserted between the two staples. Separating the two staples with a spacer, such as with a glycine residue or a N-methylamino benzoic acid residue, resulted in slightly improved affinity for HA than when only one of the two staples was present. The dissociation rate constants also increased, indicating a decrease in specificity of the RHAMM peptide mimetics for HA. This finding suggests that there may be a need for the increased stability in the linker region that is conferred through the incorporation of two staples rather than a single one. The exceptions to this, however, are Peptides **3.1+AA** and **3.1-KIK+AA**, which have very similar affinities to the lead compound. This highlights the importance of alpha-helical character in RHAMM, which is induced by additional Ala residues, on its ability to bind to HA. Interestingly, the loss of 3 residues from HABD1 (**3.1-KIK**) results in a negligible decrease in affinity compared to Peptide **3.1**, but this is negated in Peptide **3.1-KIK+AA** when two alanine residues are placed between the two staples, and the binding remains the same. Thus, Peptide 3.1-KIK+AA yields a compound with superior stability and almost identical affinity for HA, making it a drug candidate with high potential for treating diseases ensuing from the RHAMM-HA interaction.

3.3 Conclusion

Here, we described the development of the first RHAMM-based drug prototype for interfering with HA-RHAMM interactions. Alpha-helicity is an inherent property of the RHAMM protein, which facilitates binding to its ligand, hyaluronan, and its endogenous activity. The RHAMM peptide mimetics described here were cyclized by two (i, i+4) lactam bridge staples placed in the linker region between the two HABDs in order to improve helicity, HA binding, and bioactivity both in culture and *in vivo* over the linear compound. One lead compound, Peptide **3.1**, was identified from a structure activity relationship analysis, and was validated for the ability to block inflammation in culture and *in vivo*. From this compound, the sequence was successfully optimized in order to create a metabolically stable peptide with strong affinity for its target that can be further investigated as a prototypical drug molecule.

3.4 Methods

3.4.1 General Methods

All Fmoc-protected amino acids were obtained from ChemImpex. HCTU, HATU, and Rink Amide MBHA resin (4-(2’,4’-dimethoxyphenyl-(9-fluorenylmethoxycarbonyl)-aminomethyl)-phenoxy-acetamidonorleucyl-4-methyl benzhydrylamine resin) were obtained from ChemImpex. Tetrakis(triphenylphosphine)palladium (0), phenylsilane, and Fmoc-AEEA-OH spacer were obtained from Sigma-Aldrich. All solvents were obtained from Fisher Thermo-Scientific.

3.4.2 Synthesis of peptides

All peptides were synthesized by applying fluorenyl-9-methoxycarbonyl (Fmoc) solid phase peptide synthesis. Synthesis was conducted on a 0.1 mmol scale using Rink amide MBHA (0.39 mmol/g), with a four-fold excess of Fmoc protected L-amino acids. Amino acids were coupled with HCTU (4 eq.) in DMF and DIPEA (6 eq.). All coupling reactions were carried out at room temperature for 45 minutes with vortexing. The Fmoc group was removed using 2 treatments of 20% piperidine/DMF for 15-minute and 5-minute periods. Following synthesis, the resin was washed with dichloromethane. Cleavage of the peptide was carried out by treating the resin with TFA: water: triisopropylsilane (95:2.5:2.5 v/v) for 5 hours. The cleaved peptide was then precipitated with cold TBME, and was then pelleted by centrifugation at 3000 rpm for 10 min. After decanting the supernatant, the peptide pellet was rinsed with TBME, resuspended by vortexing, and centrifuged again. The ensuing peptide pellet was dissolved in water, frozen and lyophilized until a dry, solid powder was obtained.

Purification was carried out using a reversed-phase preparative HPLC column (Agilent Zorbax SB-C18 column 21.2 x 150 mm, 5μm) and analyzed on a reversed-phased analytical HPLC column (Agilent Zorbax SB-C18 column 4.6 x 150 mm, 3.5 μm). This system was outfitted with a Waters 600 136 controller, Waters Prep degasser, and Waters MassLynx software (version4.1). The mobile phases employed were 0.1% TFA in water (solvent A) and 0.1% TFA in acetonitrile (solvent B). The flow rate for the preparative HPLC was set at 20 mL/min and with a flow rate of 1.5 mL/min over 15 minutes for the analytical system. The absorbance was monitored using a Waters 2998 Photodiode array detector set at 220 nm, 254 nm, and 400 nm. The collected fractions were then lyophilized to a solid, and subsequently analyzed by analytical RP-HPLC (220 nm).

All peptides were purified by the above-mentioned protocol at a gradient of 20% to 35% with a retention time of 9-10 minutes.

3.4.3 Lactam bridge formation

Double-staple containing peptides were synthesized by Fmoc-based SPPS. Each staple was synthesized separately; the peptide was synthesized from its C-terminus to the N-terminus of the first lactam bridge, followed by selective deprotection of the orthogonal protecting groups (allyloxycarbonyl and allylester) on the side chains of the residues creating the staple. The two side chains were coupled with the N-terminal Fmoc group still in place. The remainder of the peptide was then synthesized and the second staple was formed as before.

Allyloxycarbonyl and the allylester protecting groups on the lysine and glutamic acid groups, respectively, were deprotected with phenylsilane (24 eq) in DCM to the resin-bound peptide, flushing with nitrogen, and shaking for 5 minutes. Tetrakis(triphenylphosphine) palladium (0) (0.1 eq) was then added to the mixture and the peptide vessel was again flushed with nitrogen. This reaction was allowed to proceed for 10 minutes. The resin was subsequently washed with DCM (4 x 30 s), followed by a series of washings with DCM, DMF, MeOH, DMF, DCM (30 s each). Cyclization was carried out with HATU (3 eq) and DIPEA (6 eq) in DMF for a minimum of 2 hours. Following successful cyclization, the N-terminal Fmoc group was deprotected with 20% piperidine/DMF for 15 minutes. The peptide was acetylated with 2 treatments of 20% acetic anhydride/DMF for 30 minutes each.

3.4.4 Circular Dichroism spectroscopy

CD was carried out on a Jasco J-810 spectropolarimeter and recorded in the range of 180-260 nm. The peptides were dissolved in Milli-Q water, and in a 40% TFE/water solution at a concentration of 0.25 mg/mL. The measurements were carried out at $20^{O}C$, using a quartz cuvette with a path length of 1mm. The instrument measured at a scanning speed of 10-50 nm/min, and averaged five individual data points in order to obtain the reported CD spectrum. A blank solution of Milli-Q water, and 40% TFE/water were run before the measurements, and the spectra were baseline corrected.

3.4.5 Synthesis of HA-Cystamine

5-10 kDa HA (purchased as sodium hyaluronate, Lifecore Biomedical) was dissolved in DMSO/H_2O (7/3, v/v), and was reacted with excess sodium cyanoborohydride for 12 hours at room temperature. 10 equivalents of cysteamine hydrochloride (Sigma Aldrich) was added, and the reaction proceeded for an additional 24 hours. The solution was then dialyzed exhaustively in deionized water for 3 days using a 3.5-5 kDa dialysis tube (Float-a-Lyzer, Spectrum Labs) with a biotech grade cellulose ester membrane.

3.4.6 HA binding

All experiments were carried out on an OpenSPR^{TM} instrument (Nicoya Lifesciences) at 25°C, equipped with a 100 µL loading loop. Gold nanoparticle (100 nm) biosensors were purchased from Nicoya Lifesciences. All experiments were carried out in phosphate buffered saline (PBS) running buffer (137 mM NaCl, 2.7 mM KCl, 10 mM Na_2HPO_4, 2 mM KH_2PO_4), pH 7.4. The gold biosensors were incubated with cystamine-functionalized 5-10 kDa HA (3mg/mL) for 3 days. Available binding sites on the chip surface were blocked with poly (ethylene glycol) methyl ether thiol (2 mg/mL) (Sigma Aldrich). The peptide ligands were dissolved in PBS at varying concentrations, and were injected at a flow rate of 50 µL/min when the baseline was stabilized. Regeneration of the chip surface was carried out with 1 M NaCl, and no further injections were done until the baseline was stable. The data was processed and analyzed using Tracedrawer software (Ridgeview Instruments AB). Kinetic parameters were calculated using a global analysis, fitting the data to a 1:1 model.

3.4.7 Serum stability

Each peptide (1 mM final concentration) was incubated in a mixture of 25% human serum (Sigma-Aldrich, Male type AB cat# H4522) in PBS (pH 7.4, 450 µL final volume, DMSO final concentration 0.5%) at 37 °C. At appropriate time intervals, aliquots of peptide solution were removed and mixed with either acidic solutions (4% phosphoric acid, pH 1-2) or basic (4% ammonium hydroxide, pH 11-13) to dissociate peptide interactions with components of human serum. Peptide was isolated from human serum by column separation on Oasis® sorbent 96-well µElution plates (HLB- amphiphilic resin and MCX-cation exchange resin) and manifold. The extracted peptide was quantified on an Acquity UHPLC-MS system (Waters Co.). Peptide was quantified by measuring the peak area of a peptide specific M^{+n} ion peak (average of 3 replicates). Percent abundance of peptide peak area relative to peptide peak abundance at T0 was plotted as a function of time. Peptide half-life was calculated by optimized curve fitting (linear, 2-parameter or 3-parameter exponential decay curve) on SigmaPlot™ and solving for time at 50% peptide peak abundance.

3.4.8 Inflammation protein array

Commercially available murine RAW 264.7 macrophages carrying a SEAP reporter gene (RAW-Blue; InvivoGen, San Diego, CA, USA) were used. Cells were grown to 80% confluence in DMEM containing 4.5 g/L glucose, 10% heat-inactivated fetal bovine serum, 2 mM L-glutamine, 50 µg/mL penicillin/streptomycin, 100 µg/mL Normocin (InvivoGen) at 37 °C in 5% CO_2.

For peptide screening experiments, cells were scraped in growth medium, counted, and plated to flat-bottom 96-well plates at a density of $5x10^4$cells/well either in the presence or absence (control) of 200 ng/mL TLR1/TLR2 agonist PAM3CSK4 (InvivoGen). RHAMM peptides were added in 6 replicate wells at a dose of 10ng/mL in the presence of PAM3CSK4. After 18 hours of stimulation, reverse phase protein microarray membrane was incubated in the supernatants collected from the RAW-Blue cells. After 20 minutes of incubation at 37 °C, a general secondary antibody was washed over the membrane, and the SEAP levels were determined using spectrophotometry at a wavelength of 630 nm.

3.4.9 RANTES ELISA

RANTES levels were also measured in the supernatants of stimulated RAW-Blue cells by sandwich ELISA (mouse Quantikine TNFα ELISA; R&D Systems, Minneapolis, MN, USA) following manufacturers protocol.

3.4.10 Lipopolysaccharide mouse assay

Peptide 3.1 was converted from its TFA salt form to the acetate salt with three incubations in a 25% acetic acid solution. It was dissolved in PBS buffer and was sterilized by filtration through a 0.22 μm filter. 5-week old C57BL/6 female mice (Charles River) were housed for one week prior, and were subsequently injected subcutaneously with Peptide 3.1 (9 mg/kg, 1.85 μM). A second dose of the same concentration of peptide was injected 18-20 hours after the first injection. Mice in the control group and LPS only group received an injection of PBS buffer instead of peptide. All mice were injected with buprenorphine (subcutaneous, 0.2mg/kg). Mice in the peptide treated and LPS only control groups were injected with LPS (intraperitoneal (IP), 5 mg/kg) 1 hour after the second peptide injection. The control group did not receive LPS. The mice were anesthetized by isoflurane inhalation 30 minutes after the LPS injection, and blood was drawn by cardiac puncture. The serum was isolated by centrifugation at 4 °C for 10 min at 13 000 RPM. An ELISA was carried out to quantify serum concentration of TNF-α.

3.5 References

1. Laurent, T.C. and Fraser, J., *Hyaluronan.* FASEB J, 1992. **6**(7): p. 2397-2404.

2. Kavasi, R.M., et al., *HA metabolism in skin homeostasis and inflammatory disease.* Food Chem Toxicol, 2017. **101**: p. 128-138.

3. Schiraldi, C., et al., *Hyaluronan viscosupplementation: state of the art and insight into the novel cooperative hybrid complexes based on high and low molecular weight HA of potential interest in osteoarthritis treatment.* Clin Cases Miner Bone Metab, 2016. **13**(1): p. 36-37.

4. Litwiniuk, M., et al., *Hyaluronic Acid in Inflammation and Tissue Regeneration.* Wounds, 2016. **28**(3): p. 78-88.

5. Lauer, M.E., et al., *The Rise and Fall of Hyaluronan in Respiratory Diseases.* Int J Cell Biol, 2015. **2015**: p. 712507.

6. Hull, R.L., et al., *Hyaluronan: A Mediator of Islet Dysfunction and Destruction in Diabetes?* J Histochem Cytochem, 2015. **63**(8): p. 592-603.

7. Misra, S., et al., *Interactions between Hyaluronan and Its Receptors (CD44, RHAMM) Regulate the Activities of Inflammation and Cancer.* Front Immunol, 2015. **6**: p. 201.

8. Schwertfeger, K.L., et al., *Hyaluronan, Inflammation, and Breast Cancer Progression.* Front Immunol, 2015. **6**: p. 236.

9. Stern, R., Asari, A.A., and Sugahara, K.N., *Hyaluronan fragments: An information-rich system.* Eur J Cell Biol 2006. **85**(8): p. 699-715.

10. Nikitovic, D., et al., *Could growth factor-mediated extracellular matrix deposition and degradation offer the ground for directed pharmacological targeting in fibrosarcoma?* Curr Med Chem, 2013. **20**(23): p. 2868-2880.

11. Heldin, P., et al., *Deregulation of hyaluronan synthesis, degradation and binding promotes breast cancer.* J Biochem, 2013. **154**(5): p. 395-408.

12. Stern, R. and Maibach, H.I., *Hyaluronan in skin: aspects of aging and its pharmacologic modulation.* Clin Dermatol, 2008. **26**(2): p. 106-122.

13. Scheibner, K.A., et al., *Hyaluronan fragments act as an endogenous danger signal by engaging TLR2.* J Immunol, 2006. **177**(2): p. 1272-1281.

14. Toole, B.P., *Hyaluronan: from extracellular glue to pericellular cue.* Nat Rev Cancer, 2004. **4**(7): p. 528-539.

15. Khaldoyanidi, S.K., et al., *Hyaluronan in the healthy and malignant hematopoietic microenvironment.* Adv Cancer Res, 2014. **123**: p. 149-189.

16. Kouvidi, K., et al., *Hyaluronan/RHAMM interactions in mesenchymal tumor pathogenesis: role of growth factors.* Adv Cancer Res, 2014. **123**: p. 319-349.

17. Lee-Sayer, S.S., et al., *The where, when, how, and why of hyaluronan binding by immune cells.* Front Immunol, 2015. **6**: p. 150.

18. Higman, V.A., et al., *A Refined Model for the TSG-6 Link Module in Complex with Hyaluronan: use of defined oligosaccharides to probe structure and function.* J Biol Chem, 2014. **289**(9): p. 5619-5634.

19. Yang, B., et al., *Identification of a common hyaluronan binding motif in the hyaluronan binding proteins RHAMM, CD44 and link protein.* Embo j, 1994. **13**(2): p. 286-296.

20. Tolg, C., et al., *RHAMM promotes interphase microtubule instability and mitotic spindle integrity through MEK1/ERK1/2 activity.* J Biol Chem, 2010. **285**(34): p. 26461-26474.

21. Maxwell, C.A., et al., *RHAMM is a centrosomal protein that interacts with dynein and maintains spindle pole stability.* Mol Biol Cell, 2003. **14**(6): p. 2262-2276.

22. Shigeishi, H., et al., *Overexpression of the receptor for hyaluronan-mediated motility, correlates with expression of microtubule-associated protein in human oral squamous cell carcinomas.* Int J Oncol, 2009. **34**(6): p. 1565-1571.

23. Chen, H., et al., *Spatial regulation of Aurora A activity during mitotic spindle assembly requires RHAMM to correctly localize TPX2.* Cell Cycle, 2014. **13**(14): p. 2248-2261.

24. Maxwell, C.A., McCarthy, J., and Turley, E., *Cell-surface and mitotic-spindle RHAMM: moonlighting or dual oncogenic functions?* J Cell Sci, 2008. **121**(7): p. 925-932.

25. Tolg, C., et al., *Hyaluronan and RHAMM in wound repair and the "cancerization" of stromal tissues.* Biomed Res Int, 2014. **2014**: p. 103923.

26. Shepard, H.M., *Breaching the Castle Walls: Hyaluronan Depletion as a Therapeutic Approach to Cancer Therapy.* Front Oncol, 2015. **5**: p. 192.

27. Katona, E., et al., *PP2B and ERK1/2 regulate hyaluronan synthesis of HT168 and WM35 human melanoma cell lines.* Int J Oncol, 2016. **48**(3): p. 983-997.

28. Jiang, J., Mohan, P., and Maxwell, C.A., *The cytoskeletal protein RHAMM and ERK1/2 activity maintain the pluripotency of murine embryonic stem cells.* PLoS One, 2013. **8**(9): p. e73548.

29. Hatano, H., et al., *Overexpression of receptor for hyaluronan-mediated motility (RHAMM) in MC3T3-E1 cells induces proliferation and differentiation through phosphorylation of ERK1/2.* J Bone Miner Metab, 2012. **30**(3): p. 293-303.

30. Tolg, C., et al., *A RHAMM mimetic peptide blocks hyaluronan signaling and reduces inflammation and fibrogenesis in excisional skin wounds.* Am J Pathol, 2012. **181**(4): p. 1250-1270.

31. Bahrami, S.B., et al., *Receptor for hyaluronan mediated motility (RHAMM/HMMR) is a novel target for promoting subcutaneous adipogenesis.* Integr Biol, 2017. **9**(3): p. 223-237.

32. Gandhi, N.S. and Mancera, R.L., *The structure of glycosaminoglycans and their interactions with proteins.* Chem Biol Drug Des, 2008. **72**(6): p. 455-482.

33. Houston, M.E., et al., *Lactam bridge stabilization of α-helical peptides: Ring size, orientation and positional effects.* J Pept Sci, 1995. **1**(4): p. 274-282.

34. Yang, B., Zhang, L., and Turley, E.A., *Identification of two hyaluronan-binding domains in the hyaluronan receptor RHAMM.* J Biol Chem, 1993. **268**(12): p. 8617-8623.

35. Ziebell, M.R. and Prestwich, G.D., *Interactions of peptide mimics of hyaluronic acid with the receptor for hyaluronan mediated motility (RHAMM).* J Comp Aid Mol Des, 2004. **18**(10): p. 597-614.

36. Pelton, J.T. and McLean, L.R., *Spectroscopic methods for analysis of protein secondary structure.* Anal Biochem, 2000. **277**(2): p. 167-176.

37. Hill, T.A., et al., *Constraining cyclic peptides to mimic protein structure motifs.* Angew Chem, 2014. **53**(48): p. 13020-13041.

38. Oliveira, A.V., et al., *Evaluation of cystamine-modified hyaluronic acid/chitosan polyplex as retinal gene vector.* Mater Sci Eng C, 2016. **58**: p. 264-272.

39. Morera, D.S., et al., *Hyaluronic acid family in bladder cancer: potential prognostic biomarkers and therapeutic targets.* Br J Cancer, 2017. **117**(10): p. 1507-1517.

40. Collum, S.D., et al., *Inhibition of hyaluronan synthesis attenuates pulmonary hypertension associated with lung fibrosis.* Br J Pharmacol, 2017. **174**(19): p. 3284-3301.

41. Osterholt, H.C., et al., *Antioxidant protects against increases in low molecular weight hyaluronan and inflammation in asphyxiated newborn pigs resuscitated with 100% oxygen.* PLoS One, 2012. **7**(6): p. e38839.

42. Misra, S., et al., *Hyaluronan-CD44 interactions as potential targets for cancer therapy.* Febs J, 2011. **278**(9): p. 1429-1443.

43. Heldin, P., et al., *HAS2 and CD44 in breast tumorigenesis.* Adv Cancer Res, 2014. **123**: p. 211-229.

44. Esguerra, K.V., et al., *Identification, design and synthesis of tubulin-derived peptides as novel hyaluronan mimetic ligands for the receptor for hyaluronan-mediated motility (RHAMM/HMMR).* Integr Biol, 2015. **7**(12): p. 1547-1560.

45. Piotrowicz, R.S., et al., *A6 peptide activates CD44 adhesive activity, induces FAK and MEK phosphorylation, and inhibits the migration and metastasis of CD44-expressing cells.* Mol Cancer Ther, 2011. **10**(11): p. 2072-2082.

46. Turley, E.A., Wood, D.K., and McCarthy, J.B., *Carcinoma Cell Hyaluronan as a "Portable" Cancerized Prometastatic Microenvironment.* Cancer Res, 2016. **76**(9): p. 2507-2512.

47. Greiner, J., et al., *High-dose RHAMM-R3 peptide vaccination for patients with acute myeloid leukemia, myelodysplastic syndrome and multiple myeloma.* Haematologica, 2010. **95**(7): p. 1191-1197.

48. Schmitt, M., et al., *RHAMM-R3 peptide vaccination in patients with acute myeloid leukemia, myelodysplastic syndrome, and multiple myeloma elicits immunologic and clinical responses.* Blood, 2008. **111**(3): p. 1357-1365.

49. Schafmeister, C.E., Po, J., and Verdine, G.L., *An all-hydrocarbon cross-linking system for enhancing the helicity and metabolic stability of peptides.* J Am Chem Soc, 2000. **122**(24): p. 5891-5892.

50. Nguyen, L.T., et al., *Serum stabilities of short tryptophan-and arginine-rich antimicrobial peptide analogs.* PloS one, 2010. **5**(9): p. e12684.

51. Shepherd, N.E., et al., *Single turn peptide alpha helices with exceptional stability in water.* J Am Chem Soc, 2005. **127**(9): p. 2974-2983.

52. Gdr, H.B., Sharon, N., and Australia, E.W., Nomenclature and symbolism for aminoa cids and peptides. Eur J Biochem, 1984. **138**: p. 9-37.

53. Lopez-Llano, J., Campos, L.A., and Sancho, J., *Alpha-helix stabilization by alanine relative to glycine: roles of polar and apolar solvent exposures and of backbone entropy.* Proteins, 2006. **64**(3): p. 769-778.

54. Luque, I., Mayorga, O.L., and Freire, E., *Structure-based thermodynamic scale of α-helix propensities in amino acids.* Biochemistry, 1996. **35**(42): p. 13681-13688.

55. Serrano, L., et al., *Effect of alanine versus glycine in α-helices on protein stability.* Nature, 1992. **356**(6368): p. 453-455.

3.6 Supplemental Information

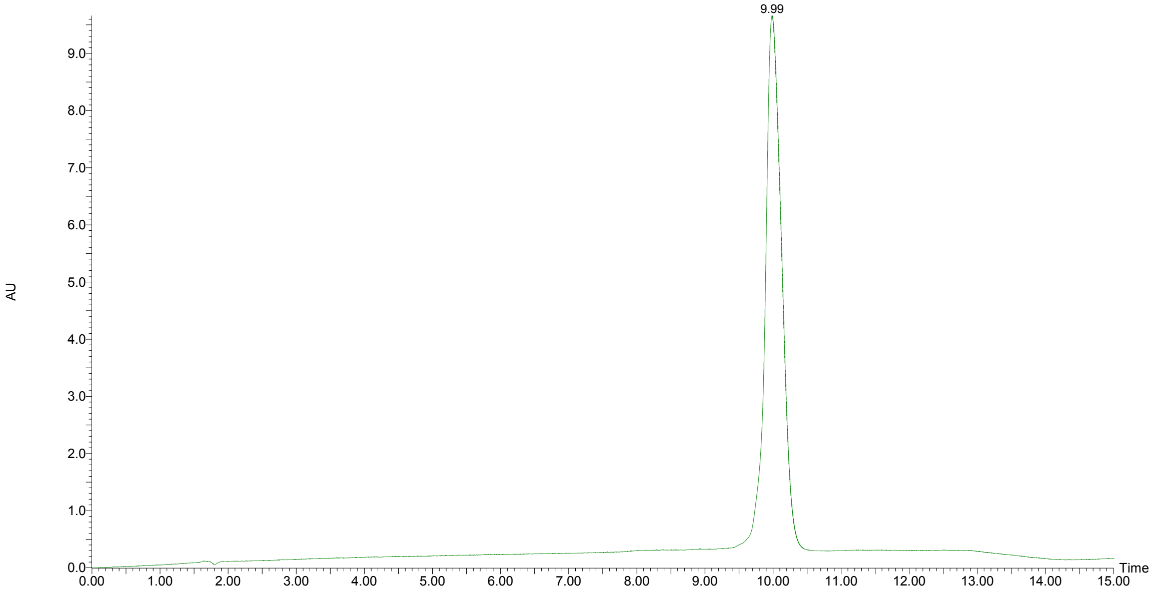

Figure S 3.1. HPLC trace of Linear peptide (Ac-KIKHVVKLKDENSQLKSEVSKL RSQLVKRK-NH$_2$)

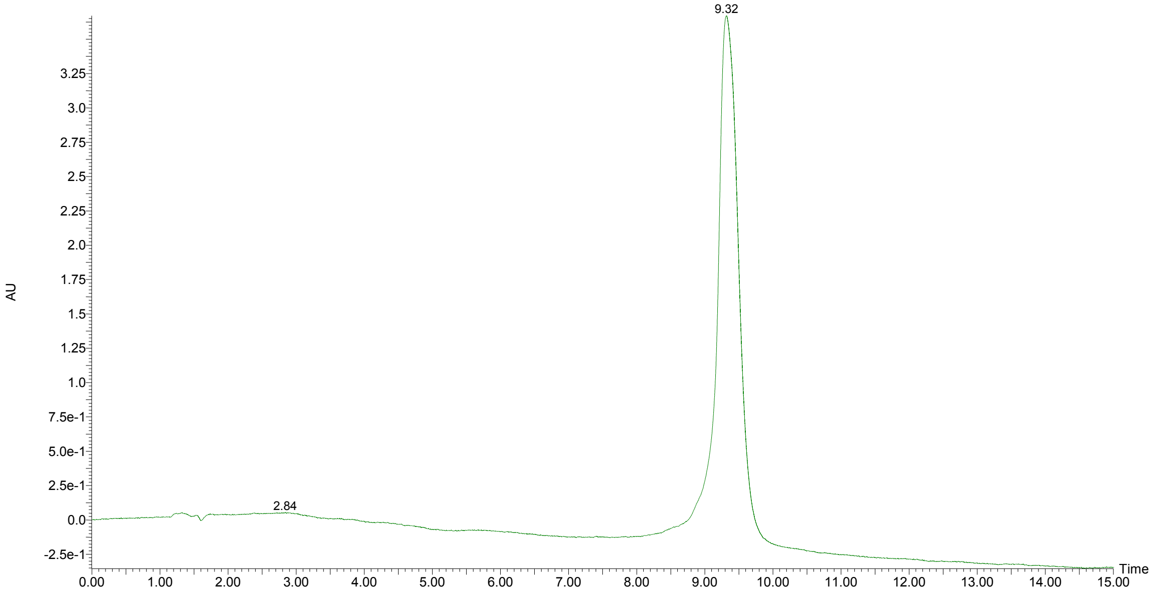

Figure S 3.2. HPLC trace of Peptide 3.1 (Ac-KIKHVVKLK [EENSK]-[EKSEK] SKLRSQLVKRK-NH$_2$)

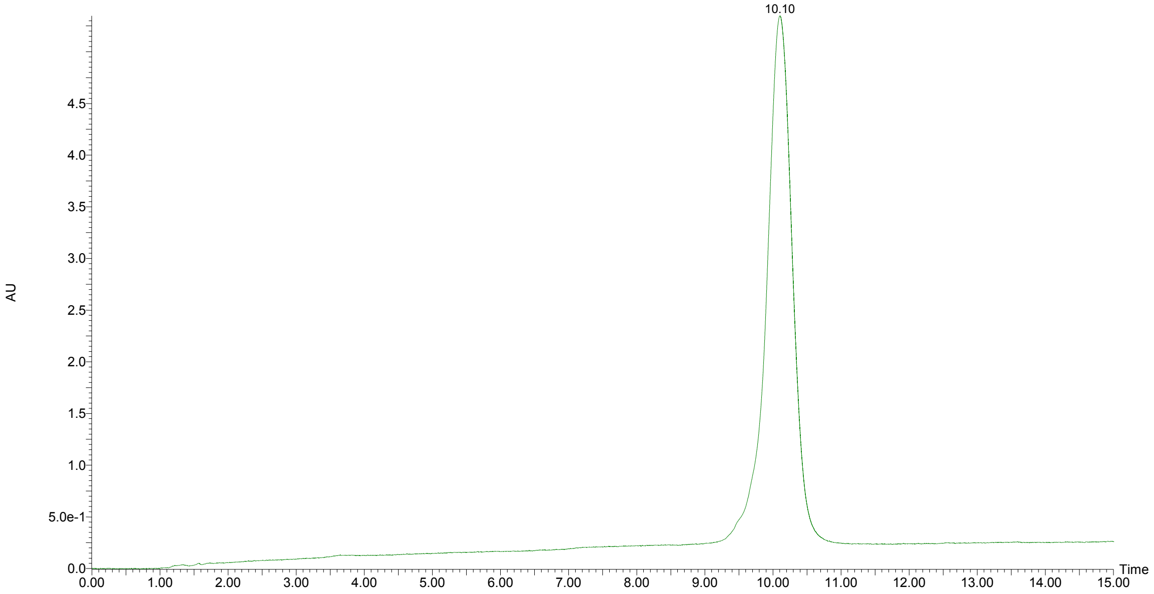

Figure S 3.3. HPLC trace of Peptide 3.2 (Ac-KIKHVVKLKD [ENSQK]-[ESEVK] KLRSQLVKRK-NH_2)

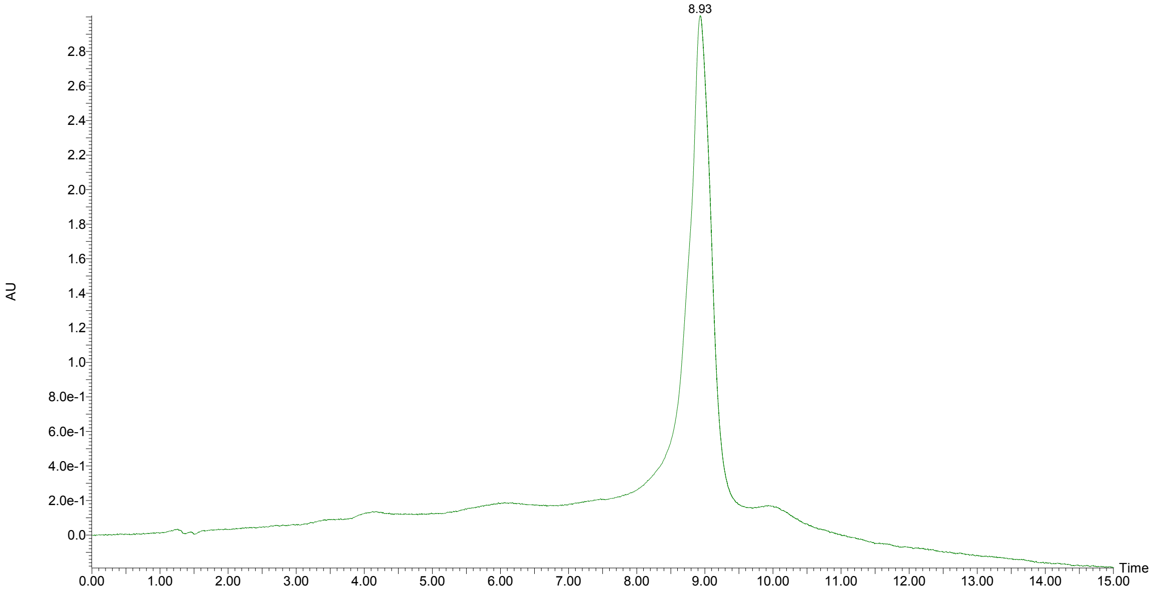

Figure S 3.4. HPLC trace of Peptide 3.3 (Ac-KIKHVVKLK [EENSK]-[KKSEE] SKLRSQLVKRK-NH_2)

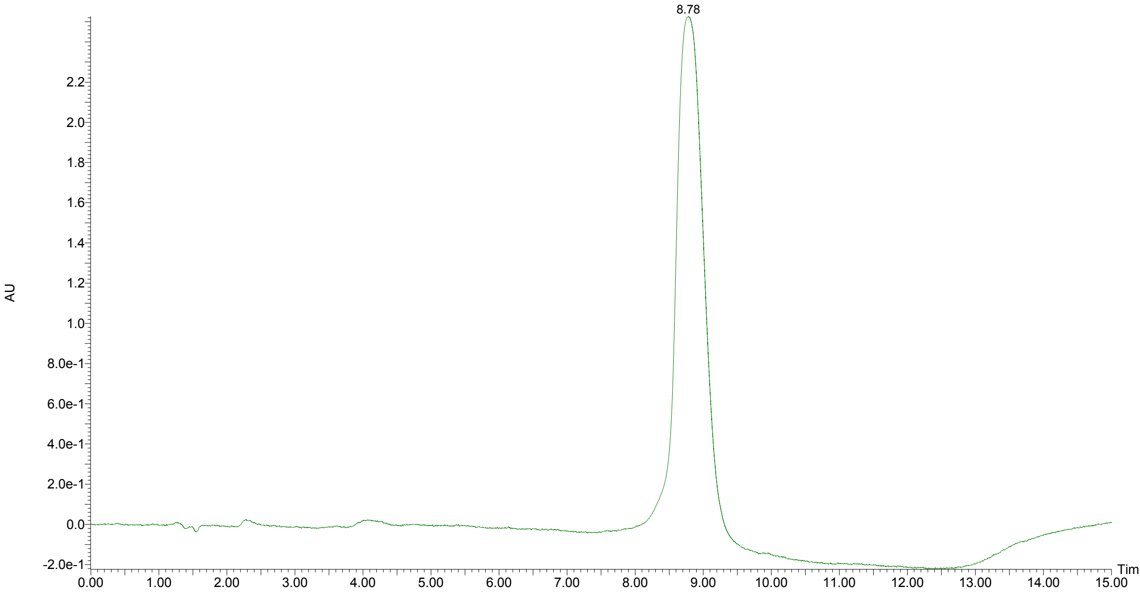

Figure S 3.5. HPLC trace of Peptide 3.4 (Ac-KIKHVVKLK[KENSE]-[EKSEK] SKLRSQLVKRK-NH$_2$)

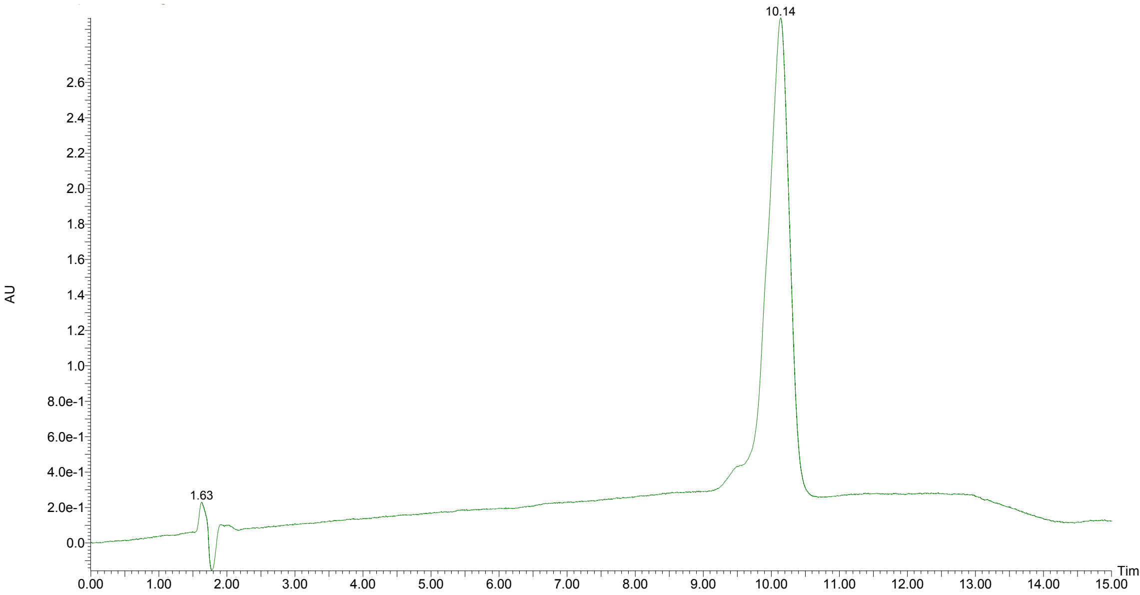

Figure S 3.6. HPLC trace of Peptide 3.1-KIK (Ac-HVVKLK [EENSK]-[EKSEK] SKLRSQLVKRK-NH$_2$)

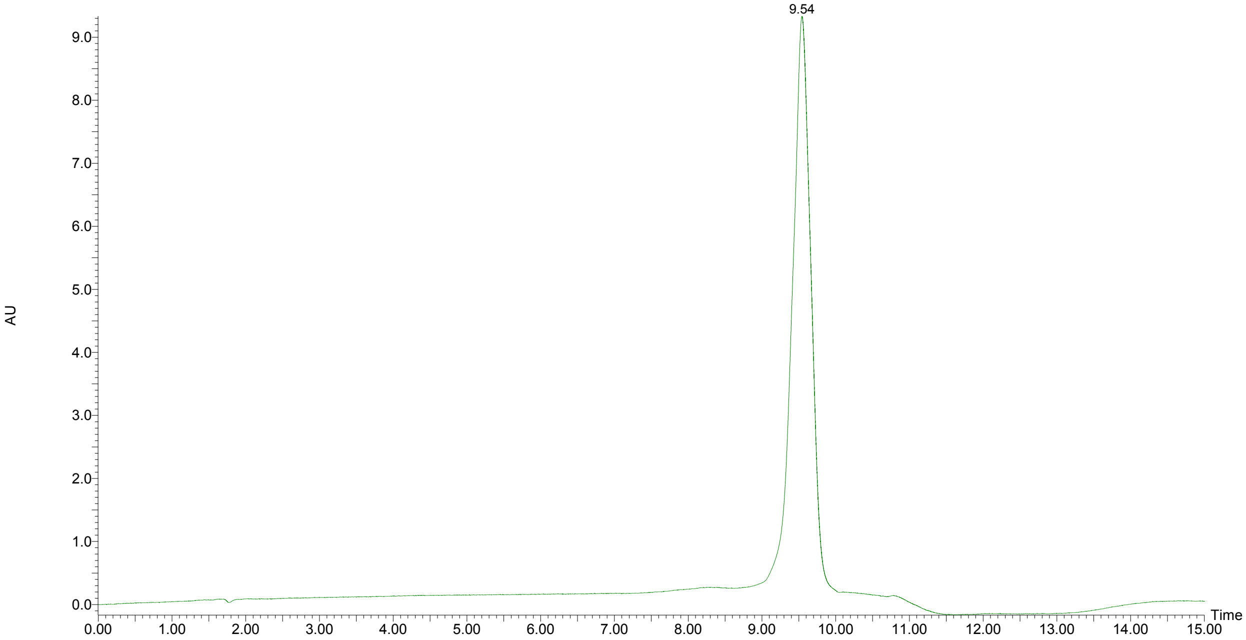

Figure S 3.7. HPLC trace of Peptide 3.1_1st staple (Ac-KIKHVVKLK [EENSK]-LKSEV SKLRSQLVKRK-NH$_2$)

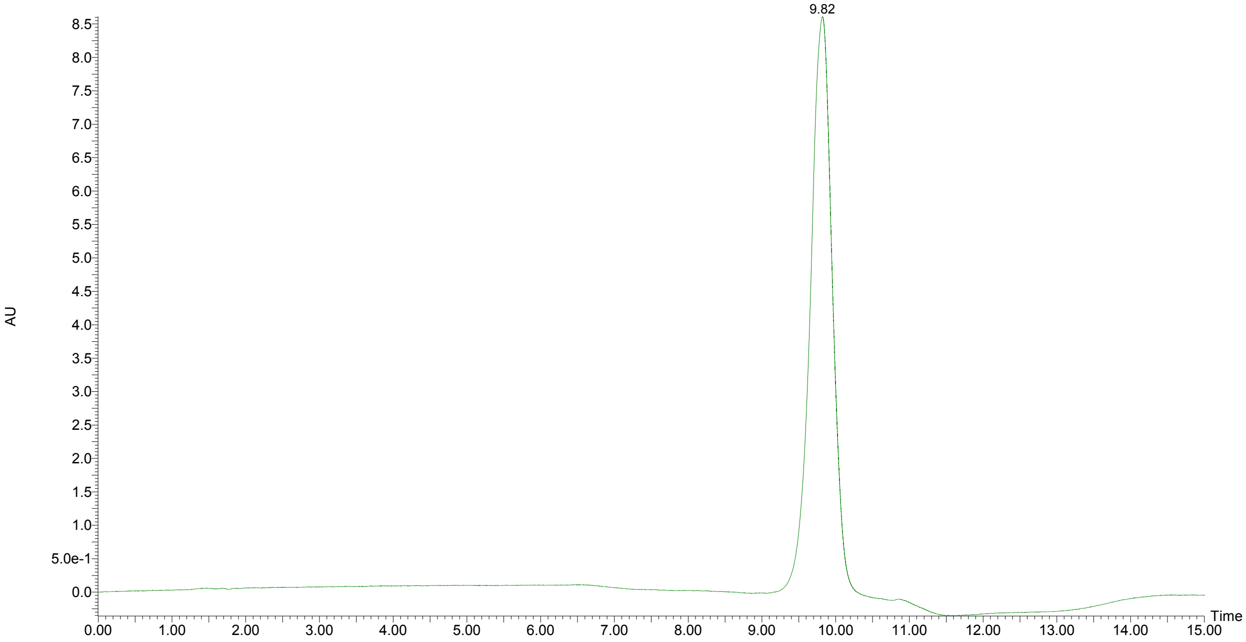

Figure S 3.8. HPLC trace of Peptide 3.1_2nd staple (Ac-KIKHVVKLK DENSQ-[EKSEK] SKLRSQLVKRK-NH$_2$)

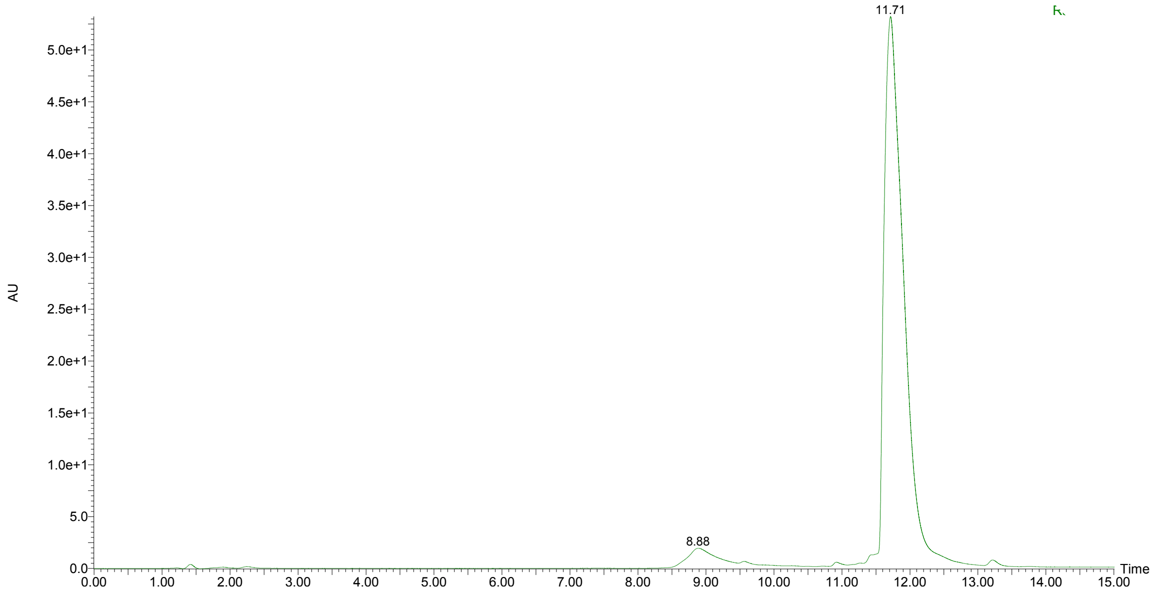

Figure S 3.9. HPLC trace of Peptide 3.1+Gly (Ac-KIKHVVKLK [EENSK]-Gly-[EKSEK] SKLRSQLVKRK-NH$_2$)

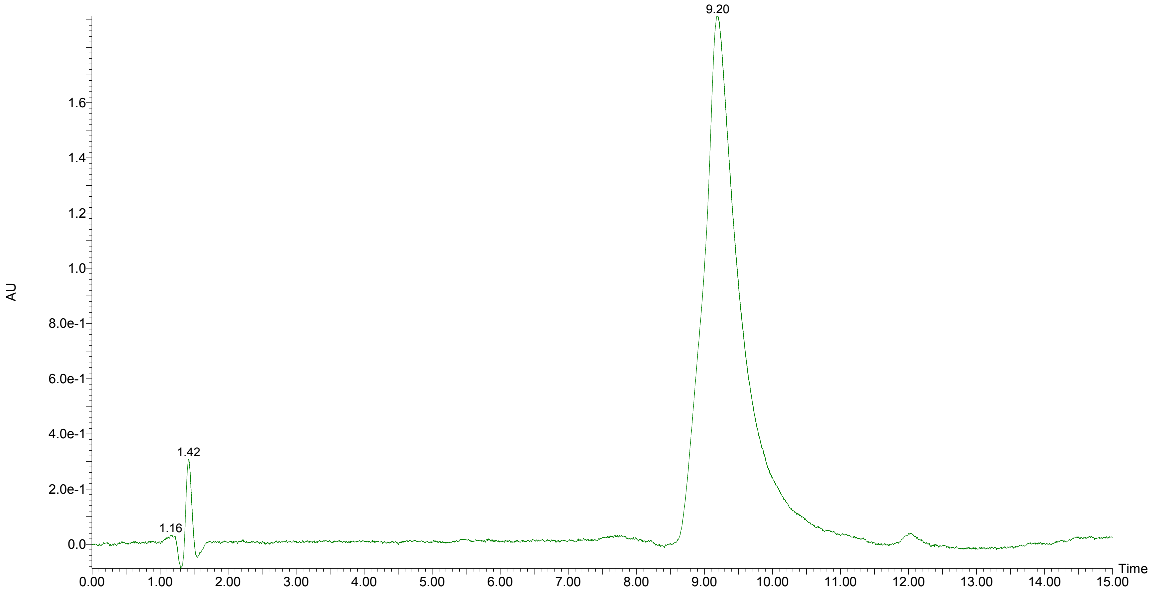

Figure S 3.10. HPLC trace of Peptide 3.1+Amb (Ac-KIKHVVKLK [EENSK]-Amb-[EKSEK] SKLRSQLVKRK-NH$_2$)

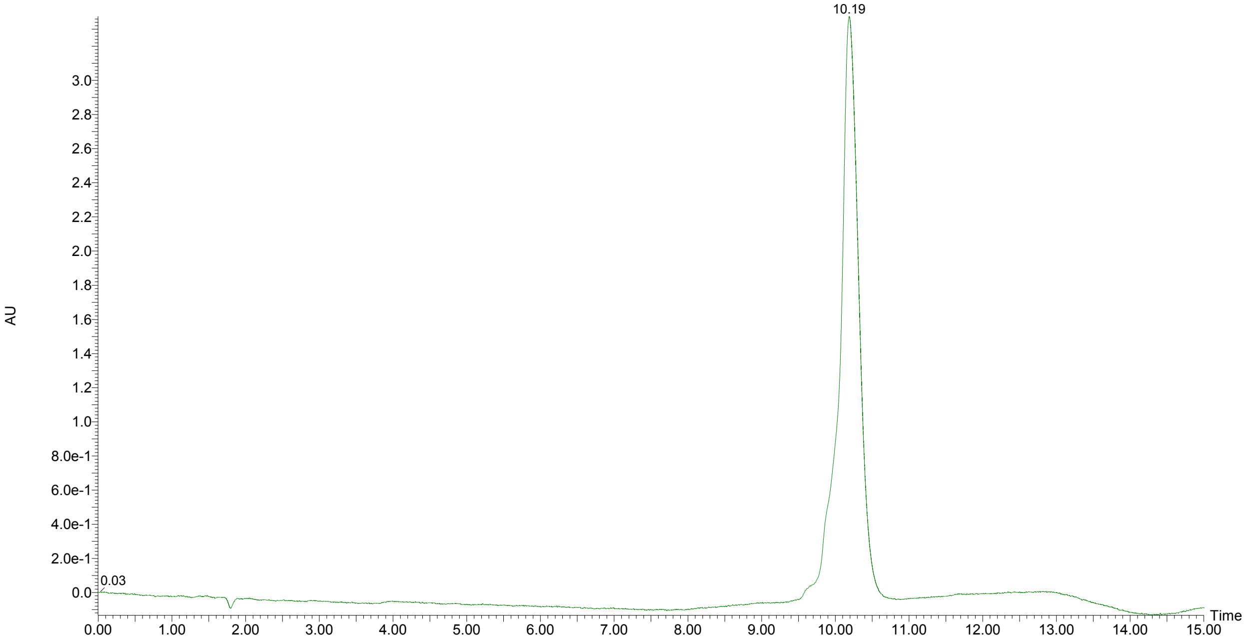

Figure S 3.11. HPLC trace of Peptide3.1+GG (Ac-KIKHVVKLK [EENSK]-G-G-[EKSEK] SKLRSQLVKRK-NH_2)

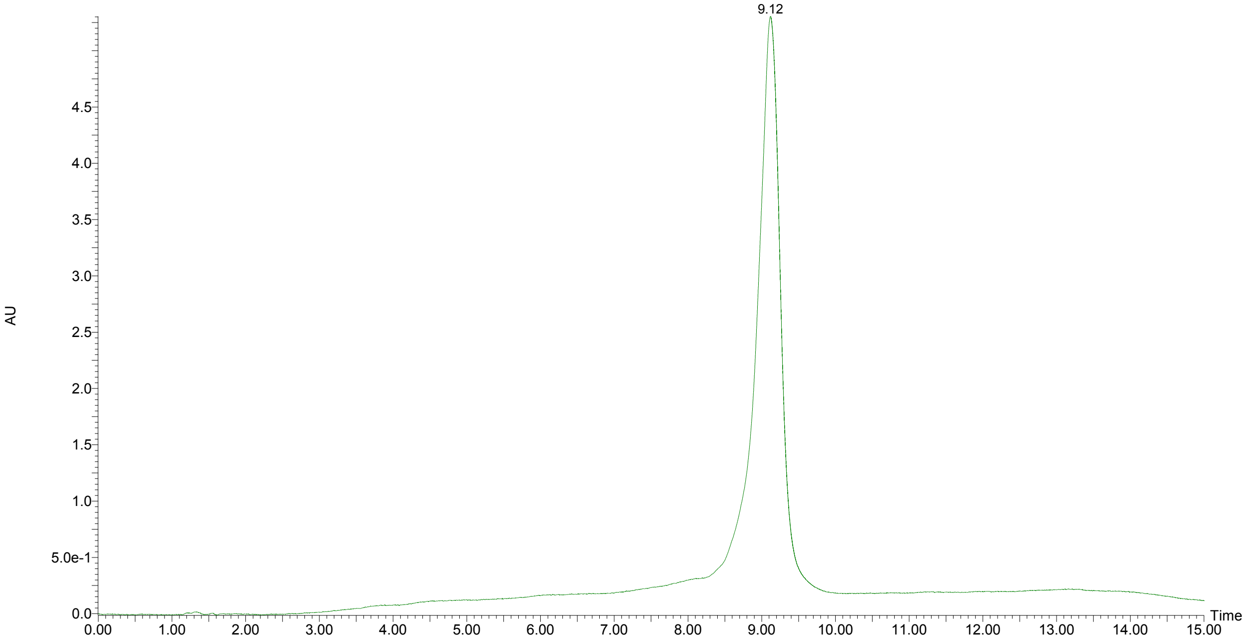

Figure S 3.12. HPLC trace of Peptide 3.1+AA (Ac-KIKHVVKLK [EENSK]-A-A-[EKSEK] SKLRSQLVKRK-NH_2)

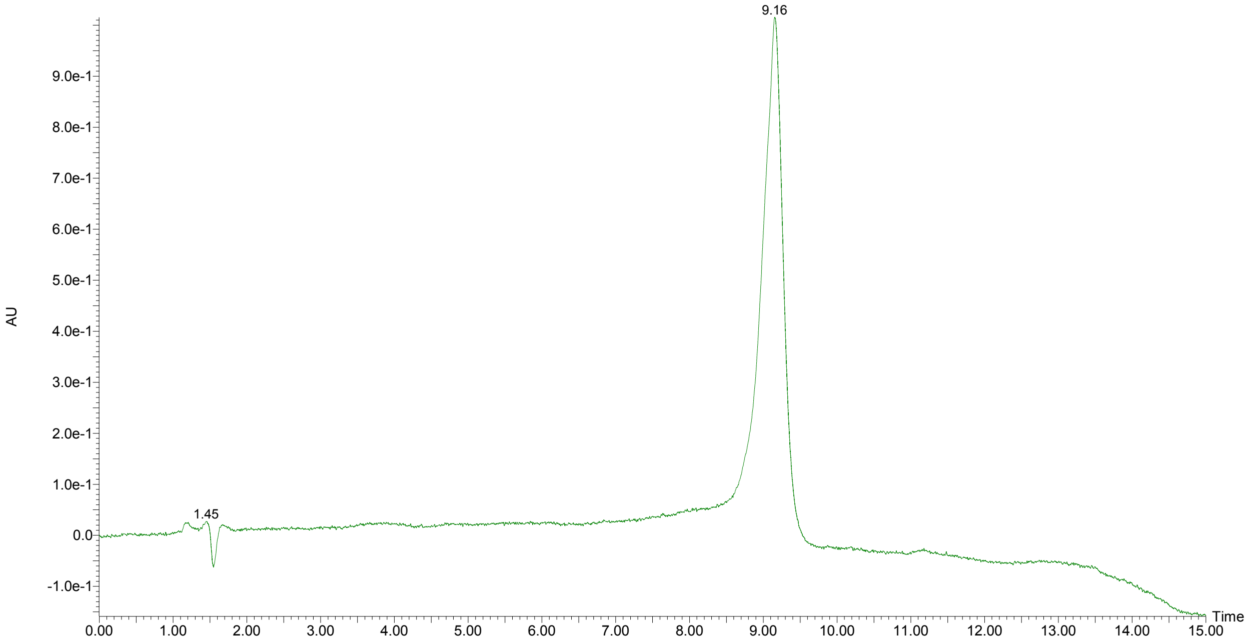

Figure S 3.13. HPLC trace of Peptide 3.1-KIK+AA (Ac-HVVKLK [EENSK]-A-A-[EKSEK] SKLRSQLVKRK-NH_2)

Table S 3.1. Expected and observed double stapled RHAMM peptide mimetics and the linear counterpart

Peptide ID	Expected m/z	Observed m/z
Linear	$[M+4H]^{4+} = 897.55$ $[M+5H]^{5+} = 718.24$ $[M+6H]^{6+} = 598.70$ $[M+7H]^{7+}$ 513.46	$[M+4H]^{4+} = 897.43$ $[M+5H]^{5+} = 718.14$ $[M+6H]^{6+} = 598.61$ $[M+7H]^{7+} =513.24$
Peptide 3.1	$[M+5H]^{5+} = 722.84$ $[M+6H]^{6+} = 602.54$ $[M+7H]^{7+} =516.75$ $[M+8H]^{8+} = 452.15$	$[M+5H]^{5+} = 722.78$ $[M+6H]^{6+} = 602.48$ $[M+7H]^{7+} =516.55$ $[M+8H]^{8+} = 452.11$
Peptide 3.2	$[M+5H]^{5+} = 722.44$ $[M+6H]^{6+} = 602.20$ $[M+7H]^{7+} =516.46$ $[M+8H]^{8+} = 451.90$	$[M+5H]^{5+} = 720.03$ $[M+6H]^{6+} = 600.20$ $[M+7H]^{7+} =516.26$ $[M+8H]^{8+} = 451.86$
Peptide 3.3	$[M+5H]^{5+} = 722.84$ $[M+6H]^{6+} = 602.54$ $[M+7H]^{7+} =516.75$ $[M+8H]^{8+} = 452.15$	$[M+5H]^{5+} = 722.37$ $[M+6H]^{6+} = 602.14$ $[M+7H]^{7+} =516.54$ $[M+8H]^{8+} = 452.11$
Peptide 3.4	$[M+5H]^{5+} = 722.84$ $[M+6H]^{6+} = 602.54$ $[M+7H]^{7+} =516.75$ $[M+8H]^{8+} = 452.15$	$[M+5H]^{5+} = 722.22$ $[M+6H]^{6+} = 602.40$ $[M+7H]^{7+} =516.53$ $[M+8H]^{8+} = 452.09$

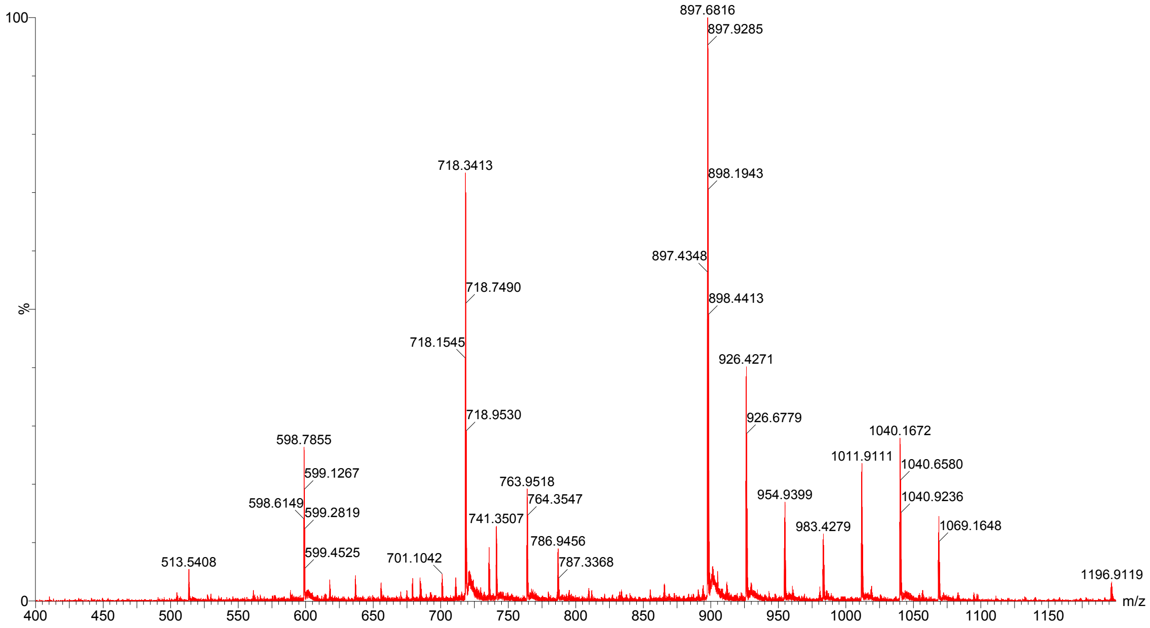

Figure S 3.14. ESI$^+$ Mass Spectrum for Linear peptide (Ac-KIKHVVKLKDENSQL KSEVSKLRSQLVKRK-NH$_2$)

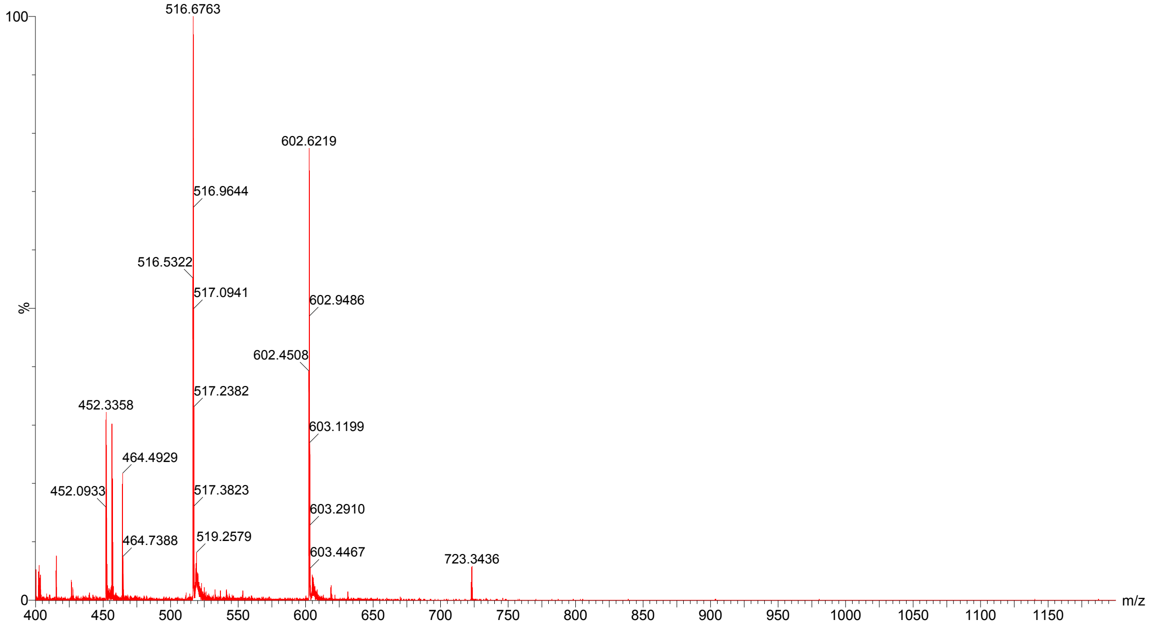

Figure S 3.15. ESI$^+$ Mass Spectrum for Peptide 3.1 (Ac-KIKHVVKLK [EENSK]-[EKSEK] SKLRSQLVKRK-NH$_2$)

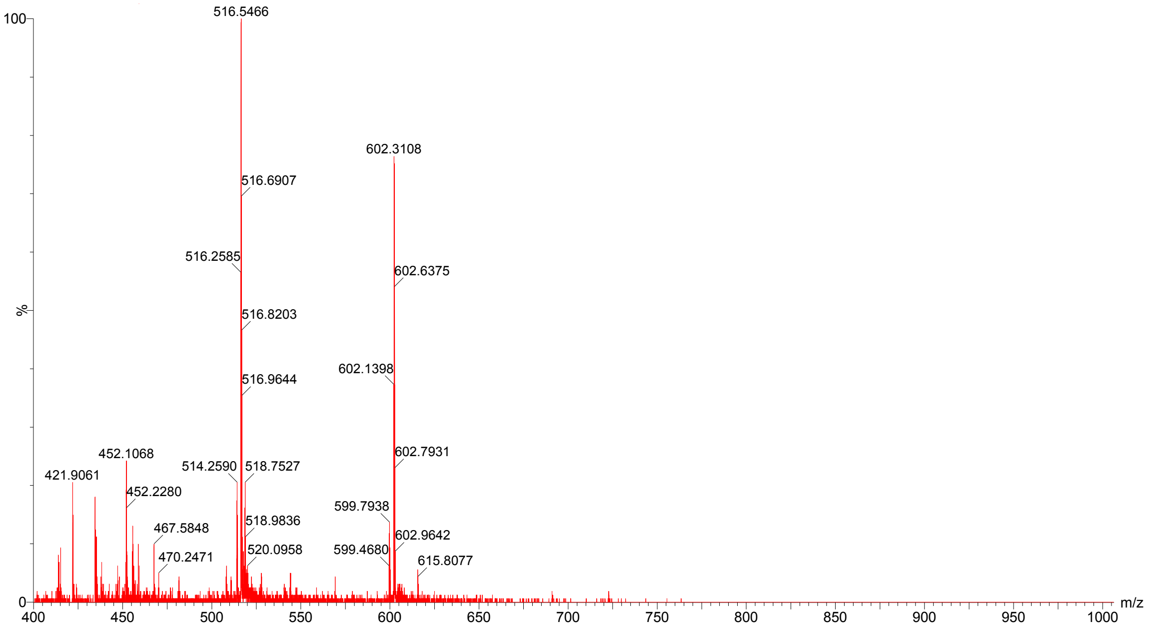

Figure S 3.16. ESI$^+$ Mass Spectrum for Peptide 3.2 (Ac-KIKHVVKLKD [ENSQK]-[ESEVK] KLRSQLVKRK-NH_2)

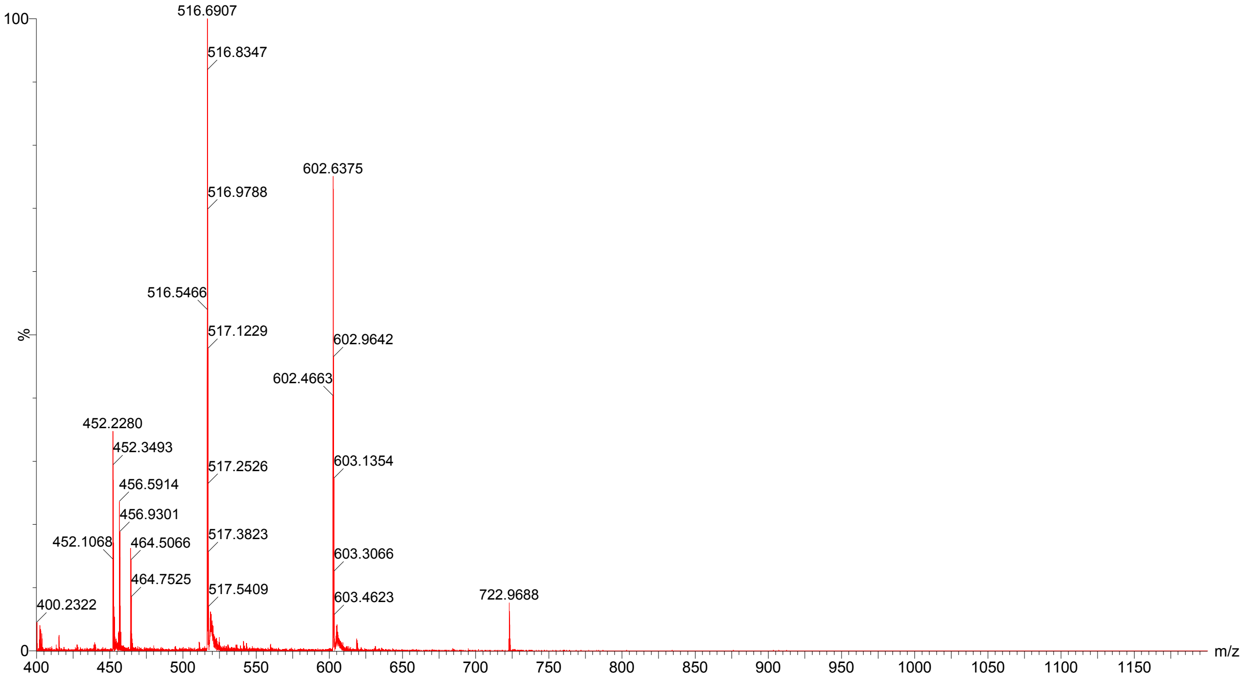

Figure S 3.17. ESI+ Mass Spectrum for Peptide 3.3 (Ac-KIKHVVKLK [EENSK]-[KKSEE] SKLRSQLVKRK-NH_2)

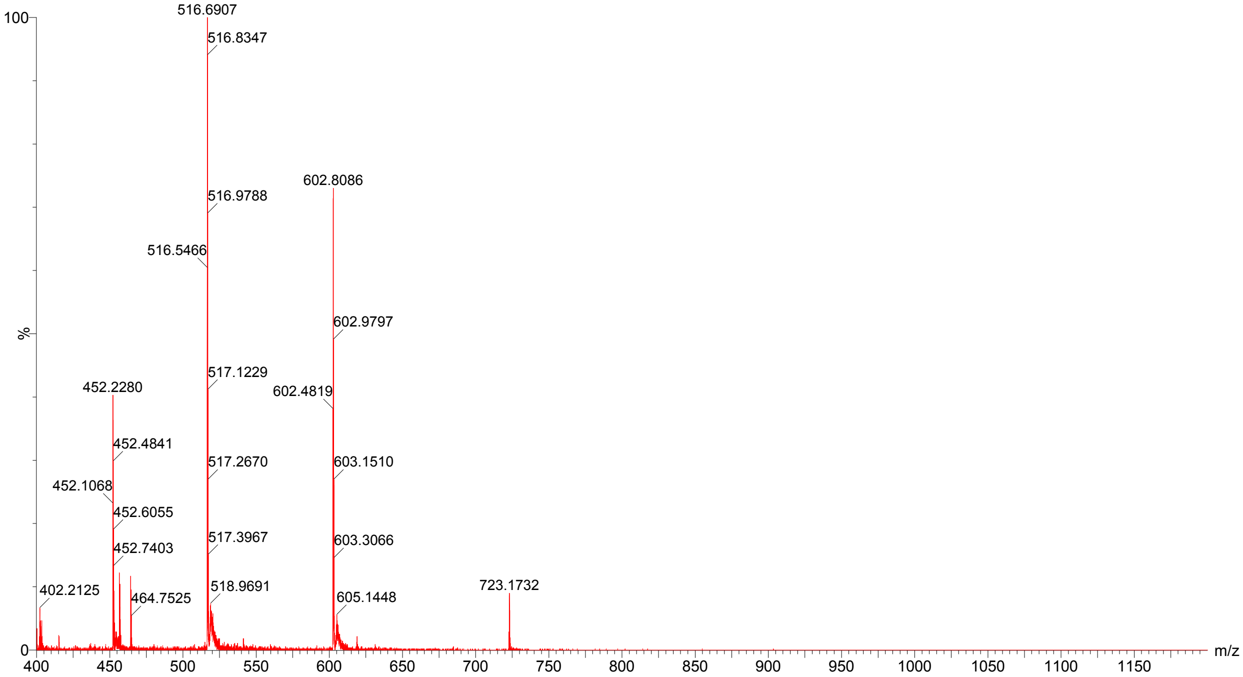

Figure S 3.18. ESI+ Mass Spectrum for Peptide 3.4 (Ac-KIKHVVKLK[KENSE]-[EKSEK] SKLRSQLVKRK-NH$_2$)

Table S 3.2. Calculated and observed m/z values for Peptide 3.1-series peptides

Peptide ID	Expected m/z	Observed m/z
Peptide 3.1-KIK	$[M+4H]^{4+}$ = 810.98 $[M+5H]^{5+}$ = 648.99 $[M+6H]^{6+}$ = 540.99 $[M+7H]^{7+}$ =464.00	$[M+4H]^{4+}$ = 811.25 $[M+5H]^{5+}$ = 649.02 $[M+6H]^{6+}$ = 541.01 $[M+7H]^{7+}$ =464.01
Peptide 3.1_1st staple	$[M+4H]^{4+}$ = 892.06 $[M+5H]^{5+}$ = 713.85 $[M+6H]^{6+}$ = 595.04 $[M+7H]^{7+}$ =510.32 $[M+8H]^{8+}$ = 446.53	$[M+4H]^{4+}$ = 892.06 $[M+5H]^{5+}$ = 713.85 $[M+6H]^{6+}$ = 595.04 $[M+7H]^{7+}$ =510.32 $[M+8H]^{8+}$ = 446.53

Peptide 3.1_2nd staple	$[M+4H]^{4+} = 899.79$	$[M+4H]^{4+} = 899.79$
	$[M+5H]^{5+} = 720.03$	$[M+5H]^{5+} = 720.03$
	$[M+6H]^{6+} = 600.20$	$[M+6H]^{6+} = 600.20$
	$[M+7H]^{7+} = 514.74$	$[M+7H]^{7+} = 514.74$
	$[M+8H]^{8+} = 450.40$	$[M+8H]^{8+} = 450.40$
Peptide 3.1+Gly	$[M+4H]^{4+} = 917.56$	$[M+4H]^{4+} = 917.56$
	$[M+5H]^{5+} = 734.25$	$[M+5H]^{5+} = 734.26$
	$[M+6H]^{6+} = 612.04$	$[M+6H]^{6+} = 612.07$
	$[M+7H]^{7+} = 524.89$	$[M+7H]^{7+} = 524.78$
	$[M+8H]^{8+} = 459.28$	$[M+8H]^{8+} = 459.67$
Peptide 3.1+Amb	$[M+5H]^{5+} = 749.48$	$[M+5H]^{5+} = 749.69$
	$[M+6H]^{6+} = 624.73$	$[M+6H]^{6+} = 625.23$
	$[M+7H]^{7+} = 535.77$	$[M+7H]^{7+} = 535.63$
	$[M+8H]^{8+} = 468.80$	$[M+8H]^{8+} = 469.07$
Peptide 3.1+GG	$[M+5H]^{5+} = 745.65$	$[M+5H]^{5+} = 745.69$
	$[M+6H]^{6+} = 621.54$	$[M+6H]^{6+} = 621.58$
	$[M+7H]^{7+} = 533.04$	$[M+7H]^{7+} = 533.07$
	$[M+8H]^{8+} = 466.41$	$[M+8H]^{8+} = 466.42$
Peptide 3.1+AA	$[M+5H]^{5+} = 751.26$	$[M+5H]^{5+} = 751.69$
	$[M+6H]^{6+} = 626.22$	$[M+6H]^{6+} = 626.25$
	$[M+7H]^{7+} = 537.04$	$[M+7H]^{7+} = 536.92$
	$[M+8H]^{8+} = 469.91$	$[M+8H]^{8+} = 469.92$
Peptide 3.1-KIK+AA	$[M+4H]^{4+} = 846.50$	$[M+4H]^{4+} = 846.40$
	$[M+5H]^{5+} = 677.40$	$[M+5H]^{5+} = 677.43$
	$[M+6H]^{6+} = 564.67$	$[M+6H]^{6+} = 564.85$
	$[M+7H]^{7+} = 484.29$	$[M+7H]^{7+} = 484.29$

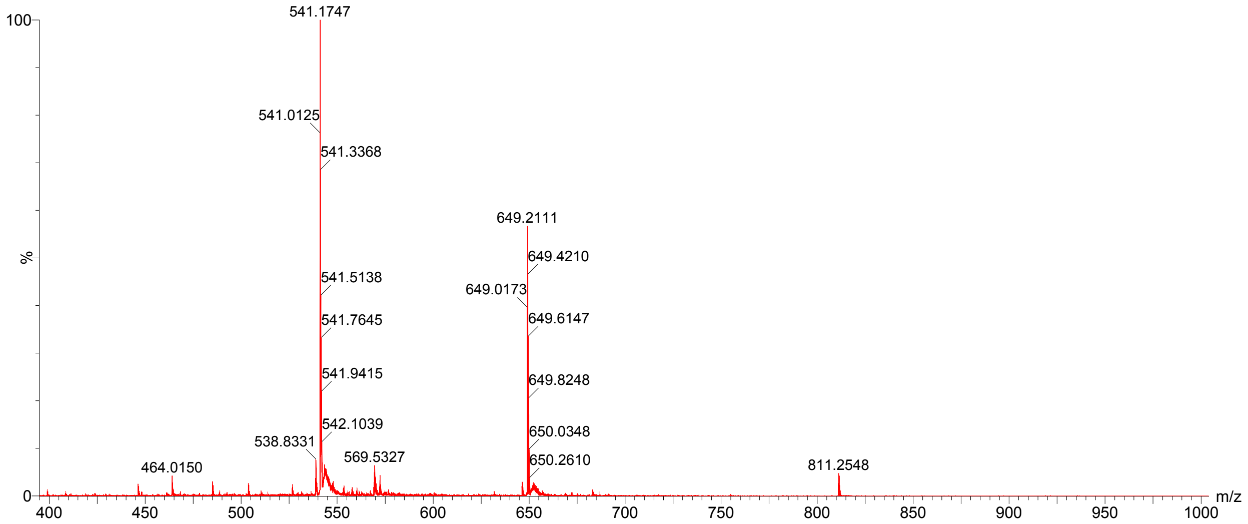

Figure S 3.19. ESI^{+} Mass Spectrum for Peptide 3.1-KIK (Ac-HVVKLK [EENSK]-[EKSEK] SKLRSQLVKRK-NH$_2$)

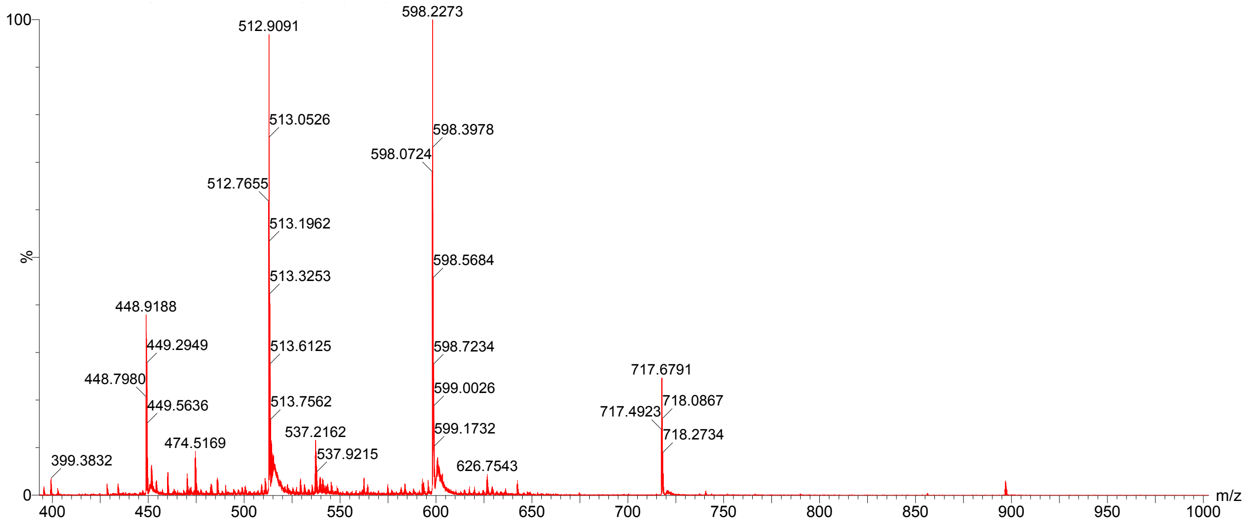

Figure S 3.20. ESI^{+} Mass Spectrum for Peptide 3.1_1st staple (Ac-KIKHVVKLK [EENSK]-LKSEV SKLRSQLVKRK-NH$_2$)

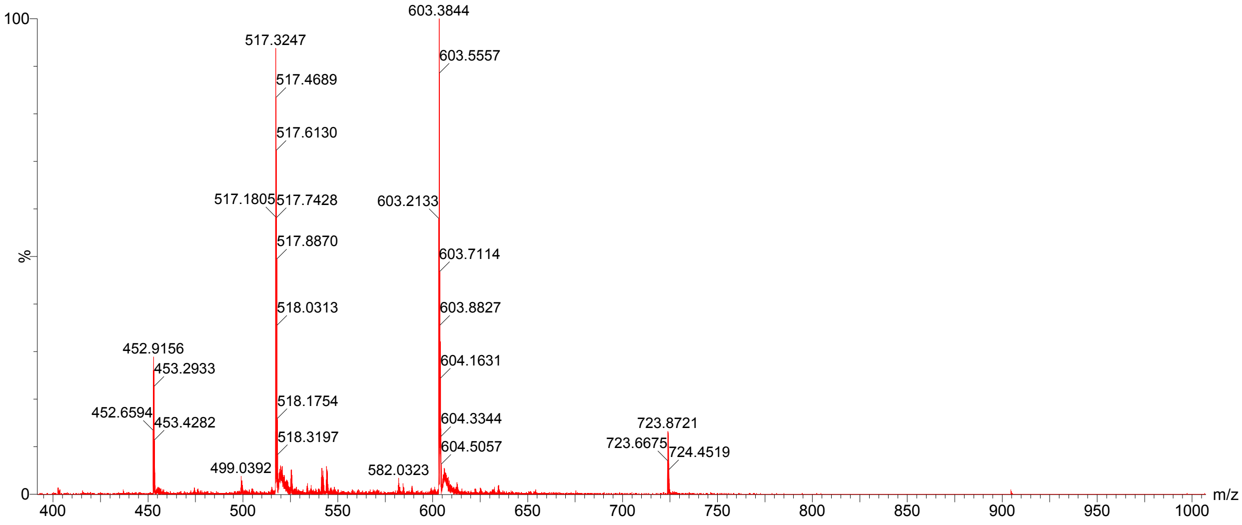

Figure S 3.21. ESI$^+$ Mass Spectrum for Peptide 3.1_2nd staple (Ac-KIKHVVKLK DENSQ-[EKSEK] SKLRSQLVKRK-NH$_2$)

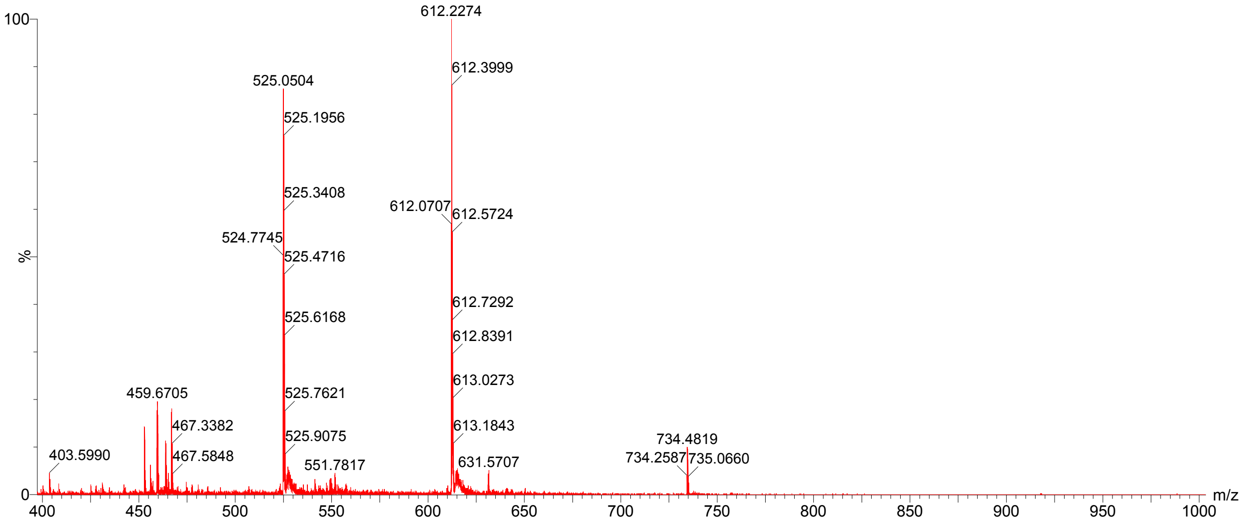

Figure S 3.22. ESI$^+$ Mass Spectrum for Peptide 3.1+Gly (Ac-KIKHVVKLK [EENSK]-Gly-[EKSEK] SKLRSQLVKRK-NH$_2$)

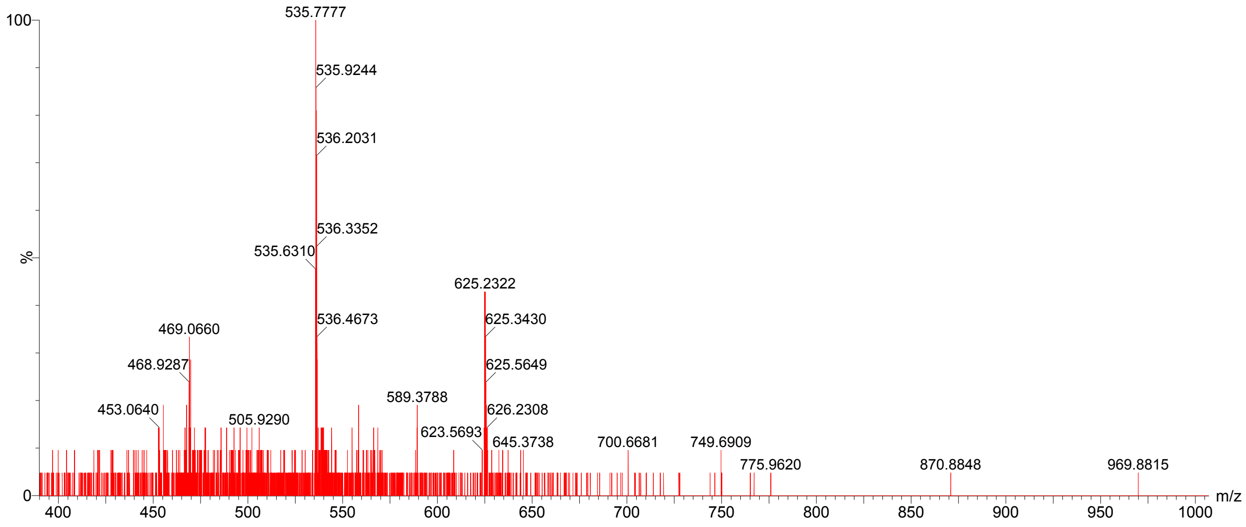

Figure S 3.23. ESI$^+$ Mass Spectrum for Peptide 3.1+Amb (Ac-KIKHVVKLK [EENSK]-Amb-[EKSEK] SKLRSQLVKRK-NH$_2$)

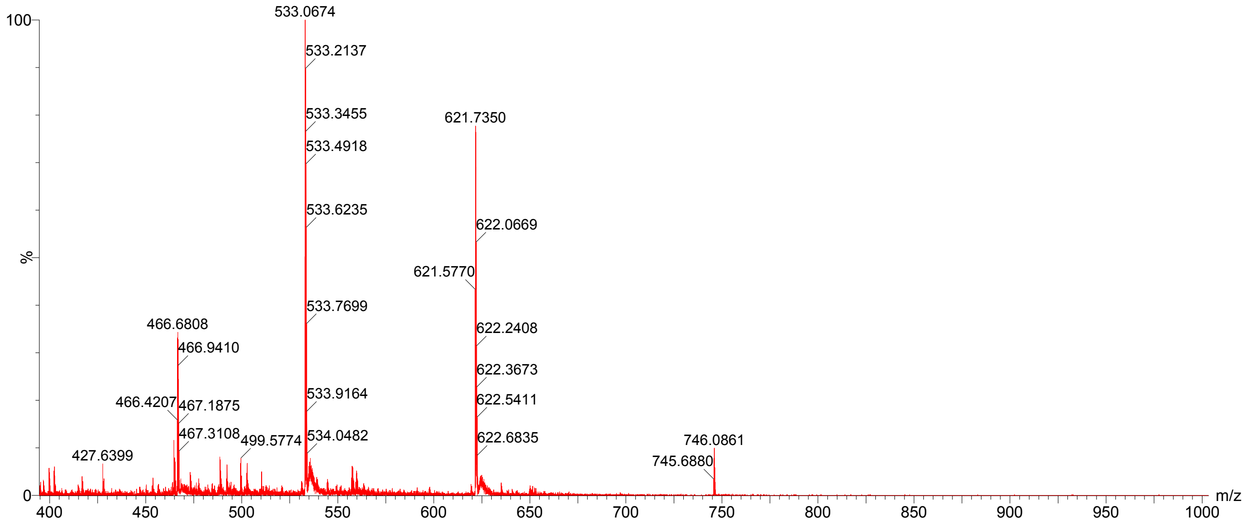

Figure S 3.24. ESI$^+$ Mass Spectrum for Peptide3.1+GG (Ac-KIKHVVKLK [EENSK]-G-G-[EKSEK] SKLRSQLVKRK-NH$_2$)

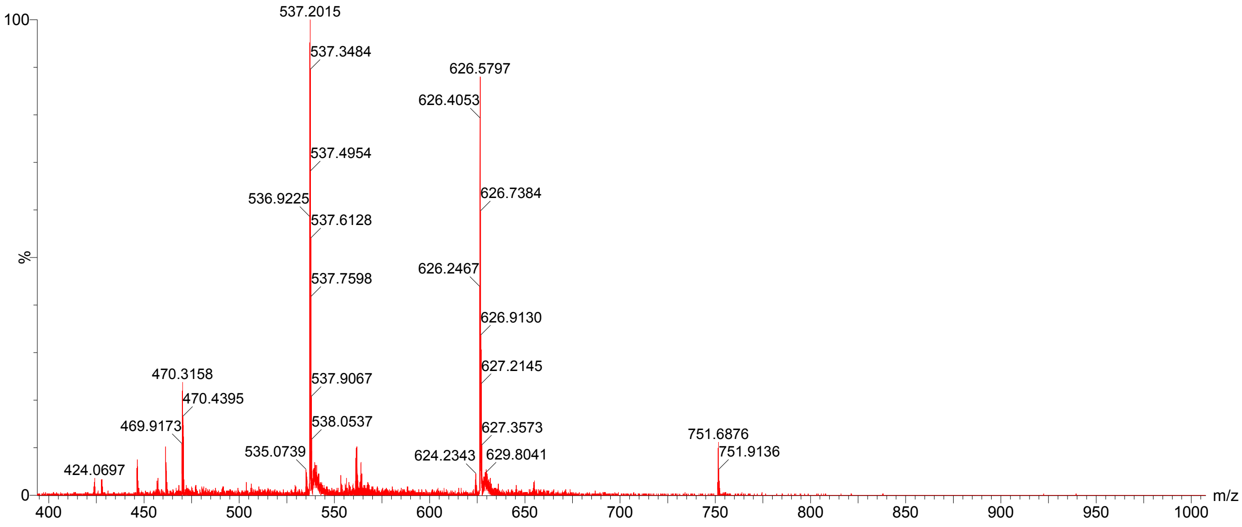

Figure S 3.25. ESI$^+$ Mass Spectrum for Peptide 3.1+AA (Ac-KIKHVVKLK [EENSK]-A-A-[EKSEK] SKLRSQLVKRK-NH$_2$)

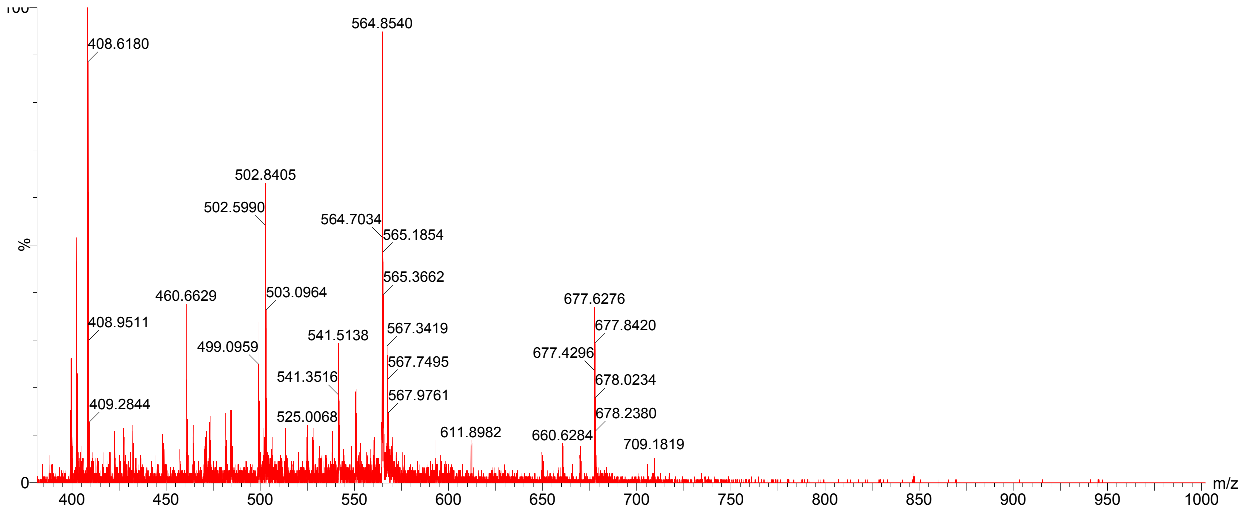

Figure S 3.26. ESI$^+$ Mass Spectrum for Peptide 3.1-KIK+AA (Ac-HVVKLK [EENSK]-A-A-[EKSEK] SKLRSQLVKRK-NH$_2$)

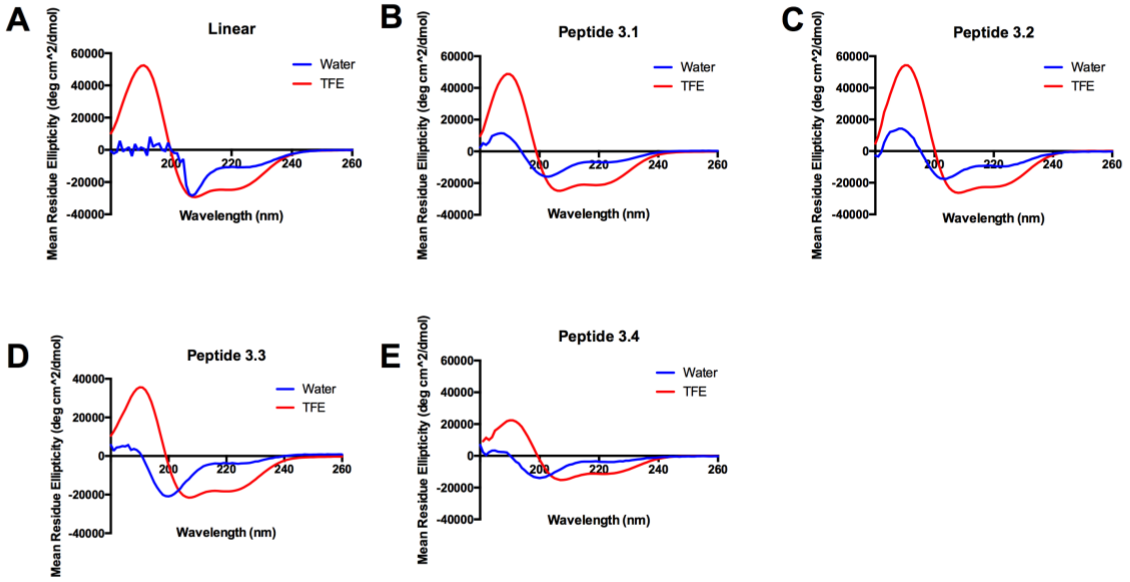

Figure S 3.27. CD spectra of double stapled Peptides 1-4 (B-E) and their linear counterpart (A) showing helicity in water and 40% TFE solution. Peptides were run at 0.25 mg/mL

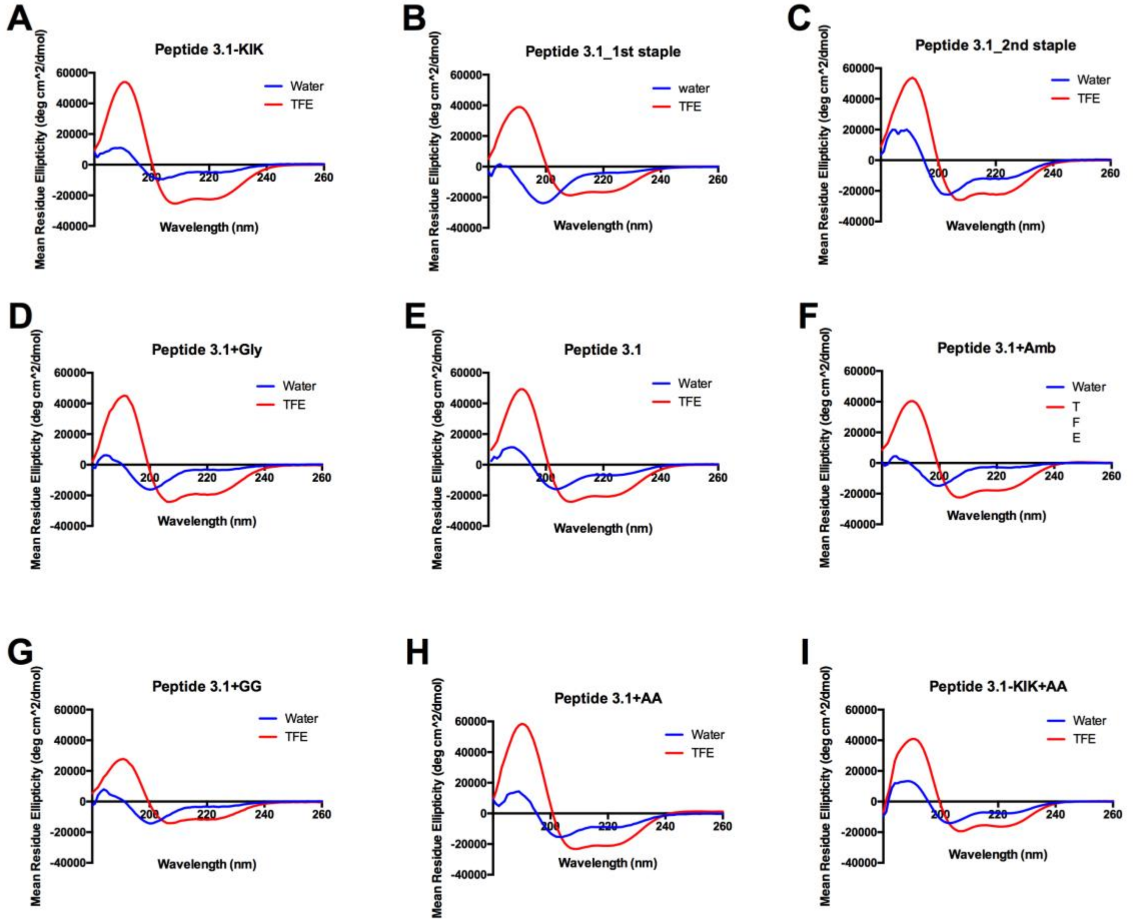

Figure S 3.28. CD spectra of modified double stapled peptides, in which the linker region and N-terminal sequence of Peptide 3.1 were modified. All peptides were run at 0.25 mg/mL in water and 40% TFE solution

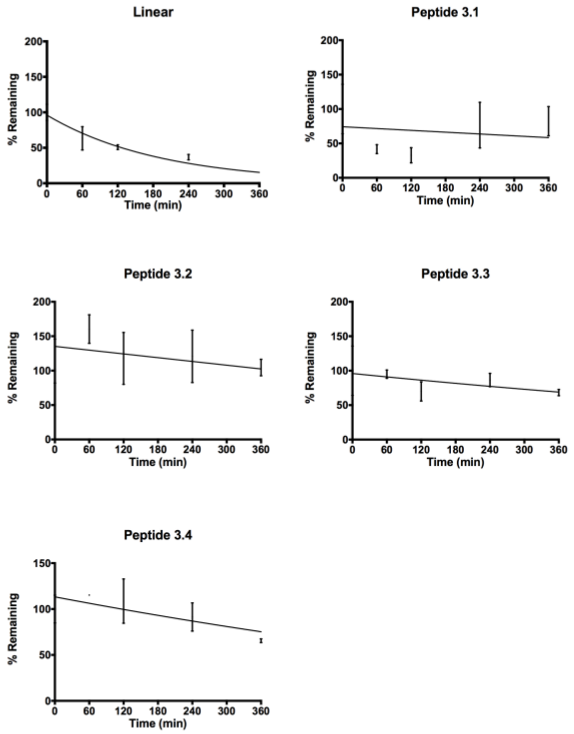

Figure S 3.29. Serum stability of Peptides 3.1-3.4 and their linear counterpart

Chapter 4

4 The development of an optical probe for measuring glomerular filtration rate

4.1 Introduction

Glomerular filtration rate (GFR) is a measure of kidney filtering capacity and renal function, and therefore, is a prognostic indicator of chronic kidney disease (CKD), such as graded renal artery stenosis. The polysaccharide, inulin, is considered the gold standard for measuring GFR clinically, as it is freely filtered through the kidneys, without being reabsorbed or secreted through peritubular capillaries or glomeruli. Therefore, the amount of inulin that is excreted in urine indicates the volume of plasma that is filtered by the glomeruli. The classic method of measuring GFR requires continuous intravenous administration of inulin, precise blood and urine collections over a 3-hour period, and bladder catheterization in order to ensure complete urine collection [1]. This laborious, tedious, and invasive method has diminished its clinical value in favour of faster estimated GFR (eGFR) values that can be easily obtained by endogenous serum creatinine levels. Unfortunately, the estimation suffers from a number of limitations that result in underestimated values compared with the physiological value. As a result, there has been considerable development of exogenous biomarkers for measuring GFR directly, and include probes that are radioisotopically labeled, such as ^{125}I-iothalamate [2], ^{51}Cr-ethylenediaminetetraacetic acid (EDTA) [3], and ^{99m}Tc-diethylenetriaminepentaacetic acid (DTPA) [4, 5], and those that are non-radioactive, such as iohexol [6], iothalamate [7, 8], fluorescently labeled sinistrin [9, 10] and fluorescein-labeled inulin [11, 12].

The measurement of GFR is a multi-faceted process, not only facilitating the detection and monitoring of chronic kidney disease, but also acts as a pre-screening method for identifying therapeutic efficiency. Drug dosing and uptake efficiency depends on a patient’s GFR, as many commonly administered drugs are excreted by the kidneys. Therefore, accurate measurement of GFR will permit more accurate dosing of drugs, and result in superior therapeutic outcome with fewer adverse complications.

Here, we propose the development of an optical probe based on inulin, the current clinical gold standard renal clearance biomarker, allowing for an efficient method of measuring GFR by transcutaneous pulse dye densitometer (TPDD) at 788 nm, without requiring blood sampling or urine collection. No reports exist on the synthesis and characterization of dye-labeled inulin. Fluorescein-labeled inulin is available commercially (Sigma Aldrich), but its synthesis is not described and its application is limited to measurements at 495 nm. It must be noted that the choice of dye used here, Cy7.5, was directed by the requirement of NIR absorption for enhanced penetration into human tissue, facilitating the detection of a probe with relative ease, and the convenience of a NIR dye that is commercially available. The method of synthesis proposed here allows for the functionalization of inulin with any dye molecule, and thus could satisfy any absorption wavelength requirement.

4.2 Results and Discussion

The novel optical probe described here is based on inulin, which is the current clinical standard for measuring GFR, and was synthesized by a straightforward method that does not require the immediate purification of the intermediate. Cy7.5-Inulin was prepared by a two-step synthesis via a non-toxic intermediate, carboxymethyl inulin (CMI) [13] (**Scheme 4.1**). The dye, functionalized with an amine, was conjugated to CMI after activation with EDC and NHS. The conjugate was then dialyzed exhaustively in water for a minimum of 3 days to remove any unconjugated dye or unreacted reagents.

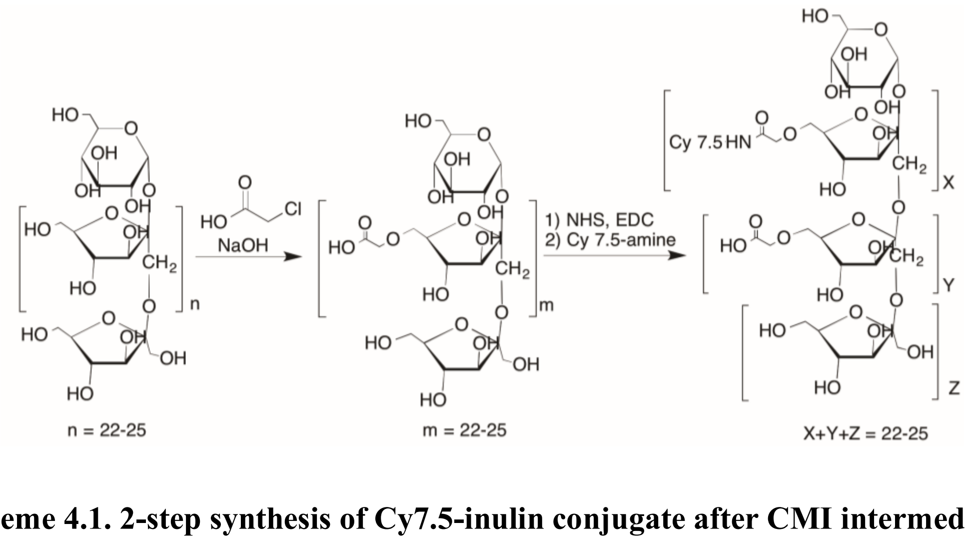

Scheme 4.1. 2-step synthesis of Cy7.5-inulin conjugate after CMI intermediate

Characterization of the starting material, inulin, the intermediate product, CMI, and the final dye-labeled inulin by FT-IR suggests that modifications made at each step allowed the successful addition of Cy7.5 to the carbohydrate (**Figure 4.1**). The appearance of new absorption signals at 1425 cm^{-1}, correlating with the –C-H bend of the methylene group, 1650 cm^{-1}, corresponding to the N-H bend of an amide, and 1708 cm^{-1}, corresponding to the carbonyl group of an amide, confirm the addition of the amine-functionalized dye to the inulin polysaccharide chain. The spectrum for inulin indicates that there might be a carbonyl in inulin (1660 cm^{-1}), which indicates that the polysaccharide's reducing end may be in its open chain form.

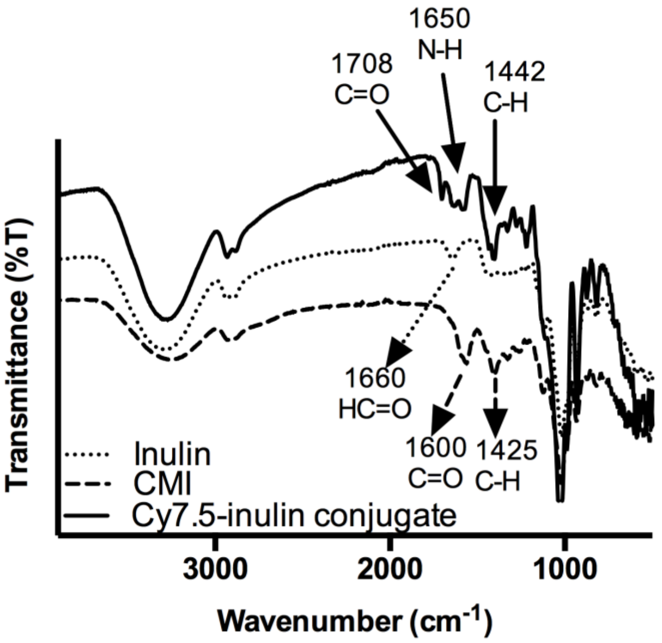

Figure 4.1. FT-IR spectrum showing shift in peaks as inulin is modified to CMI and Cy7.5-inulin conjugate and new functional groups are added

This transformation was further monitored by ^{1}H (**Figure S4.1**) and ^{13}C NMR spectroscopy (**Figure S4.2**). The conversion of inulin to CMI is noted by the appearance of the carboxylic signal (COOH) at two sites (162.97 ppm and 176.66 ppm), which were then converted to the amide (CONH) following the addition of the dye, with new carbonyl amide signals shifting to 158.76 ppm and 173.27 ppm, respectively (**Figure S4.2**). Signals representing Cy7.5 were observed in the aromatic region for the final product, which matched those of the commercial dye. We observed unreacted chloroacetic acid (169.97 ppm) in the carbon NMR of CMI, but noted that it was no longer present in the final dye-labeled conjugate, as the final conjugate is exhaustively purified by dialysis over 3-4 days, removing any unreacted reagents, including unreacted dye. We determined from the ratio of aromatic proton signals (associated with the dye) to signals identified as being part of the carbohydrate polymer (4.5 ppm to 5.5 ppm), that there are approximately 1-2 dye molecules per 10 sugar units, or approximately 2-4 dye molecules per inulin molecule (**Figure S4.1**). This was confirmed by absorption, in which a known amount of dye-conjugated inulin was measured by UV-Vis and compared with a standard curve of dye alone in order to determine the amount of dye by weight for each sample. Dye-loading efficiency ranged from 5% to 25%.

Mass analysis was carried out using matrix-assisted laser desorption/ionization mass spectrometry (MALDI-MS) (**Figure 4.2**) and electrospray ionization mass spectrometry (ESI-MS) (**Figure 4.3**), both of which confirmed the starting material as inulin by the 162 Da mass difference between peaks, correlating with glucose and fructose residues. However, because of the number of potential charged states produced from a single compound in ESI, poor ionization potential of polysaccharides, and the number of different sized sugar molecules present, we monitored the transformation from inulin to dye conjugate using MALDI, which produces singly charged ions almost exclusively [14]. In the spectrum, we were able to identify sodiated adducts, which agrees with the previously reported data for inulin [15, 16], and for each signal, we observed a corresponding signal of the polysaccharide with the reducing end residue (additional 18.015 Da). Reflectron mode and linear mode were used for the polysaccharides, and we observed fragmentation of the polysaccharides in both modes, with fructans containing from 3 to 25 residues being identified. This was unexpected, although fragmentation of large polymers to smaller ions during the MALDI process despite its soft ionization has been reported before for polysaccharides [17, 18]. ESI-MS disproved the size variability observed in MALDI, instead indicating the presence of a mixture of fructans containing 11 to 25 residues, with peaks assigned to the mass of the doubly charged molecular ion, which was calculated as twice the mass of 81.07n (mass of fructan units) + 38.96 (K mass) + 18.015 (additional mass of the reducing end residue), where n is the number of fructose units [17, 19]. The identification of sodium and potassium adducts by both mass spectrometry techniques confirms the presence of contaminants from the glass and plastic vials or plates, which can easily ionize with significant signal to noise ratios [20].

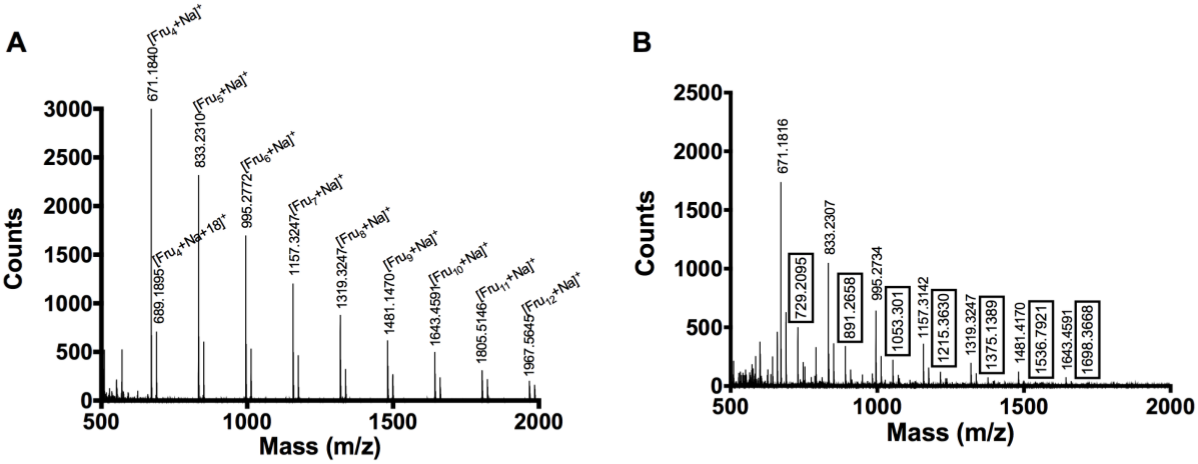

Figure 4.2. MALDI-MS of Inulin (A) and carboxymethyl inulin (CMI) (B) using DHB as matrix, acquired in reflectron mode. Masses were observed as sodiated adducts. A mass difference of 162 was observed for both inulin and CMI, and a mass difference of 57 Da was observed between inulin and CMI (boxed) (B).

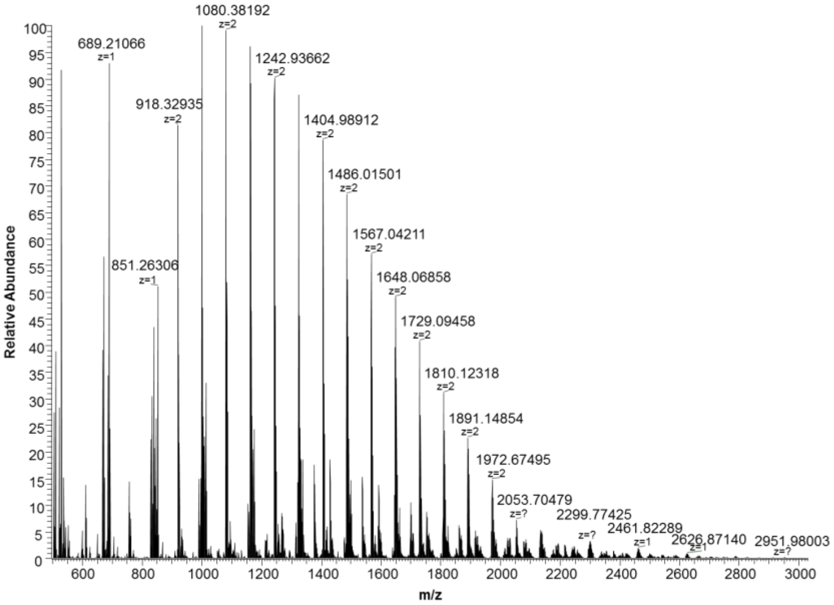

Figure 4.3. ESI-MS spectrum of inulin

A mass difference of 57 Da was observed between inulin and CMI, correlating with the mass of acetic acid to inulin (**Figure 4.2B**). However, there is an incomplete conversion of inulin to CMI, and starting material persists following the modification. It is unclear if each polysaccharide is equally modified with the same number of modified fructans per molecule, or if the number of modified monomers varies. Complete conversion is difficult to achieve [21], and the efficiencies of modifications of different sizes of polysaccharides vary. The range in number of carboxymethylated sites in CMI directly results in a range in the number of dye-conjugated sites in Cy7.5-inulin, where the maximal number of sites that can accept a dye molecule depends directly on the number of modified sites in CMI. Inconsistencies in the number of modified sites in CMI are not expected to cause any negative toxic effects, as both inulin and CMI have been conclusively determined to be non-toxic in humans, and the mixture of inulin and CMI is expected to be freely filtered by the kidneys without inducing tubular secretion or reabsorption [13]. Similarly, disparities in the number of dye-conjugated sites is not expected to affect toxicity as the conjugate’s hydrodynamic diameter falls significantly below the average minimum capillary size of 4 microns [22] (**Figure 4.4**).

MALDI produced inconclusive results for the conjugate, instead resulting in the loss of the dye molecule from the polysaccharide, as well as a repeating signal pattern of 71 Da (**Figure S4.3**), which does not correlate with the mass of the sugar molecules or portions of the dye that could be reasonably fragmented. It is unlikely that the dye is fragmenting into smaller ions, or that the fructan units are breaking apart. We believe that MALDI is an insufficient method of monitoring the addition of the dye to the polysaccharide. Despite the wide use of MALDI for polysaccharide analysis, the technique may not be an ideal method for characterizing the modification of sugars, due to its relatively poor mass accuracy and polydispersity of polysaccharides, and may explain why it has not been successfully used for analyzing large linear polysaccharides to date [18]. In fact, MALDI is approximately 1500 times more efficient for proteins than for polysaccharides of the same mass [18]. However, analysis by dynamic light scattering (DLS) confirmed there was an increase in hydrodynamic diameter during the modification of inulin and the formation of the conjugate (**Figure 4.4**). Interestingly, two average size populations of starting material, inulin, are present, which when modified to the intermediate, are more homogenous in size. An increase in average size from ~10 nm for inulin to ~25 nm for CMI, followed by a change to ~90 nm for the dye conjugate was observed. The large size change from CMI to dye-loaded inulin may be the result of the loading of multiple dye molecules, which was also determined by NMR, but may also indicate aggregation of the conjugate.

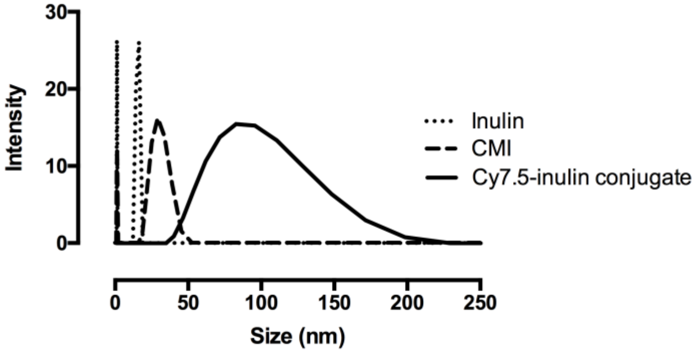

Figure 4.4. Dynamic light scattering of inulin, CMI, Cy7.5-inulin conjugate

The stability of the conjugate was evaluated by incubation in 25% plasma derived from volunteer patient blood at 38 °C for different periods over a 2-hour period, at 38 °C. After absorption measurements were taken, the samples were placed on ice to slow down any plasma-related degradation, and were subsequently centrifuged in centrifugal filter units. Following centrifugation, water and any particles smaller than the 3 kDa MWCO filter were pulled down in the eluent, while the conjugate and plasma were retained in the filter. Little to no change was observed in the absorption measurements following reconstitution to the same volume as the initial absorption measurements (**Figure 4.5**), indicating that both the dye and the dye-carbohydrate site of conjugation are robust enough for *in vivo* applications. However, the pharmacokinetic properties of the conjugate are unknown.

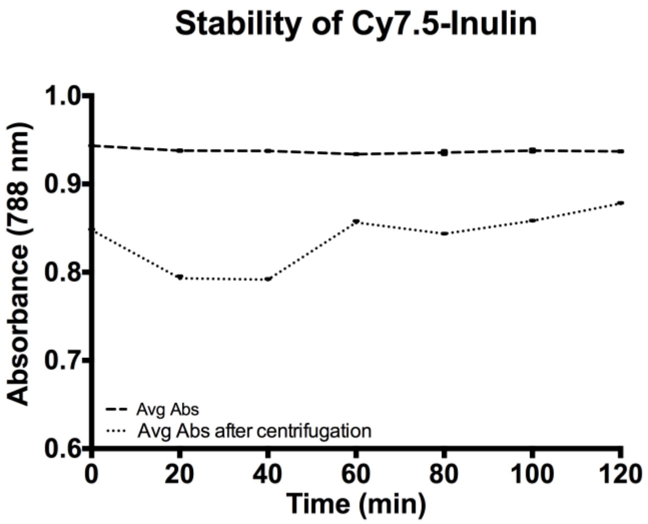

Figure 4.5. Cy7.5-inulin is stable in plasma from CKD patients over 2 hours. Each measurement was done in triplicate. The eluent following centrifugation, which contained water and particles <3 kDa in size, had absorption values < 0.05 at all time points.

Absorption measurements by UV-Vis spectrophotometry verified the absorption capacity of the dye-carbohydrate conjugate (**Figure 4.6**). In plasma alone, obtained from the blood of volunteer patients with chronic kidney disease (CKD), little is absorbed above 700 nm, while the conjugate readily absorbs at wavelengths greater than 700 nm. This suggests that all *in vivo* measurements taken at wavelengths greater than 700 nm would be measuring only the dye-carbohydrate conjugate as it circulates through the body and passes through the glomeruli.

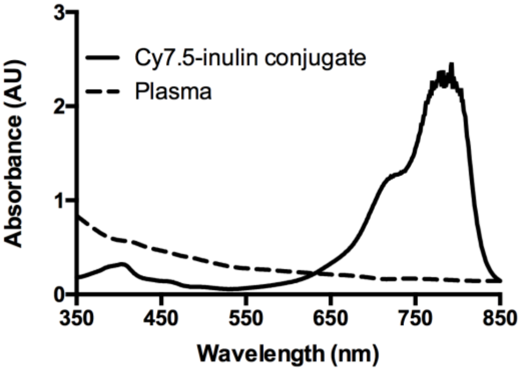

Figure 4.6. Plasma from patients with chronic kidney disease does not absorb significantly at 788 nm, where Cy7.5-inulin has its maximal absorption in plasma.

Preliminary evaluation of the conjugate has been carried out in farm-raised pigs with decreasing GFR from graded renal artery stenosis. Monitoring and analysing the plasma clearance of the conjugate allows for calculation of both the GFR and the optimal dose of drugs that filter primarily through the kidneys, such as carboplatin. Drug-related complications are partly associated with poor plasma clearance, and this subsequently increases the risk of adverse reactions from the drug. For example, most anticancer drugs have an optimal area under the curve (AUC) of the plasma drug concentration vs time curve that leads to the best therapeutic efficacy with a level of acceptable adverse reaction risks. If the drug is entirely cleared from the body by the kidneys, then the Calvert formula [23] relates the dosage needed to achieve the optimal AUC with the patient's GFR. With the development of an optical marker, such as Cy7.5-inulin, the procedure for measuring GFR can be greatly simplified. Analogous to the Calvert formula, GFR determination also depends on the AUC of plasma Cy7.5-inulin clearance curve, as shown in Figure 4.7.

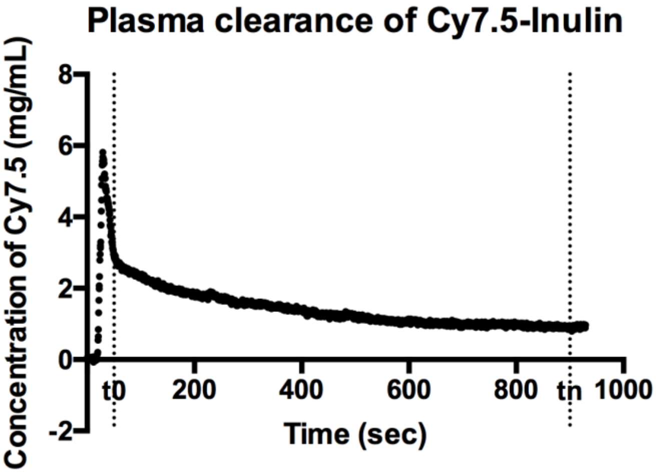

Figure 4.7. Transcutaneous pulse dye densitometry reading of Cy7.5-inulin at 805 nm in the plasma of a farm-raised pig after intravenous injection of the dye. GFR was calculated as the ratio of the amount of dye injected to the AUC, resulting in an estimated value of 120 mL/min, which is comparable with a GFR of 130 mL/min in a healthy 70 kg pig [24].

4.3 Conclusion

Here, we report the synthesis and characterization of dye-labeled inulin for use as an optical probe to accurately measure GFR efficiently and non-invasively. This soluble conjugate will also allow for optimal dosing of drugs that are filtered by the kidneys in order to achieve the most efficient therapeutic outcome. To our knowledge, there is no published protocol for the synthesis of dye-labeled inulin, and no commercially available NIR dye-labeled inulin other than fluorescein-labeled inulin. Following this procedure, more variations can be produced allowing for a range of applications. The conjugate is stable under the conditions needed to measure GFR *in vivo*. Preliminary evaluation of the probe is currently underway in farm-raised pigs with decreasing GFR from graded renal artery stenosis.

4.4 Methods

4.4.1 Synthesis of carboxymethyl inulin (CMI)

CMI was synthesized using a method described by Creixell et al. (2010) and Santiago-Rodriguez et al. (2013). Inulin (500 mg, DP 22-25) (Alfa Aesar) was dissolved in 2.5 mL deionized water at room temperature. Cold 10 M NaOH was added slowly in multiple aliquots, with stirring, for a total volume of 400 μL. Chloroacetic acid (276 mg, 2.9 mmol) was added immediately, and the mixture was heated to 70 °C for 75 minutes. The solution was cooled to room temperature, and neutralized with acetic acid. An excess of cold ethanol was added to precipitate the reaction product. The product was then pelleted by centrifugation and lyophilized until a dry, solid powder was obtained.

4.4.2 Cy7.5 labeling of CMI

For conjugation of Cy7.5 dye to CMI, the polysaccharide was activated with N-hydroxysuccinimide (NHS) and 1-ethyl-3-(3-dimethylaminopropyl)-carbodiimide (EDC). For this to occur, CMI (40-50 mg) was dissolved in water, and 1 molar equivalent of NHS and EDC were added. Activation was carried out for 1.5 hours with shaking. The activated CMI solution was subsequently added drop wise to Cy7.5-amine (Lumiprobe) (10-15 mg, 12.2-18.3 μM), dissolved in dimethyl sulfoxide (DMSO). The conjugation of the dye to CMI was allowed to proceed for 24 hours at room temperature, in the dark with shaking. The conjugated product was then lyophilized to provide a dry green crystalline product.

4.4.3 Dialysis of dye-labeled CMI

Cy7.5-conjugated inulin was resolubilized in 10:90 DMSO:water and added to a pre-treated biotech cellulose ester membrane dialysis tube (Float-a-Lyzer, Spectrum Labs, Phoenix, AZ) with a biotech grade cellulose ester membrane. Exhaustive dialysis was carried out in water with spinning in the dark. Following dialysis, the solution was lyophilized until a dry green powder was obtained.

4.4.4 FT-IR (ATR)

All measurements were carried out on a Perkin Elmer Spectrum Two IR Spectrometer, UATR-unit diamond. IR spectra were analysed using OMNIC 8.2.0.389 (Thermo Scientific Inc.)

4.4.5 Absorption measurements

All absorption readings were performed on an Agilent Cary 60 UV-Vis Spectrophotometer, and data was acquired in the Scan and Simple Reads applications (both version 5.0.0.999) in Cary WinUV version 5.0.0.1005. All optical density (OD) readings were performed at 406 nm (local maximum) in 50:50 DMSO:water.

4.4.6 Dynamic Light Scattering

All measurements were performed at 25 °C using a Zetasizer Nano ZS instrument from Malvern Instruments. Three measurements, each with a duration of 10 seconds, were performed at an angle of 173 degrees Backscatter (NIBS default). Three runs, each with a duration of 10 seconds, were performed. Samples were prepared in Milli Q water at a concentration of 0.8 mg/mL.

4.4.7 Plasma stability

Blood was obtained from volunteer chronic kidney disease (CKD) patients. Patient plasma was then obtained by mixing the blood with sodium heparin, and centrifuged to obtain supernatant.

Cy7.5-inulin conjugate was dissolved in 25% patient plasma. Absorption readings were taken after t=0 min, 20 min, 40 min, 60 min, 80 min, 100 min, and 120 min of incubation with plasma. All samples except those in the 0-minute time period were incubated at 38 °C. For those samples that were used for more than one incubation period, after each absorption measurement was taken at the end of an incubation period, the samples were placed on ice, and centrifuged at 3000 RPM at 20 °C for 40 minutes in pre-treated Amicon Ultra-15 Centrifugal Filters, MWCO 3kDa (Merck Millipore Ltd.). The ultrafiltrate was then incubate with 25% patient plasma for the time required before new absorption readings were obtained after the volumes were brought to 1 mL. The absorption readings from different incubation periods were compared. The National Research Council Canada's Research Ethics Board approved the protocols for blood withdrawals from patients with chronic kidney disease and treatment procedures described in this study (REB # 108616).

4.4.8 NMR

All spectra were recorded on a Bruker 400 Advance III HD NMR spectrometer (Bruker, Germany) equipped with an Oxford AS400/54 magnet. The samples were all run in DMSO-d_6 at room temperature, with a delay D1 of 10 seconds in the carbon to ensure full relaxation of the carbonyl signals. The field strength was 100 MHz for carbon, and 400 MHz for proton.

4.4.9 MALDI-TOF-MS

Mass spectrometric data were obtained using an AB Sciex 5800 TOF/TOF System, MALDI TOF (Framingham, MA, USA). Data acquisition and data processing were respectively done using a TOF TOF Series Explorer and Data Explorer (both from AB Sciex). The instrument is equipped with a 349 nm Nd:YLF OptiBeam On-Axis laser. The laser pulse rate was 400 Hz. Reflectron positive mode was used and each mass spectrum was collected as a sum of 500 shots. The samples were dissolved in deionized water (1 mg/mL) and mixed with the matrix, 2,5-dihydroxybenzoic acid (DHB), at 1:1 ratio. DHB was prepared as 20 mg/mL in 50% acetonitrile and 0.1% trifluoroacetic acid.

4.4.10 ESI-MS

Prior to high resolution mass spectrometry (HRMS) analysis, lyophilized inulin was reconstituted in 5 mM sodium acetate solution to 1 mg/mL, and filtered into a HPLC vial using a 0.45 um PTFE syringe filter (Chrome Spec). HRMS data was obtained using a Q-Exactive Orbitrap mass spectometer (Thermo Fisher Scientific). The sample was introduced at 3.0 mL/min by direct injection in positive ESI ionization mode using the following settings: capillary voltage, 3.9 kV; capillary temperature, 400 °C; sheath gas, 18 units; auxillary gas, 8 units; probe heater temperature, 450 °C; S-Lens RF level, 45.

Full MS data were obtained using the following conditions: scan range, 500-3000 m/z; resolution, 70,000; AGC target, 3e6; max IT, 200 ms. Data was processed using Thermo Xcalibur software.

4.4.11 *In vivo* Transcutaneous pulse dye densitometry

The Cy7.5-inulin conjugate was dissolved in sterile water and filtered first through a 5 μm, followed by a 1.2 μm polytetrafluoroethylene (PTFE) filter. The solution was then injected into the ear vein of a farm-raised pig as a single bolus (1 mg/kg) following administration of an anesthetic. The signal intensity was monitored by a Nihon Kohden (NK) TPDD clipped to the tail of the pig, tuned to indocyanine green (ICG), which has a similar absorption wavelength as Cy7.5. Plasma clearance of the conjugate was calculated using the the 2-compartmental open model of drug distribution, in which an administered drug is eliminated from the body by an excretory mechanism. The plasma clearance curve was fitted by the sum of two decaying exponentials from the time that the dye equilibrated with the blood pool (t0) to the end of acquisition (tn) of pulse dye densitometry data. The AUC of the dye plasma curve was then determined by extrapolation of the fitted biexponential curve to infinity, and the addition of the area before t0, as the contribution from the vascular phase before dye equilibrium in the blood pool was achieved. The Animal Use Subcommittee of the Canadian Council on Animal Care at Western University approved the protocols for all pig handling and treatment procedures described in this study (protocol 2009092).

4.5 References

1. Smith, H.W., *Comparative physiology of the kidney.* J Am Med Ass, 1953. **153**(17): p. 1512-1514.

2. Thomaseth, K. and Amici, G., *Optimal design of a two-sample test for assessing [125I] iothalamate plasma clearance in peritoneal dialysis.* Nephrol Dial Transplant, 1998. **13**(9): p. 2265-2270.

3. Brändström, E., et al., *GFR measurement with iohexol and 51Cr-EDTA. A comparison of the two favoured GFR markers in Europe.* Nephrol Dial Transplant, 1998. **13**(5): p. 1176-1182.

4. Rabito, C.A., et al., *Noninvasive, real-time monitoring of renal function: the ambulatory renal monitor.* J Nucl Med, 1993. **34**(2): p. 199-207.

5. Rabito, C.A., et al., *Noninvasive, real-time monitoring of renal function during critical care.* J Am Soc Nephrol, 1994. **4**(7): p. 1421-1428.

6. Schwartz, G.J., et al., *Glomerular filtration rate via plasma iohexol disappearance: pilot study for chronic kidney disease in children.* Kidney Int, 2006. **69**(11): p. 2070-2077.

7. Agarwal, R., *Ambulatory GFR measurement with cold iothalamate in adults with chronic kidney disease.* Am J Kidney Dis, 2003. **41**(4): p. 752-759.

8. Dowling, T.C., et al., *Comparison of iothalamate clearance methods for measuring GFR.* Pharmacotherapy, 1999. **19**(8): p. 943-950.

9. Schock-Kusch, D., et al., *Transcutaneous measurement of glomerular filtration rate using FITC-sinistrin in rats.* Nephrol Dial Transplant, 2009. **24**(10): p. 2997-3001.

10. Schock-Kusch, D., et al., *Transcutaneous assessment of renal function in conscious rats with a device for measuring FITC-sinistrin disappearance curves.* Kidney Int, 2011. **79**(11): p. 1254-1258.

11. Yu, W., Sandoval, R.M. and Molitoris, B.A., *Rapid determination of renal filtration function using an optical ratiometric imaging approach.* Am J Physiol Renal Physiol, 2007. **292**(6): p. F1873-1880.

12. Qi, Z., et al., *Serial determination of glomerular filtration rate in conscious mice using FITC-inulin clearance.* Am J Physiol Renal Physiol, 2004. **286**(3): p. F590-F596.

13. Johannsen, F.R., *Toxicological profile of carboxymethyl inulin.* Food Chem Toxicol, 2003. **41**(1): p. 49-59.

14. Jaskolla, T.W. and Karas, M., *Compelling evidence for lucky survivor and gas phase protonation: the unified MALDI analyte protonation mechanism.* J Am Soc Mass Spectrom, 2011. **22**(6): p. 976-988.

15. Caleffi, E.R., et al., *Isolation and prebiotic activity of inulin-type fructan extracted from Pfaffia glomerata (Spreng) Pedersen roots.* Int J Biol Macromol, 2015. **80**: p. 392-399.

16. de Oliveira, A.J.B., et al., *Structure and degree of polymerisation of fructooligosaccharides present in roots and leaves of Stevia rebaudiana (Bert.) Bertoni.* Food Chem, 2011. **129**(2): p. 305-311.

17. López-García, M., et al., *MALDI-TOF to compare polysaccharide profiles from commercial health supplements of different mushroom species.* Food Chem, 2016. **199**: p. 597-604.

18. Hsu, N.Y., et al., *Matrix-assisted laser desorption/ionization mass spectrometry of polysaccharides with 2′, 4′, 6′-trihydroxyacetophenone as matrix.* Rapid Commun Mass Spectrom, 2007. **21**(13): p. 2137-2146.

19. Hung, W.-T., et al., *Structure determination of β-glucans from Ganoderma lucidum with matrix-assisted laser desorption/ionization (MALDI) mass spectrometry.* Molecules, 2008. **13**(8): p. 1538-1550.

20. Li, L., *MALDI mass spectrometry for synthetic polymer analysis*. Vol. 175. 2009: John Wiley & Sons.

21. Hao, C., et al., *Positive-and negative-ion matrix-assisted laser desorption/ionization mass spectrometry of saccharides.* Rapid Commun Mass Spectrom, 1998. **12**(7): p. 345-348.

22. Gregersen, M.I., et al., *Flow characteristics of human erythrocytes through polycarbonate sieves.* Science, 1967. **157**(3790): p. 825-827.

23. Calvert, A., et al., *Carboplatin dosage: prospective evaluation of a simple formula based on renal function.* J Clin Oncol, 1989. **7**(11): p. 1748-1756.

24. Luis-Lima, S., et al., *A Simple Method to Measure Renal Function in Swine by the Plasma Clearance of Iohexol.* Int J Mol Sci, 2018. **19**(1).

4.6 Supplemental Information

Table S 4.1. FTIR analysis of inulin, carboxymethyl inulin, and Cy7.5-labeled inulin

Polymer	–OH stretch (cm^{-1})	–NH stretch (cm^{-1})	–CO stretch (cm^{-1})	–CH bend (alkane) (cm^{-1})	–C=O stretch (cm^{-1})	–C=C– stretch (cm^{-1})	–CN stretch (cm^{-1})	–NH bend (cm^{-1})
Inulin	3277	–	1130	–	1660	–	–	–
CMI	3217	–	1134	1425	1600	–	–	–
C7.5-inulin conjugate	3320	3320	1123	1442	1708	1604	1228	1650

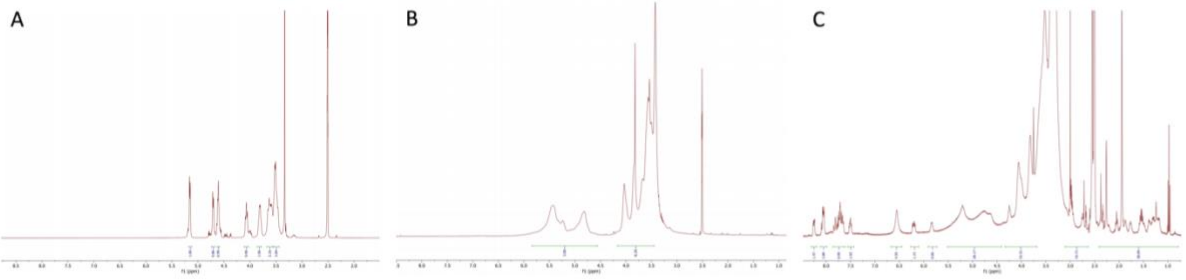

Figure S 4.1. Proton NMR spectra of Inulin (A), CMI (B), Conjugate (C). The signal at 5.15 ppm in inulin corresponds to the anomeric carbon. All samples were run in DMSO-d_6.

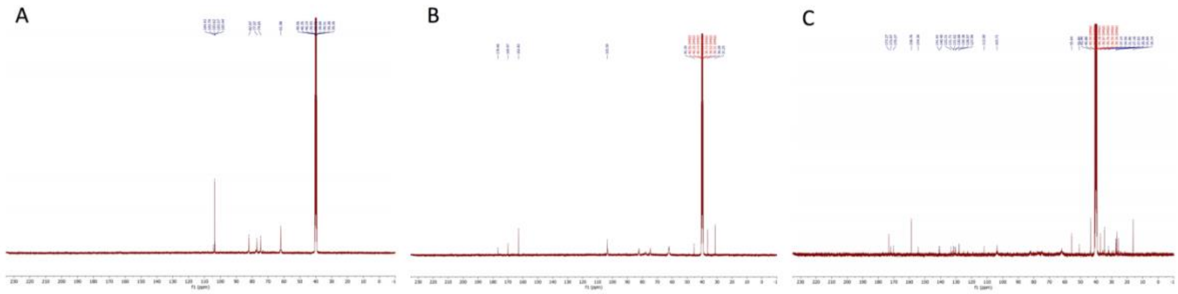

Figure S 4.2. Carbon NMR of Inulin (A), CMI (B), Conjugate (C). All samples were run in DMSO-d_6.

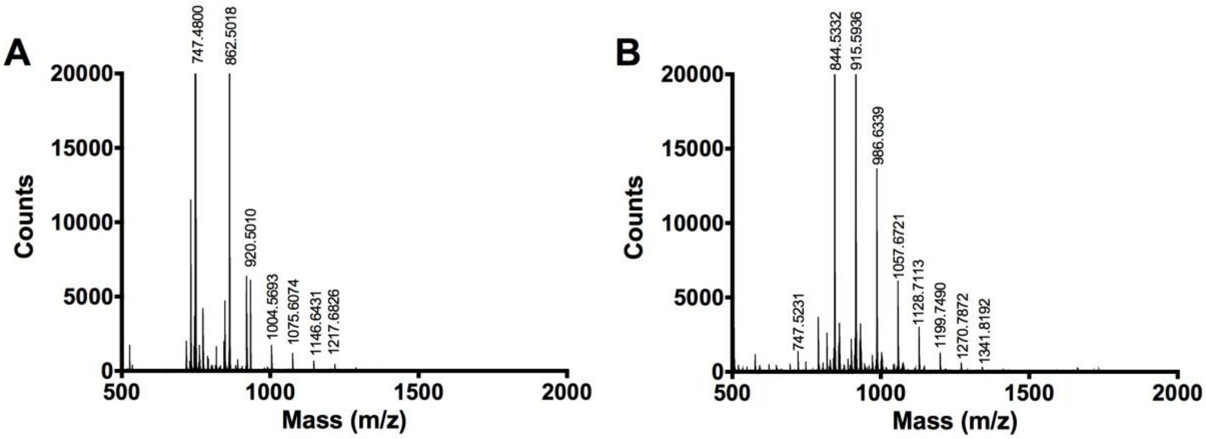

Figure S 4.3. MALDI-MS spectrum of dye-inulin conjugate. Depending on the sample, the dye was observed to cleave off easily, producing a strong signal (A) and subsequently fragment (A and B). Mass differences of 71 Da was also observed, which does not correlate with any mass where the polysaccharide could be easily fragmented.

Chapter 5

5 Outlook and conclusions

5.1 Outlook and conclusions

This thesis examined two separate principles. The first focused on the RHAMM-hyaluronan (HA) interaction and methods for interrupting their association in order to prevent the progression of diseases related to elevated RHAMM expression. The second focused on the development and characterization of an optical probe to measure glomerular filtration rate that is based on the clinical gold standard: the carbohydrate inulin.

The second chapter studied the development of a target receptor, 7 kDa RHAMM, for discovering and screening novel RHAMM-binding ligands. 7 kDa RHAMM is a 62-amino acid chemically synthesized receptor, and is the first report of a mini-protein with biological properties that was synthesized by continuous peptide chemistry. 7 kDa RHAMM was determined to be biologically active in inhibiting the migration of RHAMM-transfected 10T1/2 (LR21) cells, which we rationalize is the result of the chemically synthesized receptor blocking the native cell-surface receptor's motility-stimulating actions. This receptor was revealed to have the important alpha-helical character that has been described in the native protein [1, 2]. Because reports have indicated that the protein's secondary structure is important for it to bind its polysaccharide ligand, HA [1, 2], we expected the chemically synthesized receptor to also bind HA because it also exhibits alpha-helical character. This was found to be the case, and our reported dissociation constant of 8.98 nM is the first quantification of the RHAMM-HA interaction. The absence of protein-carbohydrate interaction analysis to date in the literature is most likely due to the lack of readily available full-length recombinant RHAMM protein. Similarly, new reports on novel RHAMM-binding ligands have likely been hindered by the lack of available protein for screening. While the synthesis and purification of recombinant RHAMM has been previously reported [3, 4], it is known to be a challenging process, which is reflected in the commercial price of the recombinant protein. 7 kDa RHAMM was further validated by evaluating its binding to previously reported tubulin-derived peptides [5]. Using SPR, the tubulin-derived peptides were determined to have very similar binding affinities to 7 kDa RHAMM as to recombinant RHAMM. It is therefore concluded that truncating the receptor to 7 kDa in size and producing it by chemical synthesis are suitable approaches for utilization in drug development programs for this novel target. This is exciting, as it provides a reliable tool for screening and discovering new compounds that are currently lacking in the clinic.

The third chapter discusses the development of novel double stapled RHAMM peptide mimetics for blocking the RHAMM-HA interaction. These double stapled peptides contain two adjacent lactam bridge staples that lie between both HA binding domains. The position of the staple within the peptide sequence and the order of amino acids making up the staples were evaluated and compared with the linear peptide for helicity, HA-binding potential, stability and bioactivity. A correlation between helicity, binding affinity and bioactivity was observed, and a lead compound was identified (Peptide **3.1**) (**Table 5.1**). Peptide **3.1** was further modified to explore the importance of rigidity in the linker region containing the staple to helicity and HA-binding. This was done by studying the effect of only one staple vs both staples, and by introducing a spacer between the staples in the linker region, including a single Gly residue, two residues (Gly and known helix-stabilizing Ala), and a hydrophobic residue (4-aminomethyl benzoic acid). In addition, the lead compound was synthesized without the notable cleavage product following incubation in serum. These efforts resulted in the identification of a new lead peptide sequence (Peptide **3.1-KIK+AA**) that is more stable against enzymatic degradation than the original compound, with improved helicity and binding to HA. While the bioactivity of this new compound has yet to be determined, the observed correlation between helicity, binding affinity, and bioactivity suggests that it will be active in inhibiting the release of pro-inflammatory cytokines. Similarly, it may have the potential to inhibit motogenic stimulus from elevated RHAMM expression, and therefore, have applications in treating cancers that involve RHAMM expression.

Table 5.1. Lead double stapled RHAMM peptide mimetics and their corresponding helicities and binding affinities for binding to 5-10 kDa HA

Peptide ID	Sequence	$[\theta]_{222}/[\theta]_{208}$ (Water)	K_D (nM)
3.1	Ac-KIKHVVKLK[EENSK]-[EKSEK]SKLRSQLVKRK-NH_2	0.65	88
3.1-KIK+AA	Ac-HVVKLK[EENSK]-AA-[EKSEK]SKLRSQLVKRK-NH_2	0.67	89

Elevated RHAMM expression propagates increased levels of fragmented HA, and therefore, there is an increase in RHAMM-HA interactions at the cell surface [6, 7]. Prior studies have shown that high RHAMM expression is correlated with highly invasive and aggressive disease, and in the case of cancer, highly metastatic disease [8]. In the case of cancer, current treatments are not always effective in targeting the primary tumor, which can lead to metastasis and poor patient outcome. Thus, there is a clinical need for the development of novel drug molecules that effectively target cells with aggressive or metastatic potential. This can be carried out with targeted therapeutics that sequester fragmented HA before it can activate the signaling cascade, thereby preventing the active transcription of motogenic and pro-inflammatory genes. While further research into the pharmacokinetic and pharmacodynamics properties of these compounds is required to properly validate and translate the peptides to a clinical setting, the double stapled RHAMM peptide mimetics provide a framework for developing fragmented HA-targeted therapeutic agents. The identified lead compound, Peptide 3.1-KIK-AA, can be used as the prototype drug molecule for treating those diseases that are affected by elevated RHAMM levels or fragmented HA. Specifically, patients suffering from pro-inflammatory conditions or cancers with RHAMM-overexpressing tumors could receive Peptide 3.1-KIK-AA as part of the treatment regimen in order to prevent worsening of the disease or metastatic effects from occurring.

The bioactivity studied in this chapter focused directly on inflammation by measuring the change in inflammatory cytokine levels before and after treatment with the peptides in question. This is an exciting application for therapeutic intervention of the RHAMM mimetic peptides, and could have potential use in treating inflammation early. However, other applications of these peptides are certainly viable, several of which have been explored at a preliminary level and were reported in the patent application No. PCT/IB2016/051587. Models in which they may have therapeutic application, and in which they deserve further evaluation, include fibrosis/adipogenesis and wound repair, specifically invasion and migration. In fact, different RHAMM mimetic peptides that inhibit the RHAMM-HA interaction were observed to promote adipogenesis and reduce tissue fibrosis [9], suggesting that the double stapled RHAMM mimetic peptides may also be effective in this model.

The fourth chapter discussed the development of an optical probe for measuring glomerular filtration rate (GFR), an indication of kidney function. The current clinical standard for measuring GFR is by quantifying the rate of renal elimination of inulin, which is neither metabolized nor reabsorbed by the renal tubules, and therefore passes through the body intact. The optical probe discussed in this chapter was based on the inulin structure, but was chemically modified for the conjugation of a dye molecule by way of a non-toxic intermediate [10]. This was the first detailed report on the synthesis and analysis of a dye-labeled inulin conjugate. The starting material, the intermediate, and the final compound were all characterized by a number of analytical techniques in order to monitor the synthetic progress, as well as determine the efficiency of dye-labeling. In addition, the probe was determined to be stable in serum following 2 hours of incubation at 38 °C, suggesting that dye conjugation results in a stable final product. Analysis by ^{1}H and ^{13}C NMR spectroscopy and absorption concluded that approximately 2-5 dye molecules per polysaccharide were added, which corresponds to approximately 5% to 25% dye by weight. The range of dye-labeling is not expected to pose toxicity related complications *in vivo*, as its diameter falls beneath the average capillary size. In fact, the probe has been evaluated *in vivo* in pigs with compromised kidneys, and shows promise in accurately measuring GFR. In addition to measuring GFR, this probe will allow for improved dosing of drugs that filter through the kidneys, such as carboplatin, a commonly administered anticancer drug. Despite its use as an anticancer drug, it results in adverse side effects and toxicities, including anemia and the suppression of bone marrow function [11, 12]. Delivering the optimal dose of drugs like carboplatin would help ensure that patients receive the optimal therapeutic result with a lower risk of treatment morbidity or toxicity.

The work carried out in the fourth chapter involved the use of a fluorescent dye. It should be noted that any dye that absorbs at the right wavelength (788 nm) could be used in place of a commercially available dye (ε = 223 000 L mol^{-1} cm^{-1}). This could include a novel synthetic dye, which could potentially be developed at a lower cost than the commercially available Cyanine dyes, which tend to be quite expensive. A current challenge faced with the probe is that Cy7.5-amine is not water-soluble, with no sulfonated versions commercially available. Similarly, the conjugate suffers from occasional solubility difficulties and is often trapped in the filter. When this occurs, the filtrate contains strictly conjugate with low dye loading, and is often insufficient for analysis by transcutaneous pulse dye densitometry (TPDD). Thus, the development of novel dyes with the appropriate absorption properties that have improved water-solubility over the current commercially available ones could improve dye-loading and facilitate the clinical translation of the probe.

In conclusion, this thesis described the development and characterization of chemical entities that have the potential to facilitate the translation of novel technologies to a clinical setting. Firstly, the development of 7 kDa RHAMM as a suitable replacement receptor for screening novel RHAMM-binding compounds will enable the screening and discovery of new therapeutic and imaging agents, permitting early treatment of diseases that are correlated with aggressive and metastatic phenotypes. In addition, the development of double stapled RHAMM peptide mimetics that bind to HA with strong affinity and that have function blocking activity in inflammation models both *in vitro* and *in vivo* are promising as potential therapeutic agents themselves, or as prototypes for designing other compounds. Lastly, the development of an optical probe based on the current clinical gold-standard, inulin, for measuring GFR efficiently and non-invasively, is exciting, and will allow for improved patient care both in individuals with compromised kidneys, as well as other diseases through the minimizing of risk associated with over- or under-dosing of renal excreted drugs.

5.2 References

1. Yang, B., Zhang, L., and Turley, E.A., *Identification of two hyaluronan-binding domains in the hyaluronan receptor RHAMM.* J Biol Chem, 1993. **268**(12): p. 8617-8623.

2. Ziebell, M.R. and Prestwich, G.D., *Interactions of peptide mimics of hyaluronic acid with the receptor for hyaluronan mediated motility (RHAMM).* J Comp Aid Mol Des, 2004. **18**(10): p. 597-614.

3. Mohapatra, S., et al., *Soluble hyaluronan receptor RHAMM induces mitotic arrest by suppressing Cdc2 and cyclin B1 expression.* J Exp Med, 1996. **183**(4): p. 1663-1668.

4. Nedvetzki, S., et al., *RHAMM, a receptor for hyaluronan-mediated motility, compensates for CD44 in inflamed CD44-knockout mice: a different interpretation of redundancy.* Proc Nat Acad Sci, 2004. **101**(52): p. 18081-18086.

5. Esguerra, K.V., et al., *Identification, design and synthesis of tubulin-derived peptides as novel hyaluronan mimetic ligands for the receptor for hyaluronan-mediated motility (RHAMM/HMMR).* Integr Biol, 2015. **7**(12): p. 1547-1560.

6. Veiseh, M., et al., *Uncovering the dual role of RHAMM as an HA receptor and a regulator of CD44 expression in RHAMM-expressing mesenchymal progenitor cells.* Front Cell Dev Biol, 2015. **3**: p. 63.

7. Tolg, C., et al., *Rhamm-/- fibroblasts are defective in CD44-mediated ERK1,2 motogenic signaling, leading to defective skin wound repair.* J Cell Biol, 2006. **175**(6): p. 1017-1028.

8. Tolg, C., et al., *Hyaluronan and RHAMM in wound repair and the "cancerization" of stromal tissues.* Biomed Res Int, 2014. **2014**: p. 103923.

9. Bahrami, S.B., et al., *Receptor for hyaluronan mediated motility (RHAMM/HMMR) is a novel target for promoting subcutaneous adipogenesis.* Integr Biol, 2017. **9**(3): p. 223-237.

10. Johannsen, F.R., *Toxicological profile of carboxymethyl inulin.* Food Chem Toxicol, 2003. **41**(1): p. 49-59.

11. Dilruba, S. and Kalayda, G.V., *Platinum-based drugs: past, present and future.* Cancer Chemother Pharmacol, 2016. **77**(6): p. 1103-1124.

12. Duffull, S.B. and Robinson, B.A., *Clinical pharmacokinetics and dose optimisation of carboplatin.* Clin Pharmacokinet, 1997. **33**(3): p. 161-183.

Curriculum Vitae

EDUCATION

2013-2018	Western University London, Ontario, Canada Doctorate
2007-2012	University of Toronto Toronto, Ontario, Canada B.Sc.

HONOURS AND AWARDS

2013-2014	Translational Breast Cancer Research Unit Studentship
2014-2015	Translational Breast Cancer Research Unit Studentship
2015-2016	Translational Breast Cancer Research Unit Studentship
2016-2017	Translational Breast Cancer Research Unit Studentship
2017-2018	Translational Breast Cancer Research Unit Studentship
2017	Host for Oncology Day keynote speaker, Dr. Paul J. Hergenrother, University of Illinois at Urbana-Champaign: June 16, 2017 (London, ON)
2017	Travel grant to 13th Medicinal and Bioorganic Chemistry Conference, Steamboat Springs, CO
2016	Travel Grant to 34th Annual European Peptide Symposium and 8th International Peptide Symposium, Leipzig, Germany
2015	Poster award at 12th Annual Oncology Research and Education Day

RELATED WORK EXPERIENCE

2013-2017	Teaching Assistant for Chemistry 2213 Western University
2015-2017	Research Chemist Novare Pharmaceuticals Inc.

CONTRIBUTIONS

Patent

Luyt, LG; Turley, E; **Hauser-Kawaguchi, A**; Rodrigues, E. 2015. Stapled Peptides as Mimics of the Receptor for Hyaluronan Mediated Motility (RHAMM). International Application No. PCT/IB2016/051587.

Book chapter

Hauser-Kawaguchi, A; Luyt, LG. Nanomedicine – Nanoparticles in Cancer Imaging and Therapy. Genomic Instability and Cancer Metastasis: Mechanisms, Emerging Themes, and Novel Therapeutic Strategies. Maxwell, C & Roskelley, C. eds.; Springer: Dordrecht. 205-244, 2015. DOI: 10.1007/978-3-319-12136-9_10.

Peer-Reviewed Publications

Hauser-Kawaguchi, A; Milne, M; Li, F; Lee, TY; Luyt, LG. *The development of a near infrared optical probe for measuring glomerular filtration rate*. Submitted to International Biological Macromolecules, **2018**.

Hauser-Kawaguchi, A; Tolg, C; Peart, T; Turley, E; Luyt, LG. *Truncating and chemically synthesizing RHAMM for the development of novel peptide drugs.* Submitted to Biomolecular and Medicinal Chemistry, **2018**.

Hauser-Kawaguchi, A; Luyt, LG; Turley, E. *Design of peptide mimetics to block pro-inflammatory functions of HA fragments.* Matrix Biology, **2017.**

Manuscripts in preparation

Hauser-Kawaguchi, A; Peart, T; Tolg, C; Ma, J; Turley, E; Luyt, LG. *The development of RHAMM peptide mimetics for inhibiting inflammation*, Manuscript in preparation.

Published abstracts

Hauser-Kawaguchi, A; Peart, T; Tolg, C; Turley, E; Luyt, LG. *Chemical Synthesis of 7 kDa RHAMM as the Receptor for the Discovery of Novel Peptide Ligands.* Proceedings of 34th EPS, 4-9 September 2016. Journal of Peptide Science, 2016, 22(9), OP-35, 27-28.

Potentinova, Z; **Hauser-Kawaguchi, A**; Turley, E; Luyt, LG. *Identification of Interactions between Tubulin-Derived Peptides and the Receptor for Hyaluronan Mediated Motility (RHAMM).* Proceedings of 34th EPS, 4-9 September 2016. Journal of Peptide Science, 2016, 22(9), PPXIV-374, 231.

Academic meetings

Hauser-Kawaguchi, A; Peart, T.; Tolg, C; Turley, E; Luyt, LG. The Development of Cyclic Peptides as RHAMM Mimics for Blocking Inflammation and RHAMM-Expressing Cancer. Oncology Research and Education Day, London, ON, June 16, 2017. (TED-style oral presentation)

Hauser-Kawaguchi, A; Peart, T.; Tolg, C; Turley, E; Luyt, LG. The Development of Cyclic Peptides as RHAMM Mimics for Blocking Inflammation. 100th Canadian Chemistry Conference and Exhibition, Toronto, ON, May 28-June 1. (oral presentation)

Hauser-Kawaguchi, A; Peart, T.; Tolg, C; Turley, E; Luyt, LG. The Development of Cyclic Peptides as RHAMM Mimics for Blocking Inflammation. 13th Medicinal and Bioorganic Chemistry Conference, Steamboat Springs, CO, January 22-26, 2017. (poster presentation)

Hauser-Kawaguchi, A; The Development of Cyclic Peptides as RHAMM Mimics for Blocking Inflammation. 2017 Fallona Family Interdisciplinary Showcase, London, ON, Janary 2017. (poster presentation)

Hauser-Kawaguchi, A; Peart, T; Tolg, C; Turley, E; Luyt, LG. Chemical Synthesis of 7 kDa RHAMM as the Receptor for the Discovery of Novel Peptide Ligands. 34th European Peptide Symposium & 8th International Peptide Symposium, Leipzig, Germany, September 2016. (oral presentation, Young Investigators Session)

Hauser-Kawaguchi, A; Peart, T; Tolg, C; Turley, E; Luyt, LG. Chemical Synthesis of 7 kDa RHAMM and Analysis of Protein-Ligand Interactions. Oncology Research and Education Day, London, ON, June 2016. (poster presentation)

Hauser-Kawaguchi, A; Tolg, C; Turley, E; Luyt, LG. Chemical Synthesis of 7 kDa RHAMM and Analysis of Protein-Ligand Interactions. 2015 Fallona Family Interdisciplinary Showcase, London, ON, December 2015. (poster presentation)

Hauser-Kawaguchi, A; Tolg, C; Turley, E; Luyt, LG. Chemical Synthesis of 7 kDa RHAMM and Analysis of Protein-Ligand Interactions. Boulder Peptide Symposium, Boulder, CO, September 2015. (poster presentation)

Hauser-Kawaguchi, A; Rodrigues, E; Luyt, LG. Chemical Synthesis of 7 kDa RHAMM and Analysis of Protein-Ligand Interactions. Oncology Research and Education Day, London, ON, June 2015. (poster presentation)

Hauser-Kawaguchi, A. Chemical Synthesis of 7 kDa RHAMM and Evaluation of Protein-Ligand Interactions. Cancer Research Laboratory Program Seminar Series, London, ON, January 2015. (oral presentation)